Summer 8-15-2018

Forward Electrophysiological Modeling and Inverse Problem for Uterine Contractions during Pregnancy

Mengxue Zhang
Washington University in St. Louis

WASHINGTON UNIVERSITY IN ST. LOUIS

School of Engineering and Applied Science

Department of Electrical & Systems Engineering

Dissertation Examination Committee:
Arye Nehorai, Chair
Mark A. Anastasio
R. Martin Arthur
Hari Eswaran
Lan Yang

Forward Electrophysiological Modeling and Inverse Problem for Uterine Contractions during Pregnancy

by

Mengxue Zhang

A dissertation presented to
The Graduate School
of Washington University in
partial fulfillment of the
requirements for the degree
of Doctor of Philosophy

August 2018
Saint Louis, Missouri

Contents

List of Figures

List of Tables

Acknowledgments

First and foremost, I would like to express my deepest gratitude to my advisor, Dr. Arye Nehorai, for providing me with an excellent Ph.D. training experience at Washington University in St. Louis (WUSTL). I am very thankful to him for his valuable concerns and suggestions both before and after I came to the United States of America. These made me feel well welcomed and helped me greatly to adapt to a new environment that is quite different from the one in my previous life. I also would like to thank him for introducing me to several statistical study groups, which helped me build a deep foundation in statistics. I am very grateful for his leading me into the interesting multidisciplinary project at the heart of this dissertation, providing me with continuous guidance and support, and encouraging me when I encountered obstacles during the research process. I also thank him for providing me with teaching opportunities with the study groups for new Ph.D. students in our department.

I also would like to convey my sincere gratitude to my principal collaborator, Dr. Patricio La Rosa, for his kind and dedicated advice on the research work. As a former Ph.D. student in Dr. Arye Nehorai's lab, Dr. La Rosa was the first to work on this interdisciplinary research topic. I am very grateful to him for his careful introduction of this topic to me. I am also thankful to him for sparing the time to provide me with inspirations and suggestions

on the problems that I encountered, and for carefully revising and providing constructive suggestions on the papers. I am grateful for his encouragement at the different stages of my Ph.D. study and enjoyed working with him and learning from his experience with Ph.D. and postdoctoral studies.

I would like to thank my dissertation committee members — Dr. Mark Anatosio, Dr. R. Martin Arthur, Dr. Hari Eswaran, and Dr. Lan Yang — for providing valuable suggestions on this dissertation. Also, I would like to thank our collaborators on the research topics. Specifically, I thank Dr. Vanessa Tidwell for collaborating on the multiscale forward model project, Dr. Diana Escalona-Vargas for her help with the plot of the real data and her discussion on the connectivity measure of uterine activity project, and Dr. Hari Eswaran and Dr. James D. Wilson for their discussions and feedback on the topics, and for providing me with the real measurement data that were used in this work.

My thanks also go to my past and current labmates: Elad, Peng, Xiaoxiao, Alex, Keyong, Zhao, Mianzhi, Prateek, Hesam, Yijian, Zhen, Eric, Yiqi, and Zhenqi. Their friendship and optimistic attitude always made the lab a pleasant place for me to work in. In particular, I am thankful for sharing me with different cultures of India, Iran, Isreal, USA, and multiple provinces of China, and for their discussions on my research topics. I also want to acknowledge all the other faculty and staff members of the Department of Electrical and Systems Engineering for their teaching and help. Special thanks go to Mr. James Ballard

at the Engineering Communication Center at WUSTL for spending time with me polishing my papers and dissertation.

Last but not least, I would like to express my deepest appreciation to my parents for encouraging me to pursue my dream, for supporting me emotionally, for their confidence in me, and for being with me no matter what happened during all these years. This Ph.D. journey would not have been possible without their accompaniment.

Mengxue Zhang

Washington University in Saint Louis

August 2018

Dedicated to my parents

ABSTRACT OF THE DISSERTATION

Forward Electrophysiological Modeling and Inverse Problem for Uterine Contractions during Pregnancy

by

Mengxue Zhang

Doctor of Philosophy in Electrical Engineering

Washington University in St. Louis, 2018

Professor Arye Nehorai, Chair

Uterine contractile dysfunction during pregnancy is a significant healthcare challenge that imposes heavy medical and financial burdens on both human beings and society. In the U.S., about 12% of babies are born prematurely each year, which is a leading cause of neonatal mortality and increases the possibility of having subsequent health problems. Post-term birth, in which a baby is born after 42 weeks of gestation, can cause risks for both the newborn and the mother. Currently, there is a limited understanding of how the uterus transitions from quiescence to excitation, which hampers our ability to detect labor and treat major obstetric syndromes associated with contractile dysfunction. Therefore, it is critical to develop objective methods to investigate the underlying contractile mechanism using a non-invasive sensing technique. This dissertation focuses on the multiscale forward electromagnetic modeling of uterine contractile activities and the inverse estimation of underlying source currents from abdominal magnetic field measurements.

We develop a realistic multiscale forward electromagnetic model of uterine contractions in the pregnant uterus, taking into account current electrophysiological and anatomical knowledge of the uterus. Previous models focused on generating contractile forces at the organ level or on ionic concentration changes at the cellular level. Our approach is to characterize the electromagnetic fields of uterine contractions jointly at the cellular, tissue, and organ levels. At the cellular level, focusing on both plateau-type and bursting-type action potentials, we introduce a generalized version of the FitzHugh-Nagumo equations and analyze its response behavior based on bifurcation theory. To represent the anisotropy of the myometrium, we introduce a random conductivity tensor model for the fiber orientations at the tissue level. Specifically, we divide the uterus into contiguous regions, each of which is assigned a random fiber angle. We also derive analytical expressions for the spiking frequency and propagation velocity of the bursting potential. At the organ level, we propose a realistic four-compartment volume conductor, in which the uterus is modeled based on the magnetic resonance imaging scans of a near-term woman and the abdomen is curved to match the device used to take the magnetomyography measurements. To mimic the effect of the sensing direction, we incorporate a sensor array model on the surface of abdomen. We illustrate our approach using numerical examples and compute the magnetic field using the finite element method. Our results show that fiber orientation and initiation location are the key factors affecting the magnetic field pattern, and that our multiscale forward model flexibly characterizes the limited-propagation local contractions at term. These results are potentially important as a tool for interpreting the non-invasive measurements of uterine contractions.

We also consider the inverse problem of uterine contractions during pregnancy. Our aim is to estimate the myometrial source currents that generate the external magnetomyography measurements. Existing works approach this problem using synthetic electromyography data. Our approach instead proceeds in two stages: develop a linear approximation model

and conduct the estimation. In the first stage, we derive a linear approximation model of the sensor-oriented magnetic field measurements with respect to source current dipoles in the myometrium, based on a lead-field matrix. In particular, this lead-field matrix is analytically computed from distributed current dipoles in the myometrium according to quasi-static Maxwell's equations, using the finite element method. In the second stage, we solve a constrained least-squares problem to estimate the source currents, from which we predict the intrauterine pressure. We demonstrate our approach through numerical examples with synthetic data that are generated using our multiscale forward model. In the simulations, we assume that the excitation is located at the fundus of the uterus. We also illustrate our approach using real data sets, one of which has simultaneous contractile pressure measurements. The results show that our method well captures the short-distance propagation of uterine contractile activities during pregnancy, the change of excitation area in subsequent contractions or even in a single contraction, and the timing of uterine contractions. These findings are helpful in understanding the physiological and functional properties of the uterus, potentially enabling the diagnosis of labor and the treatment of obstetric syndromes associated with contractile dysfunction such as preterm birth and post-term birth.

Chapter 1

Introduction

The uterus is a complex dynamic organ whose mechanism of operation during pregnancy is largely unknown. During most of pregnancy, the uterus is maintained in a quiescent, non-contractile state in which its myometrial smooth muscle cells are hyperpolarized and non-excitable. At term, the muscle cells become depolarized, excitable, and contractile. The coordination of these cells produces organized contractions and changes the intrauterine pressure to dilate cervix, resulting in the expulsion of the fetus from the mother's body [1]. In the U.S., approximately 12% of babies are born prematurely (< 37 weeks of gestation) and up to 10% are born post-term (> 42 weeks of gestation), creating in a significant healthcare challenge that has long-term medical and financial consequences [2–4].

For the affected children, preterm delivery results in life-long health challenges, including motor delays, lower intelligence quotients, and behavioral problems [2]. Similarly, post-term deliveries incur increased perinatal morbidity and mortality risks for both the mother and fetus, and a recent study has demonstrated that affected children are at increased risk of behavioral and emotional problems later in life [4]. Even in the case of normal term deliveries, where false labor is diagnosed, unwanted hospital stays and treatment could be avoided if physicians were able to more objectively determine whether the false labor would

progress to true labor, and, if so, on what time scale. The relatively few agents currently used to either arrest or promote uterine contractions are typically ineffectual and are often associated with adverse maternal and fetal effects [5–7]. Thus, there is a need for better understanding of the mechanisms that underlie uterine smooth muscle excitation-contraction coupling during pregnancy in order to enable prediction of labor and develop more effective regulatory treatments.

In order to better understand the labor process, we develop a realistic multiscale forward electromagnetic model of the pregnant uterus, taking into account current electrophysiological and anatomical knowledge, based on which we study the myometrial source current that produces the external electromagnetic fields. In the following, we will describe the anatomy and electrophysiology of the uterus, and the non-invasive technique we use to sense uterine activities.

1.1 Uterine anatomy

The uterus is an inverted pear-shaped, hollow, muscular organ with thick walls in the female reproductive system [8]. Fig. 1.1 illustrates the anatomy and microanatomy of the human uterus. The fundus is the uppermost curved area, where the fallopian tubes connect to the uterus, and the cervix is in the lower end, opening into the vagina (see upper left in Fig. 1.1). The uterine wall is comprised of three layers (upper right in Fig. 1.1):

1. the endometrium, the inner layer, which responds to cyclic ovarian hormone changes;
2. the myometrium, the middle layer, mostly consisting of smooth muscle cells, also known as myocytes; and

3. the perimetrium, the outer layer enveloping the uterus.

The layer responsible for uterine contractions is the myometrium (bottom in Fig. 1.1), whose macroscopic structures are fasciculi that comprise sheet-like and cylindrical bundles of myocytes (muscle fibers) embedded in a connective tissue matrix [9]. The bundles are contiguous within a fasciculus with myocytes in a bundle close to each other. The fasciculi are interconnected via communicating bridges that allow electrical communication among them. Since the end of the 19th century, a large amount of work has been done to investigate the overall muscle fiber orientations in the human uterus [10–13]. Although there is no widely accepted model of the fiber architecture, it introduces anisotropy into action potential propagation [13, 14].

1.2 Uterine electrophysiology

The functional units of the uterus are the myocytes, which are long, narrow, and almost spindle shaped smooth muscle cells. The cell membrane that separates the interior of the cell from the extracellular environment is selectively permeable to ions such as Na^+, K^+, Ca^{2+}, and Cl^- and regulates the entry and exit of these ions. The membrane potential, the potential difference across the cell membrane, is a result of the unequal distribution of ions inside and outside the cell [15–17]. Ions move through ionic channels in a direction that is determined by the intracellular and extracellular ion concentrations as well as the membrane potential. The concentrations of Na^+, Ca^{2+}, and Cl^- are higher in the extracellular domain, whereas the concentration of K^+ is higher inside the cell. The permeability and relative concentrations of these ions determine the resting potential of myocytes, which is in general

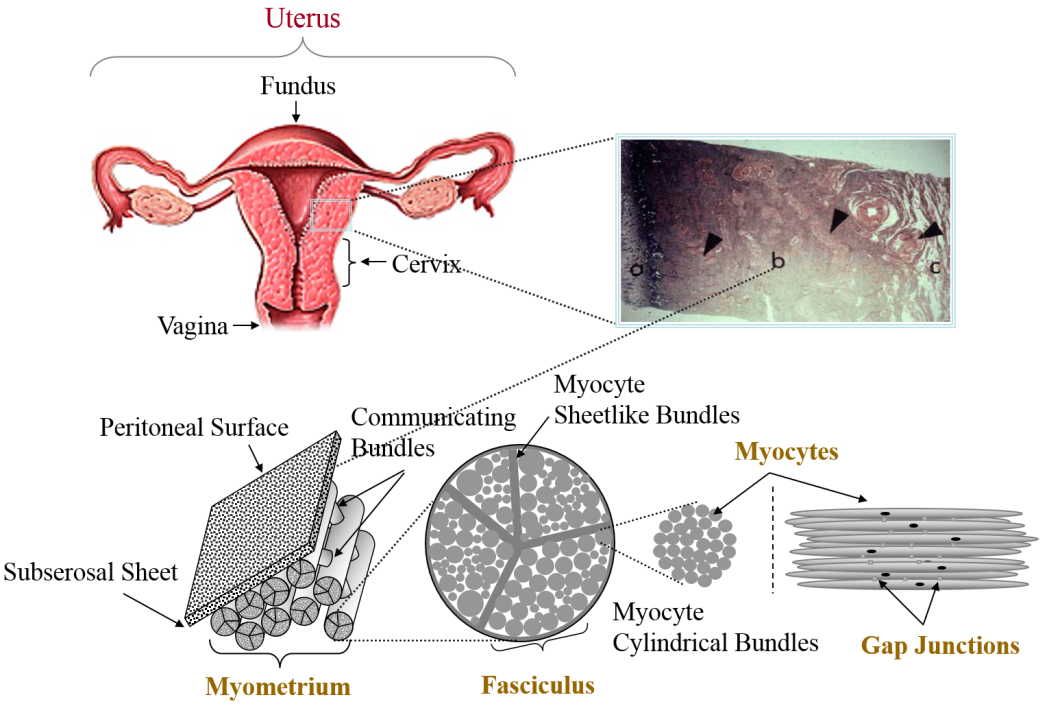

Figure 1.1: Anatomy and microanatomy of the human uterus. Upper left: illustration of the human uterus. Upper right: uterine wall with the (a) endometrium (b) myometrium and (c) perimetrium. Bottom: microanatomy of the pregnant human myometrium (source: Young, 1999 [9]).

-40 to -50 mV. During pregnancy, it becomes more negative, approaching -60 mV, and then increases to about -45 mV near term.

Contractile activity in the uterus is initiated by an action potential that is generated autonomously in a cell when the threshold of firing is reached. Such cells function similarly to pacemakers in the stomach, intestine, and heart [15, 18, 19] that can spontaneously excite action potentials. In the uterus, the smooth muscle cells either can spontaneously generate their own impulses or can be excited by the action potentials propagating from neighboring cells. However, it is still unclear whether there exists a specific pacemaker mechanism or a specific pacemaker area [20]. Except for some observations of contractile

activity originating from specialized cells [21], most activities arise from any site throughout the myometrium [22, 23]. The initiation area can even change during a single contraction or successive contractions [23].

The action potential is attributed to the entry of Ca^{2+} through voltage-sensitive calcium channels, and, perhaps also through fast Na^{+} channels [24] close to the end of the pregnancy. There are two predominant types of action potentials in both a single uterine smooth muscle cell and isolated strips of myometrium: plateau-type and bursting-type [17, 25]. At term, the mechanical contractions correlate to action potentials as follows:

1. The frequency of the contractions is related to the frequency of the action potentials.
2. The duration of the contraction is related to the duration of the train of action potentials.
3. The contractile strength is related to the spike numbers in the action potential and the number of simultaneously activated cells.

At some unknown point during pregnancy, the uterine smooth muscle cells communicate and coordinate with each other to generate organized activities. Electrical synapses called gap junctions, which consist of pores composed of proteins known as connexins, connect the interiors of two cells and allow molecules and current to flow between cells. The gap junctions are sparse throughout pregnancy but increase during delivery [26–31] and disappear within 24 hours after delivery. The increase strengthens the coupling of cells, resulting in the synchronization and coordination of various regions in the uterus. The action potential propagation enabled by gap junctions has been assumed to be the only mechanism for the recruitment of myometrium in uterine contractions [32]. However, animal and human data

indicates that action potentials propagate noncontiguously and only over short distances [23, 33, 34]. A new mechanism, called mechanotransduction, is proposed in [35] for long-distance signaling. In this mechanism, a local contraction is initiated and propagated by action potential, increasing the intrauterine pressure and hence the wall tension, and inducing more local contractions to generate strong uterine contractile activities.

1.3 Non-invasive sensing techniques

Various techniques have been developed to monitor uterine activities. Apart from recording changes in cervical dilation, the frequency and duration of uterine contractions are monitored by tocodynamometry (TOCO), in which a strain gauge responds to changes in uterine tension that are transmitted to the abdomen [36]. This technique is non-invasive, simple, and almost risk free, but it cannot identify contraction intensity and suffers from maternal motion artifacts. An alternative technique is to measure the intrauterine pressure using an intrauterine pressure catheter (IUPC), which is more reliable and accurate than TOCO. However, this procedure requires rupturing the amniotic membrane and may introduce risks of infection and abruption. Fig. 1.2 illustrates the TOCO and IUPC techniques.

Currently, there are two methods employed to record the electrophysiological activity of uterine contractions. The first is electromyography (EMG) [37], which measures the action potentials using either internal electrodes or electrodes attached to the abdomen [38, 39]. EMG studies on rats with electrodes placed simultaneously in the uterus and on the abdominal surface have shown that every burst of action potential recorded directly from the myometrium corresponds to a burst measured on the abdominal surface and to the mechanical contraction recorded by a pressure catheter [38]. This technique has a high temporal

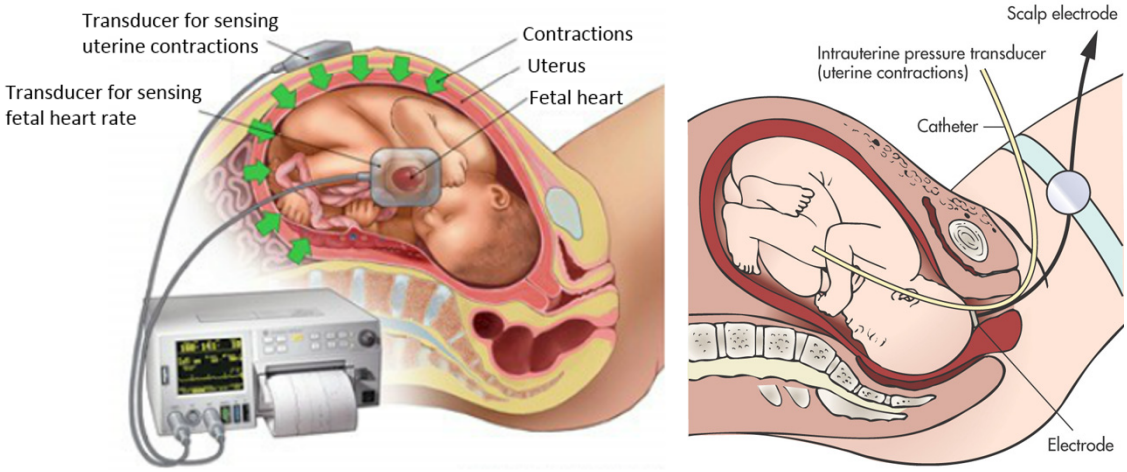

(a) TOCO (source: AMICUS Visual Solutions, 2007) (b) IUPC (source: Mosby. Inc, 2004)

Figure 1.2: TOCO and IUPC techniques used to monitor uterine contractions.

resolution, but suffers from attenuation during propagation to the maternal abdominal surface because the measured activity arises from volume currents and is strongly dependent on tissue conductivity [40]. In addition, having many pairs of electrodes on the maternal abdomen is uncomfortable and cumbersome. A magnetic homologue, magnetomyography (MMG), is a more recently developed non-invasive technique that records the magnetic field corresponding to the uterine electrical activity. Unlike EMG, MMG, without making electrical contact with the body and arising from the primary current, is much less dependent on tissue conductivity [41] and is independent of any kind of reference, ensuring the localized recording of uterine activities. However, the device for MMG recording is expensive, which limits its wide applicability. These two techniques are illustrated in Fig. 1.3.

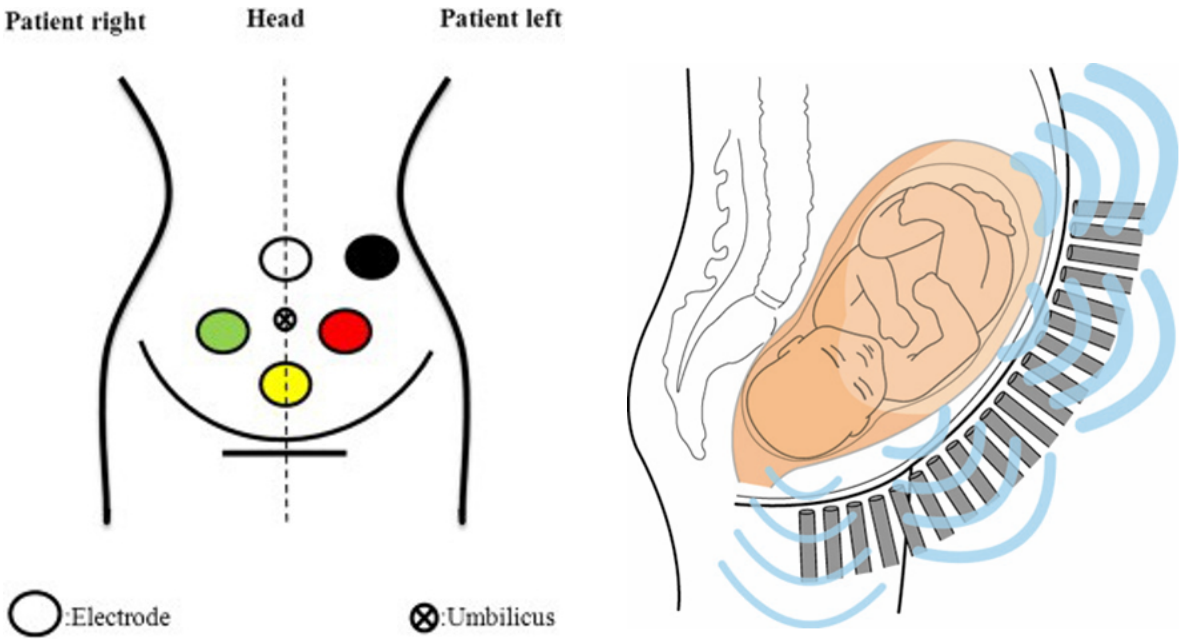

(a) EMG (source: Vasak et. al., 2013 [42]) (b) MMG (source: La Rosa et. al., 2008 [43])

Figure 1.3: EMG and MMG techniques used to record the electrophysiological activity of uterine contractions.

1.4 Clinical site and data collection

After the study protocol was explained to subjects and written consents to perform the study were obtained, abdominal MMG data were collected at the University of Arkansas for Medical Sciences (UAMS). The protocol was approved by the UAMS Institutional Review Board. The system (Fig. 1.4(a)) used to record the data is called SARA: SQUID (superconducting quantum interference device) array for reproductive assessment. This device is installed in a magnetically shielded room next to the labor and delivery unit in the UAMS, to reduce external magnetic fields which interfere with the biomagnetic field generated by human organs. This SARA system consists of 151 primary magnetic sensors spaced 3 cm apart over an area of 850 cm^2 (Fig. 1.4(b)), arranged in a concave array covering the maternal abdomen from the pubic symphysis to the uterine fundus, and laterally over a similar span.

Each sensor measures the magnetic fields at two magnetometers, one close to abdomen and the other 8 cm away from the first one in a direction similar but not identical to the normal of the SARA surface (Fig. 1.4(c)). The sensor measurement is the difference between the measurements from these two magnetometers. The subject simply sits and leans forward slightly against the smooth surface of the array (Fig. 1.4(d)), allowing the SQUID sensors to receive electrophysiological signals.

The procedure to record and preprocess MMG data is illustrated in Fig. 1.5. All of the MMG data sets were first recorded at 250 Hz and then downsampled to 32 Hz. For the preprocessing, we applied a 8th-order band-pass Butterworth filter of $0.1-1$ Hz to attenuate interfering maternal and fetal cardiac signals. A 8th-order band-stop (notch) Butterworth filter of $0.25-0.35$ Hz was also applied to suppress maternal breathing, which is a prominent signal around 0.33 Hz. Noisy sensors were then removed to avoid possible pollution in MMG measurements. Using spectral analysis, the primary magnetic activity of a uterine contraction is represented by a low frequency band between 0.1 Hz and 0.4 Hz [44, 45]. The MMG activity in this range likely represents the plateau and repolarization phase of the action potentials. For a more accurate analysis that is closer to the true time-frame, a higher band $0.4-1$ Hz should be added to the analysis [44,45]. Also, early studies [29, 46, 47] have shown that the power spectrum density of uterine EMG bursts in subjects during active labor peaks at 0.71 ± 0.05 Hz, compared to the 0.48 ± 0.03 Hz value for non-laboring term subjects. Most of the uterine EMG studies apply a bandwidth of $0.35-1$ Hz. The lower band limit of 0.35 Hz is chosen to avoid movement artifacts and also because maternal breathing around the frequency of 0.33 Hz can contaminate uterine EMG acquisition. For the collection of MMG, the frequency band $0.1-0.25$ Hz is also included since it is possible to acquire signals as low as 0.1 Hz with a relatively high signal to noise ratio with the SARA system [48, 49].

(a) SARA system installed in UAMS hospital

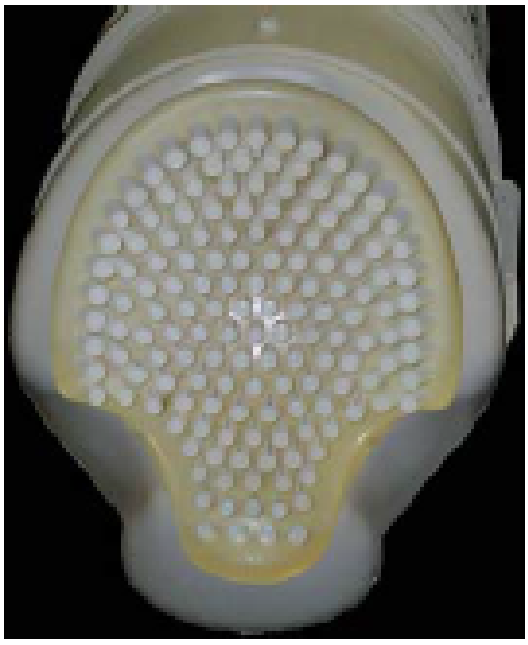

(b) The 151-channel sensor array with each sensor spaced 3 cm apart

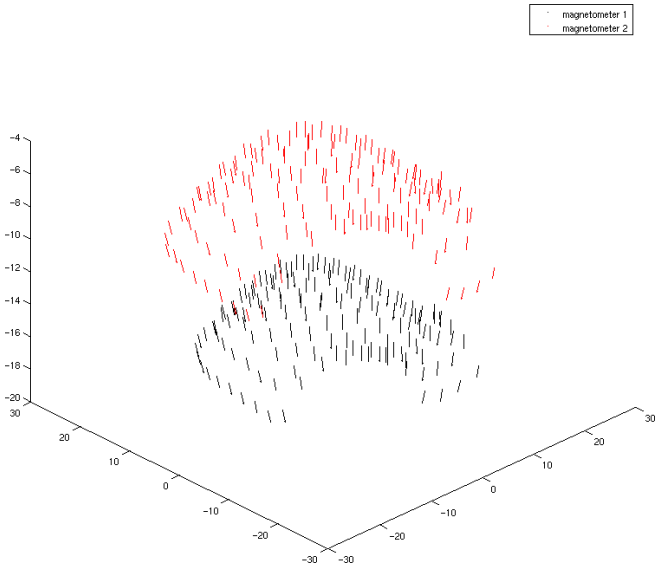

(c) Layout of the magnetometers of SQUID sensors (in centimeters)

(d) Subject sits and leans against the surface of the system

Figure 1.4: The SARA device used to non-invasively collect MMG data of uterine activities.

1.5 Contributions of this work

In this dissertation, we investigate the uterine contractions during pregnancy from two perspectives: forward and inverse. We develop a realistic multiscale forward electromagnetic

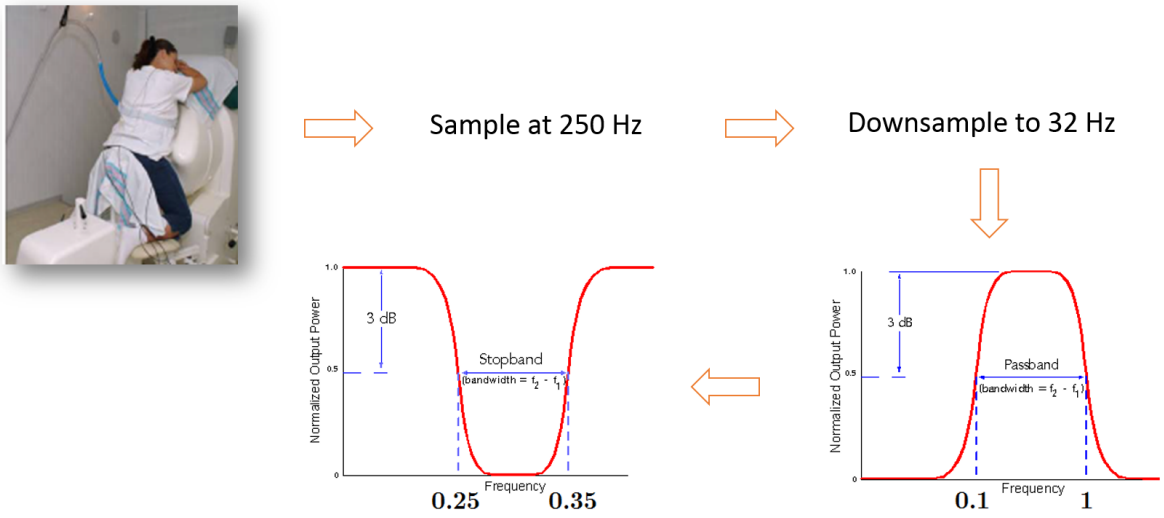

Figure 1.5: Recording and preprocessing of real MMG data.

model considering current electrophysiological and anatomical knowledge, and derive the inverse estimation of the underlying source currents from the external measurements. We summarize the main contributions as follows.

Multiscale forward model: The development of effective tools to characterize uterine contractions during pregnancy is important for better understanding their underlying mechanisms. Our method is to establish a multiscale model, which integrates the knowledge from the cellular, tissue, and organ levels, to describe the electromagnetic properties of uterine contractile activities. Our modeling approach aims at computing the abdominal magnetic field that is generated by the myometrial current source and propagates through a four-compartment volume conductor. We assume that the abdomen deforms to follow the contour of the SARA device when the subject leans against it, and we model the uterus based on the MRI of a pregnant, near-term woman. Considering the anisotropic property of tissue fibers in the uterus, we design a random conductivity tensor model that assigns different fiber orientations to different regions of the uterus. This model is applicable to arbitrary uterine shapes.

The myometrial current source is modeled as a function of the transmembrane potential by introducing a generalized version of the FitzHugh-Nagumo equations in each myometrial cell. We investigate the parameters of this cellular model using bifurcation analysis in order to generate both plateau-type and bursting-type potentials. We analytically compute our model using the finite element method, investigate the effect of model configuration aspects on model outputs, and conduct initial validation of our multiscale model against real MMG measurements. The numerical results show that fiber orientation and initiation location are the key factors that influence the MMG pattern, and our model flexibly characterizes clinically observed local contractile activities during pregnancy.

Inverse estimation: The non-invasive MMG measurements obtained using the SARA device incorporate the electrophysiological activity of the uterus. Therefore, the inverse problem of investigating the internal myometrium from external MMG data is promising for understanding the physiological and functional properties of the uterus. In this work, we propose a method to estimate the underlying source currents of uterine contractions using the MMG obtained from the SARA device. We first develop a linear approximation model that relates the sensor-oriented MMG measurements to the currents in the myometrium, and then conduct the inverse estimation. In the first stage, we introduce distributed current dipoles as the source model in the myometrium and establish the lead-field matrix by analytically solving the MMG measurements that propagate from the unit current dipole in the myometrium through the realistic volume conductor to the SARA sensors outside the abdomen. In the second stage, we solve a constrained optimization problem to estimate the main myometrial source currents. Based on this estimation, we predict the intrauterine pressure to show its clinical use. We validate our method using both synthetic data generated by our multiscale foward model and real MMG data collected using the SARA device. Our method proves to be able to characterize the short-distance propagation of local contractile activities in the

uterus and in timing contractions as well, which is potentially helpful in predicting labor and treating obstetric syndromes associated with preterm or post-term birth.

1.6 Organization of the dissertation

The rest of the dissertation is organized as follows. In Chapter 2, a realistic multiscale forward electromagnetic model of uterine contractions in the pregnant uterus is presented. In Chapter 3, the inverse estimation of source currents of uterine contractile activity that produce MMG measurements is conducted. In Chapter 4, we summarize the contributions of this dissertation and discuss future directions.

Chapter 2

Realistic Multiscale Electromagnetic Forward Modeling[1]

In the following chapter, we will investigate uterine contractile activities during pregnancy from the forward modeling perspective.

We begin by developing a realistic multiscale electromagnetic model of uterine contractions during pregnancy. At the cellular level, building on bifurcation theory, we apply generalized FitzHugh-Nagumo (FHN) equations to produce both plateau-type and bursting-type action potentials. At the tissue level, we introduce a random fiber orientation model applicable to an arbitrary uterine shape. We also develop an analytical expression for the propagation speed of transmembrane potential. At the organ level, a realistic volume conductor geometry model is provided based on magnetic resonance images (MRI) of a pregnant woman. To simulate the sensing directions of the SARA device, we propose a sensor array model. We

[1]This chapter is based on M. Zhang, V. Tidwell, P. S. La Rosa, J. D. Wilson, H. Eswaran, and A. Nehorai, "Modeling magnetomyograms of uterine contractions during pregnancy using a multiscale forward electromagnetic approach," *PLOS ONE* 11(3): E0152421, DOI: 10.1371/journal.pone.0152421, Mar. 2016.

then demonstrate with numerical examples that our model is able to reproduce the characteristics of action potentials. Additionally, we investigate the sensitivity of MMG to model configuration aspects such as volume geometry, fiber orientation, and initiation location. Our numerical results show that fiber orientation and initiation location are the key aspects that greatly affect the MMG as measured by the SARA device. We conclude that sphere is appropriate as an approximation of the volume geometry. The initial step towards validating the model against real MMG measurement is also presented. Our results show that the model flexibly mimics the limited-propagation magnetic signature during the emergence and decay of a uterine contraction.

2.1 Introduction

In this section, we will describe briefly the existing models and our approach to characterizing uterine contractile activities during pregnancy.

2.1.1 Previous approaches

The uterus provides a safe environment for a developing fetus, which is later expelled through intense contractions. These contractions are primarily regulated by uterine electrical activities [22, 32]. Previous models [50, 51] rarely considered the physiological properties of the myometrium. A computer model consisting of discrete contractile elements that propagate electrical impulses and generate tension is proposed in [50]. The authors predict contraction waveforms by defining contracting and refractory periods. In [51], the authors demonstrate

that two mechanisms, action potential propagation and calcium wave propagation, contribute to intercellular communication.

The models presented in [52–57] take into account the physiological aspect of uterine contractions. A simple electrophysiological model of a smooth muscle cell is developed in [52]. The limitation of this model is that it includes only sodium and potassium currents, but not other involved physiological ionic currents. In [53], the authors propose a model that considers the electrical and mechanical properties of smooth muscle cells; however, the model disregards the time dependency of the calcium current. In [54], a model is developed to study the process of myometrial excitation and contraction. This model describes L-type Ca^{2+} current, Ca^{2+} pumps, and Na^{+}/Ca^{2+} exchangers without including the time-dependency dynamics. In [55], the authors construct a model in terms of voltage-dependent Na^{+} currents, voltage-dependent Ca^{2+} currents, voltage and calcium-dependent K^{+} currents, a leakage current, and the dynamics of intracellular calcium concentration. In [56], the authors provide a more detailed smooth muscle cell model, which incorporates 13 ionic currents and calcium dynamics, to reproduce different types of action potentials. In [57], KCNQ and hERG channel currents are added into the uterine cell model which is developed in [56], enabling simulations of long-lasting bursting-type action potentials.

Recently, the models have focused on characterizing the electrophysiological property of uterine contractions jointly at the cellular, tissue, and organ levels. A 2D multiscale model for uterine electrical activity is presented in [58, 59]. This model considers K^{+} current and the dynamics of Ca^{2+} at the cell scale, applies a 2D isotropic grid of square cells at the tissue scale, and simulates the surface electrohysterogram at the organ scale. In [60], a multiscale electromagnetic model of uterine contractions is developed. This model is the first to apply

a 3D multiscale approach to uterine modeling. However, it regards the uterus as a sphere with fixed-angle conductivity, which is an oversimplified version of the real geometry.

2.1.2 Our approach

In this work, based on the simplified model in [60], we develop a more realistic multiscale forward model of uterine contractions during pregnancy. We first introduce an ionic current model capable of generating both plateau-type and bursting-type action potentials in each myocyte. Specifically, using bifurcation analysis, we develop a generalization of the FitzHugh-Nagumo (FHN) equations capable of generating both types of action potentials. Second, we introduce a random fiber orientation model applicable to an arbitrary uterine shape. An analytical expression for the speed of propagation is also developed. Third, instead of a spherical model, we introduce a realistic model for the volume conductor geometry based on magnetic resonance images (MRI) of a pregnant woman. We also propose a sensor array model matching the SARA device to simulate real sensing directions of the SARA device [48, 49, 61]. The numerical results illustrate the main characteristics of both types of action potentials. We also demonstrate that the pattern of the magnetic field depends greatly on the fiber orientation and initiation location, rather than the volume geometry. The spherical volume geometry is therefore a good approximation of uterine geometry for investigating the MMG measurements of the SARA device. We also validate that our modeling approach can flexibly mimic the limited-propagation magnetic field pattern of real subject data during the emergence and decay of contraction.

Our aim is to better understand the uterine structure and the propagation of contractions from an electrophysiological point of view and to determine which aspects of the model

configuration have a major influence on the pattern of the abdomen-surface magnetic field, as measured by the SARA device. By creating a variety of model configuration aspects, e.g., by spatially varying the fiber layout or conductivity properties of the myometrium, and then simulating the magnetic field on the abdominal surface for each configuration, we seek to determine the extent to which each aspect of the configuration influences the pattern of magnetomyograms. Creating a realistic multiscale forward model of uterine contractions will allow us to better interpret the data from MMG measurements, and thus to characterize the underlying contractile mechanisms.

2.2 Preliminary work

In this section, we summarize our preliminary work. In our recent work [60], we proposed a multiscale electromagnetic forward model of human myometrial contractions during pregnancy, whose details are listed in Table 2.1. Fig. 2.1 illustrates the three levels that are involved in the modeling: cell, tissue, and organ.

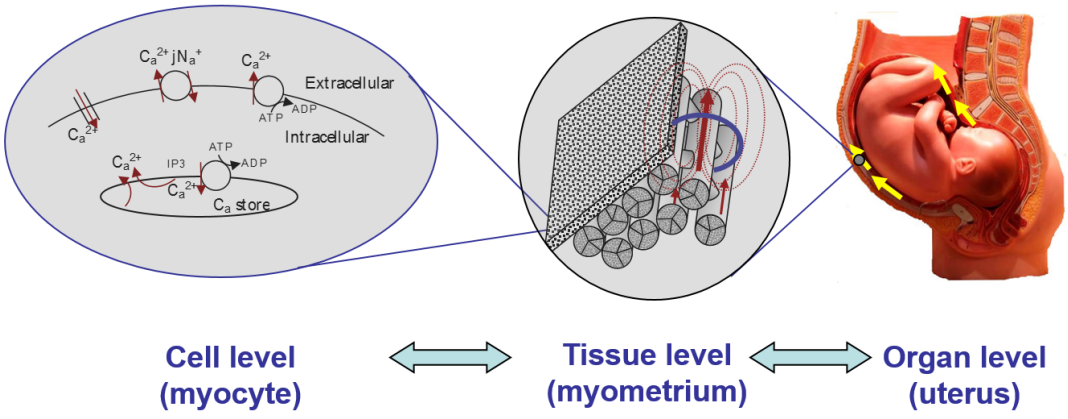

Figure 2.1: Illustration of the three levels (cell, tissue, and organ) involved in the modeling.

Table 2.1: Equations of our previous uterine model.

Magnetic field	$\nabla \times \boldsymbol{B}(\boldsymbol{r},t) = \mu_0(\boldsymbol{J}_{\mathrm{s}}(\boldsymbol{r},t) - \boldsymbol{G}(\boldsymbol{r})\nabla\phi(\boldsymbol{r},t))$ (2.1)
Electrical potential	$\nabla \cdot \boldsymbol{G}_{\mathcal{A}}(\boldsymbol{r})\nabla\phi(\boldsymbol{r},t) = 0, in\ \mathcal{A}$ (2.2)
	$\nabla \cdot \boldsymbol{G}_{\mathcal{U}}(\boldsymbol{r})\nabla\phi(\boldsymbol{r},t) = 0, in\ \mathcal{U}$ (2.3)
	$\nabla \cdot \boldsymbol{G}_{\mathrm{e}}^{'}\nabla\phi_{\mathrm{e}}(\boldsymbol{r},t) = -\nabla \cdot \frac{\zeta}{\zeta+1}\boldsymbol{G}_{\mathrm{e}}^{'}\nabla v_{\mathrm{m}}(\boldsymbol{r},t), in\ \mathcal{M}$ (2.4)
Current source density	$\boldsymbol{J}_{\mathrm{s}}(\boldsymbol{r},t) = -\zeta\boldsymbol{G}_{\mathrm{e}}^{'}\nabla v_{\mathrm{m}}(\boldsymbol{r},t), in\ \mathcal{M}$ (2.5)
Transmembrane potential	$\nabla \cdot \frac{\zeta}{\zeta+1}\boldsymbol{G}_{\mathrm{e}}^{'}\nabla v_{\mathrm{m}}(\boldsymbol{r},t) = a_{\mathrm{m}}(c_{\mathrm{m}}\frac{\partial v_{\mathrm{m}}(\boldsymbol{r},t)}{\partial t} + \boldsymbol{J}_{\mathrm{ion}}(\boldsymbol{r},t) - \boldsymbol{J}_{\mathrm{stim}}(\boldsymbol{r},t)), in\ \mathcal{M}$ (2.6)
Stimulus activity	$\boldsymbol{J}_{\mathrm{stim}}(\boldsymbol{r},t) = \frac{1}{\varepsilon_1}\sum_{i=1}^{N_{\mathrm{p}}}\nu_i h_i(\boldsymbol{r},t)$ (2.7)

Our modeling approach (Fig. 2.2) was to solve the forward electromagnetic problem of uterine contractions using a four-compartment volume conductor geometry, namely, we computed at the abdominal surface the magnetic field, $\boldsymbol{B}(\boldsymbol{r},t)$ (2.1), and the electrical potential, $\phi(\boldsymbol{r},t)$ (2.2)–(2.4), generated by the myometrial current source density, $\boldsymbol{J}_{\mathrm{s}}(\boldsymbol{r},t)$ (2.5). In the

Table 2.1: Equations of our previous uterine model (cont.)

Boundary conditions	$\phi_{\mathrm{e}}(\boldsymbol{r},t) = \phi_{\mathcal{A}}(\boldsymbol{r},t), in\ \partial\mathcal{M}$	(2.8)
	$\hat{\boldsymbol{n}}_{\mathcal{M}} \cdot (\boldsymbol{G}_{\mathrm{i}}{}'\nabla\phi_{\mathrm{i}}(\boldsymbol{r},t) + \boldsymbol{G}_{\mathrm{e}}{}'\nabla\phi_{\mathrm{e}}(\boldsymbol{r},t)) = \hat{\boldsymbol{n}}_{\mathcal{M}} \cdot \boldsymbol{G}_{\mathcal{A}}\nabla\phi_{\mathcal{A}}(\boldsymbol{r},t), in\ \partial\mathcal{M}$	(2.9)
	$\hat{\boldsymbol{n}}_{\mathcal{M}} \cdot \boldsymbol{G}_{\mathrm{i}}'\nabla v_{\mathrm{m}}(\boldsymbol{r},t) = 0, in\ \partial\mathcal{M}$	(2.10)
	$\phi_{\mathrm{e}}(\boldsymbol{r},t) = \phi_{\mathcal{U}}(\boldsymbol{r},t), in\ \partial\mathcal{U}$	(2.11)
	$\hat{\boldsymbol{n}}_{\mathcal{U}} \cdot (\boldsymbol{G}_{\mathrm{i}}{}'\nabla\phi_{\mathrm{i}}(\boldsymbol{r},t) + \boldsymbol{G}_{\mathrm{e}}{}'\nabla\phi_{\mathrm{e}}(\boldsymbol{r},t)) = \hat{\boldsymbol{n}}_{\mathcal{U}} \cdot \boldsymbol{G}_{\mathcal{U}}\nabla\phi_{\mathcal{U}}(\boldsymbol{r},t), in\ \partial\mathcal{U}$	(2.12)
	$\hat{\boldsymbol{n}}_{\mathcal{U}} \cdot \boldsymbol{G}_{\mathrm{i}}'\nabla v_{\mathrm{m}}(\boldsymbol{r},t) = 0, in\ \partial\mathcal{U}$	(2.13)
	$\hat{\boldsymbol{n}}_{\mathcal{A}} \cdot \boldsymbol{G}_{\mathcal{A}}\nabla\phi_{\mathcal{A}}(\boldsymbol{r},t) = 0, in\ \partial\mathcal{A}$	(2.14)
	$\hat{\boldsymbol{n}}_{\mathcal{F}} \cdot \boldsymbol{G}_{\mathcal{U}}\nabla\phi_{\mathcal{U}}(\boldsymbol{r},t) = \lambda(\hat{\boldsymbol{n}}_{\mathcal{F}} \cdot \boldsymbol{G}_{\mathcal{F}}\nabla\phi_{\mathcal{F}}(\boldsymbol{r},t)), in\ \partial\mathcal{F}$	(2.15)

volume conductor geometry model as illustrated in Fig. 2.2, $\mathcal{A}$ represents the abdominal cavity and $\partial\mathcal{A}$ the boundary surface defined by the abdomen. $\mathcal{M}$ represents the myometrium, and $\partial\mathcal{M}$ and $\partial\mathcal{U}$ are its external and internal boundary surfaces, respectively. The volume

denoted by $\mathcal{U}$ represents the space filled with the amniotic fluid that exists between the internal uterine wall $\partial\mathcal{U}$ and the boundary $\partial\mathcal{F}$ defined by the fetus volume $\mathcal{F}$.

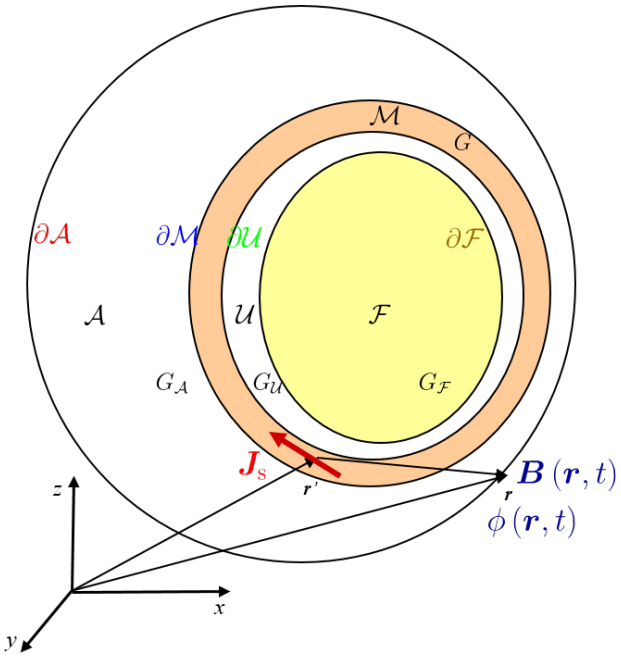

Figure 2.2: Illustration of the four-compartment volume conductor geometry and the forward electromagnetic problem of uterine contractions.

Fig. 2.3 illustrates the bidomain approach we applied to model the current source density and the transmembrane potential. According to the Ohm's law, the current source density $\boldsymbol{J}_{\mathrm{s}}(\boldsymbol{r},t)$ was defined as the gradient of the transmembrane potential, $v_{\mathrm{m}}(\boldsymbol{r},t)$ (2.6). The transmembrane potential $v_{\mathrm{m}}(\boldsymbol{r},t)$, using reaction diffusion equations, was modeled as a function of the ionic current dynamics, $\boldsymbol{J}_{\mathrm{ion}}(\boldsymbol{r},t)$, stimulus current due to excitation, $\boldsymbol{J}_{\mathrm{stim}}(\boldsymbol{r},t)$ (2.7), anisotropic conductivity, $\boldsymbol{G}_{\mathrm{i}}^{'}$ and $\boldsymbol{G}_{\mathrm{e}}^{'}$, and the corresponding boundary conditions (2.8)–(2.15).

Focusing on the plateau-type action potential, we applied the modified version of the FHN equations [62, 63] to model the ionic currents, $\boldsymbol{J}_{\mathrm{ion}}(\boldsymbol{r},t)$, in each myocyte. We also proposed a general approach to design conductivity tensors, $\boldsymbol{G}_{\mathrm{i}}^{'}$ and $\boldsymbol{G}_{\mathrm{e}}^{'}$, simply assuming that the

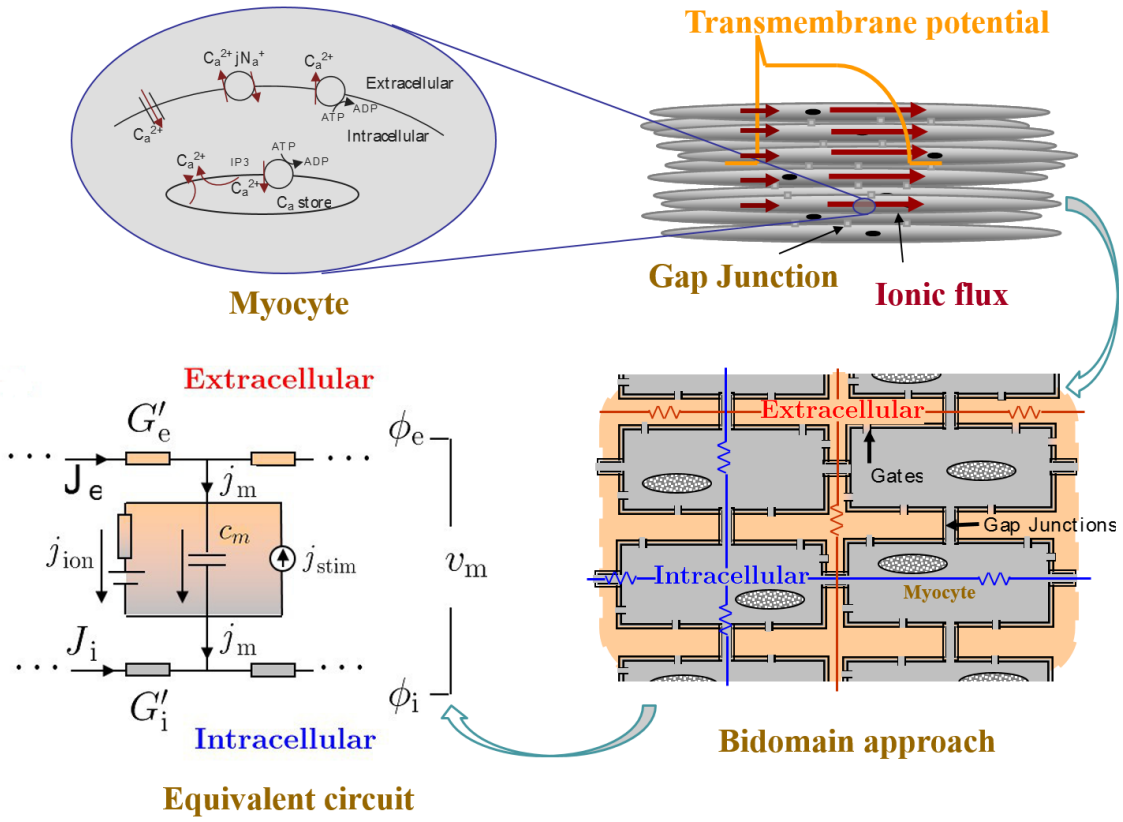

Figure 2.3: Illustration of the bidomain approach used to model the current source density and the transmembrane potential.

main axis of the fibers runs vertically from the fundus to the cervix for any uterine shape. To model the volume conductor geometry, we defined a spherical uterus and also a spherical abdomen as a simplification of the real anatomical structure. Although our preliminary work provides a novel approach to model the contractions in the pregnant uterus, some aspects of the model are oversimplified when compared with the realistic case.

2.3 Realistic multiscale forward model

In this section, we explain explicitly how we develop a more realistic multiscale forward model of uterine contractions during pregnancy, taking into consideration current electrophysiological and anatomical characteristics of the uterus.

2.3.1 Bursting-type action potential model at the cellular level

At the cellular level, we develop an ionic current model capable of generating plateau-type and bursting-type action potentials (Fig. 2.4), since both of them are very common in smooth muscle cells or isolated strips of myometrium [17, 25, 64]. Particularly, we apply a variation of the FHN equations [60], which is given by the following nonlinear dynamical system of ordinary differential equations:

$$\frac{\partial v_{\mathrm{m}}}{\partial t} = \frac{1}{\varepsilon_1 c_{\mathrm{m}}}(k(v_{\mathrm{m}} - v_1)(v_2 - v_{\mathrm{m}})(v_{\mathrm{m}} - v_3) - w + \nu), \tag{2.16}$$

$$\frac{\partial w}{\partial t} = \varepsilon_2(\beta v_{\mathrm{m}} - \gamma w + \delta), \tag{2.17}$$

where v_{m} is the action potential, w is a state variable, ν is the stimulus current amplitude due to an excitation activity, which is defined in Eq. (2.7), and ε_1, ε_2, k, β, γ, δ, v_1, v_2, and v_3 are model parameters.

The behavior of a nonlinear dynamical system depends greatly on the values of its parameters. For example, for certain set of parameters, the FHN model has a stable but excitable equilibrium. That is, if the system undergoes a sufficiently large perturbation, there is a large excursion of variables in phase space before returning to the equilibrium, hence generating a

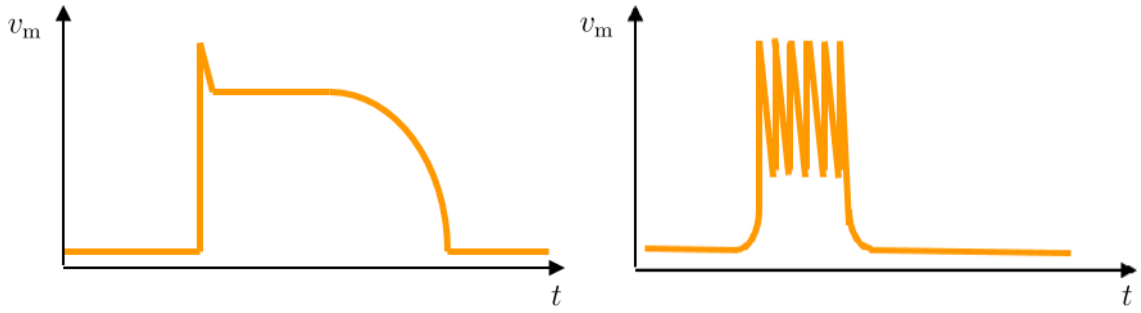

(a) Plateau-type action potential (b) Bursting-type action potential

Figure 2.4: Caricature of the two types of action potentials observed in the human uterus.

plateau-type action potential (Fig. 2.5(a)). There is also a range of parameter values where the FHN model displays limit cycle characteristics; that is, the variables settle on a closed trajectory in phase space, hence spike trains occur in the system (Fig. 2.5(b)).

In this work, we focus on investigating the bursting-type action potential, which occurs when the FHN model displays limit cycle behavior. In order to identify the set of parameters that generates a limit cycle, we apply bifurcation analysis to the variation of the FHN model. Bifurcation analysis is a powerful tool to investigate such properties of nonlinear dynamical systems. It helps to identify the set of parameters with which certain behavior occurs in the systems. The parameter that is varied is known as a bifurcation parameter. We assume in this work that the uterus is formed by cells of the same type. The excitation activity is represented by a specified stimulus current but the parameters of the ionic current cell model are exactly the same throughout the uterus. Therefore, the only degree of freedom that we have is the stimulus amplitude, which can be varied at initiation, so it can be regarded as the bifurcation parameter. In other words, our claim is that the cell response changes on the basis of the initiation activity.

In bifurcation analysis, equilibrium, limit cycle, and their stabilities appear as a function of the bifurcation parameter. Since the right hand side of Eq. (2.16) is a cubic polynomial

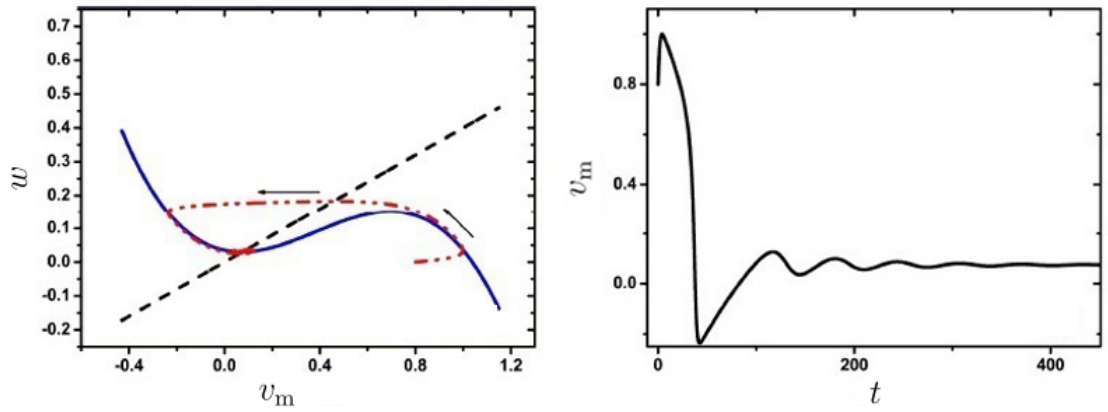

(a) Phase space plot with variables returning to equilibrium and the corresponding plateau-type action potential

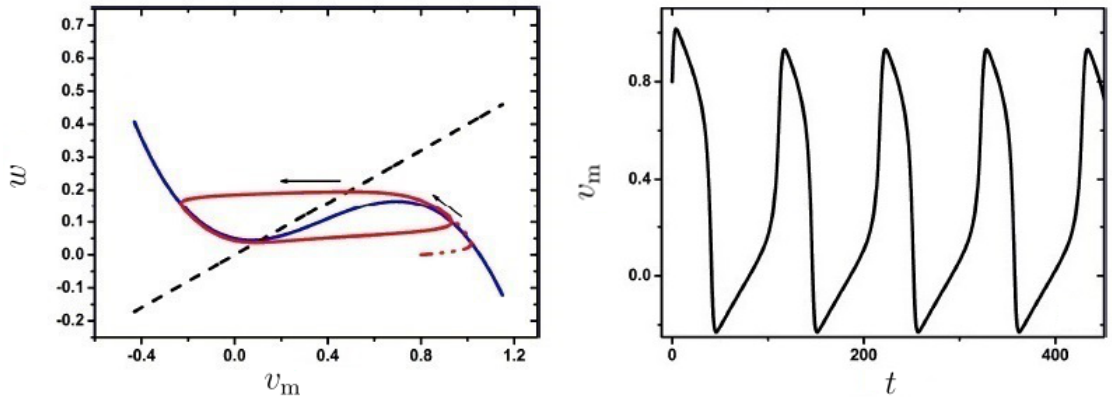

(b) Phase space plot with variables settling on a closed trajectory and the corresponding bursting-type action potential

Figure 2.5: Different behaviors of a nonlinear dynamical system.

of v_m, it is difficult to write explicitly the equilibrium v_m^* as a function of the bifurcation parameter ν. Instead, we rewrite the stimulus amplitude ν as a function of the equilibrium v_m^*:

$$\nu(v_m^*) = -k(v_m^* - v_1)(v_2 - v_m^*)(v_m^* - v_3) + (\beta v_m^* + \delta)/\gamma, \tag{2.18}$$

where v_m^* is the value of action potential at the equilibrium. Therefore, by finding the conditions in which the system has an unstable equilibrium and limit cycle, we can then derive the corresponding values for the stimulus amplitude using Eq. (2.18). In this work,

we are interested in the case when there is always only one equilibrium in the FHN model whatever the stimulus amplitude ν, for which the parameters should satisfy the following condition (see Appendix A):

$$\Delta_1 \triangleq (v_1 + v_2 + v_3)^2 - 3(v_1 v_2 + v_1 v_3 + v_2 v_3) - \frac{3\beta}{k\gamma} < 0. \tag{2.19}$$

Using bifurcation analysis (see Appendix A), we identify the following condition under which the FHN model has an unstable equilibrium and also a limit cycle:

$$\frac{v_1 + v_2 + v_3 - \sqrt{\Delta_2}}{3} < v_{\mathrm{m}}^* < \frac{v_1 + v_2 + v_3 + \sqrt{\Delta_2}}{3}, \tag{2.20}$$

where the parameters v_1, v_2, v_3, k, γ, ε_1, ε_2, c_{m} should satisfy

$$\Delta_2 = (v_1 + v_2 + v_3)^2 - 3(v_1 v_2 + v_1 v_3 + v_2 v_3) - \frac{3\varepsilon_1 \varepsilon_2 c_{\mathrm{m}} \gamma}{k} > 0. \tag{2.21}$$

Note that the parameters need to satisfy both $\Delta_1 < 0$ and $\Delta_2 > 0$, which introduces the following relationship:

$$\beta > \varepsilon_1 \varepsilon_2 c_{\mathrm{m}} \gamma^2. \tag{2.22}$$

With Eq. (2.18) and inequalities (2.19)–(2.21), we finally obtain the set of stimulus amplitude ν that leads to a limit cycle.

A periodic bursting-type action potential can then be derived by designing a stimulus amplitude so that the state of the FHN model periodically switches between a stable equilibrium and a limit cycle, hence producing a periodic spike trains. Here, we model the stimulus activity $\boldsymbol{J}_{\mathrm{stim}}$ using a periodic function with stimulus amplitude ν in the limit cycle range (a

value satisfying Eq. (2.18) and inequality (2.19)–(2.21)):

$$\boldsymbol{J}_{\text{stim}} = \frac{1}{\varepsilon_1}\nu h(t), \tag{2.23}$$

where $h(t) = h(t+T)$, which is a periodic function with frequency $f = 1/T$ that controls the time interval between trains of spikes and therefore consecutive contractions.

Frequency of bursting-type action potential Having an analytical expression that relates the spike frequency of a bursting-type action potential with the model parameters is useful for designing realistic action potentials. The FHN system exhibits oscillatory solution when it has a limit cycle other than an unstable equilibrium. With the analysis of eigenvalues during bifurcation analysis (see Appendix A), the oscillatory frequency of the FHN model in a limit cycle is

$$\omega = \sqrt{\frac{\varepsilon_2}{\varepsilon_1 c_{\text{m}}}} g(v_1, v_2, v_3, k, \beta, \delta, \gamma, \nu), \tag{2.24}$$

where $g(v_1, v_2, v_3, k, \beta, \delta, \gamma, \nu)$ is a function of v_1, v_2, v_3, k, β, δ, γ, ν. The frequency is proportional to the square root of ε_2 and inversely proportional to the square root of ε_1. We can therefore enhance the frequency of spike trains simply by either decreasing ε_1 or increasing ε_2.

2.3.2 Random conductivity tensor model at the tissue level

At the tissue level, we introduce a random conductivity tensor model that aims at better capturing the lack of global structure of the uterine fibers. The velocity of the transmembrane potential propagation is dependent on the myocyte fiber anisotropy. In order to take into account the myometrial fiber orientations, we assume a regular fiber structure, that is, we

define $\boldsymbol{a}_l(\boldsymbol{r})$ as a unit vector parallel to the main fiber orientation at a point $\boldsymbol{r}$. Following the procedure presented in our recent work [60], the conductivity tensors in a global coordinate system are given by

$$\boldsymbol{G}_{\mathrm{i}}^{'}(\boldsymbol{r}) = (\sigma_{\mathrm{il}} - \sigma_{\mathrm{it}})\boldsymbol{a}_3(\boldsymbol{r})\boldsymbol{a}_3^T(\boldsymbol{r}) + \sigma_{\mathrm{it}}\boldsymbol{I}_3, \tag{2.25}$$

$$\boldsymbol{G}_{\mathrm{e}}^{'}(\boldsymbol{r}) = (\sigma_{\mathrm{el}} - \sigma_{\mathrm{et}})\boldsymbol{a}_3(\boldsymbol{r})\boldsymbol{a}_3^T(\boldsymbol{r}) + \sigma_{\mathrm{et}}\boldsymbol{I}_3, \tag{2.26}$$

where $\boldsymbol{G}_{\mathrm{i}}^{'}(\boldsymbol{r})$ ($\boldsymbol{G}_{\mathrm{e}}^{'}(\boldsymbol{r})$) is the intra (extra) cellular conductivity tensor, σ_{il}, σ_{it} (σ_{el}, σ_{et}) are the longitudinal and transversal conductivity values of the intra (extra) cellular domain, respectively, $\boldsymbol{a}_3(\boldsymbol{r})$ is a basis vector that is parallel to $\boldsymbol{a}_l(\boldsymbol{r})$, and $\boldsymbol{I}_3$ denotes an identity matrix of size 3×3.

In our recent work [60], we represented the uterus as a hollow volume with uniform thickness and introduced a general framework for designing the tensor direction in the myometrium for an arbitrary uterine shape. Specifically, we presented the fiber orientation $\boldsymbol{a}_3(\boldsymbol{r})$ using its angle α with respect to a vector defined in the tangential plane at the point $\boldsymbol{r}$ (Fig. 2.6). The angle α can be modeled as a spatial basis function defined over the whole uterine domain. In the numerical example, however, we only considered a fixed fiber angle of $\pi/4$ for the whole myometrium (Fig. 2.7(a)). In this work, we define the fiber orientation using a finite element mesh. We divide the uterus into 25 contiguous regions, via random sampling of the finite elements within the myometrium model and resampling any point that lies less than 4 cm from its nearest neighbor. We compute the vector based on the surface normals at our uterus model mesh points for an arbitrary uterine shape. Given a mesh point $\boldsymbol{r}$, with surface

normal $\hat{\boldsymbol{n}}(\boldsymbol{r}) = [n_x, n_y, n_z]'$, the fiber orientation $\boldsymbol{a}_3(\boldsymbol{r})$ is defined as

$$\boldsymbol{a}_3(\boldsymbol{r}) = \begin{pmatrix} \dfrac{n_x n_y \cos(\alpha) - n_z \sin(\alpha)}{\sqrt{n_x^2 + n_z^2}} \\ \sqrt{n_x^2 + n_z^2}\cos(\alpha) \\ \dfrac{n_z n_y \cos(\alpha) - n_x \sin(\alpha)}{\sqrt{n_x^2 + n_z^2}} \end{pmatrix}, \tag{2.27}$$

where α is the angle of the fiber with respect to the tangent vector. In this work, the vertical axis is the y axis rather than the z axis in [60]. In order to take into account the spatial variation of the fiber orientations, we assign a random fiber angle to each region of uterus by sampling from the normal distribution $(0, \pi/4)$ (Fig. 2.7(b)), where 0 denotes that the fiber is oriented along the vertical axis of the uterus.

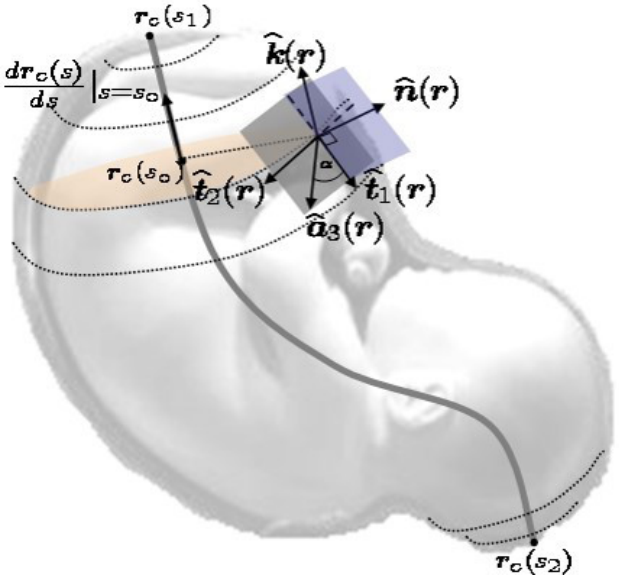

Figure 2.6: Illustration of the fiber orientation $\boldsymbol{a}_3(\boldsymbol{r})$ with respect to the fiber angle α.

Propagation speed of bursting-type potential In our recent work [60], we obtained an expression for the anisotropy ratio ζ by solving for a traveling wave with known propagation speed of plateau-type potential. In the following, we derive an expression for the speed of

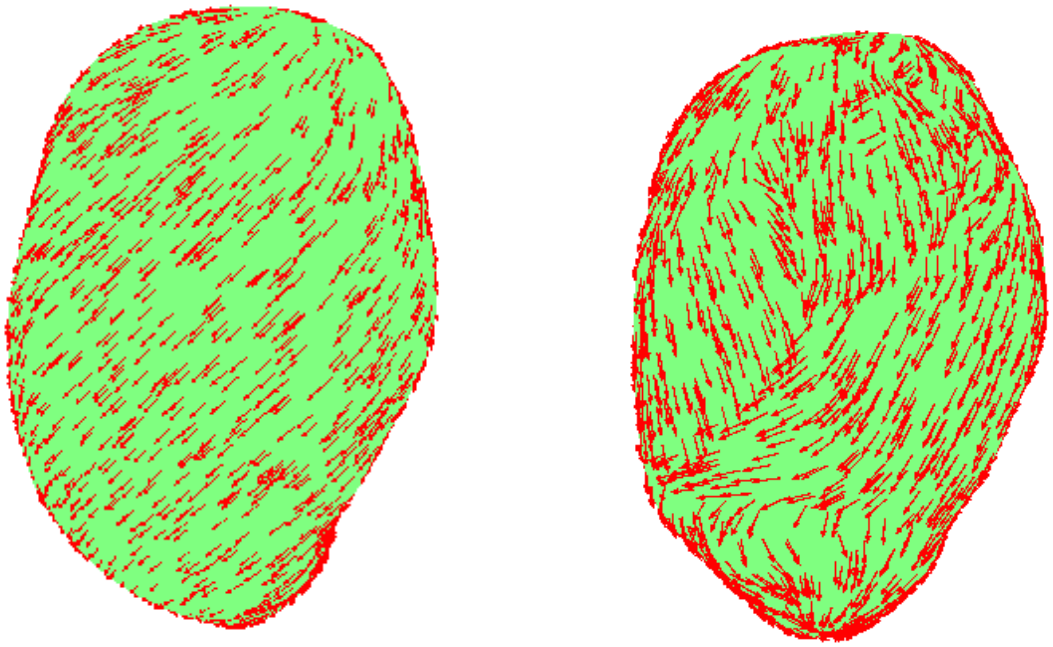

(a) Fixed fiber angle: $\alpha = \pi/4$ (b) Random fiber angle: $\alpha \sim \mathcal{N}(0, \pi/4)$

Figure 2.7: Fixed and random fiber angles of the myometrium.

propagation of the bursting-type potential by following a similar solution for the traveling wave with a fixed value of ζ.

A traveling wave is defined as a wave that travels without change of shape. The speed of propagation of the leading front of the waveform can then be taken as the wavespeed. Considering the leading front of a transmembrane potential, the variable w of the FHN model changes very slowly, which is then regarded to be set at the resting value that can be obtained through Eq. (2.17) as follows:

$$w = \frac{1}{\gamma}(\beta v_{\text{mr}} + \delta), \tag{2.28}$$

where v_{mr} is the resting potential. Replacing (2.28) in Eq. (2.6), the reaction diffusion equation is then presented by

$$\frac{\partial v_{\mathrm{m}}}{\partial t} = \frac{k}{\varepsilon_1 c_{\mathrm{m}}}((v_{\mathrm{m}} - v_1)(v_2 - v_{\mathrm{m}})(v_{\mathrm{m}} - v_3) - \frac{1}{k\gamma}(\beta v_{\mathrm{mr}} + \delta)) + \frac{\zeta}{\zeta + 1}\frac{\sigma_{\mathrm{el}}}{a_{\mathrm{m}} c_{\mathrm{m}}}\frac{\partial^2 v_{\mathrm{m}}}{\partial l^2}, \tag{2.29}$$

where a_{m} is the surface-to-volume ratio of the membrane. Eq. (2.29) matches with the standard form of the reaction diffusion equation for an excitable kinetics model in [65], whose wavespeed is given by

$$c = \frac{\tilde{v}_1 - 2\tilde{v}_2 + \tilde{v}_3}{c_{\mathrm{m}}}\left(\frac{k\sigma_{\mathrm{el}}\zeta}{2\varepsilon_1 a_{\mathrm{m}}(\zeta + 1)}\right)^{1/2}, \tag{2.30}$$

where $\tilde{v}_1$, $\tilde{v}_2$, and $\tilde{v}_3$ are the roots of the following polynomial

$$f(v_{\mathrm{m}}) = (v_{\mathrm{m}} - v_1)(v_2 - v_{\mathrm{m}})(v_{\mathrm{m}} - v_3) - \frac{1}{k\gamma}(\beta v_{\mathrm{mr}} + \delta). \tag{2.31}$$

Note that the speed of propagation is proportional to the square root of the extracellular longitudinal conductivity σ_{el} and inversely proportional to the membrane capacitance c_{m} and the square root of surface-to-volume ratio a_{m}.

2.3.3 Realistic volume conductor model at the organ level

At the organ level, we create an anatomically realistic model for the volume conductor. Rather than using a simple spherical geometry for the uterus, we model the uterus based on the MRI of a real, pregnant, near-term woman. We adapt a uterine mesh from the FEMONUM project [66], creating a smooth 3D model for the organ with a uniform 1 cm thickness (Fig. 2.8(a)). Similarly, rather than using a spherical model for the abdomen, we

assume that when the mother leans against the SARA device, her abdomen will deform slightly to follow the device contour. Following this assumption, we create an abdominal model that follows the shape of the SARA device, offset from the front of the uterus by roughly 2 cm (Fig. 2.8(b)).

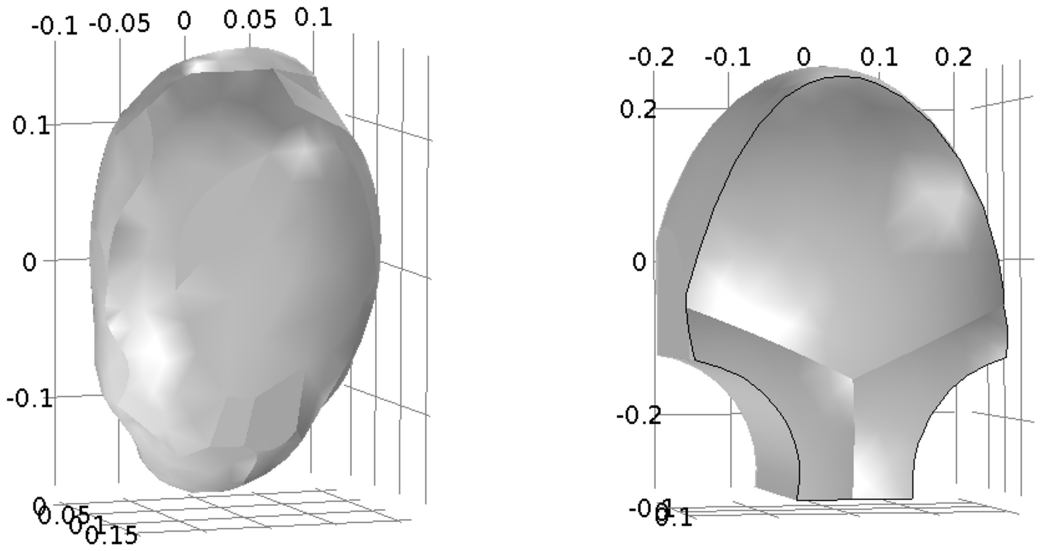

(a) Outer surface of the anatomical uterus (b) Outer surface of the SARA-based abdomen

Figure 2.8: Realistic uterus and abdomen models.

2.3.4 Sensor model on the abdominal surface

Finally, in order to obtain a more accurate simulation of magnetic field measurements, especially around the lower abdomen, we replicate the true sensor positions and sensing directions of the SARA device, rather than simply observing the normal component of the magnetic field at the abdomen. The SARA sensors are hardware magnetometers; each sensor measures the magnetic field at two coils (Fig. 1.4(c)). The first is on the inner surface of the device close to the mother's abdomen (denoted as B_1) and the second is displaced 8 cm from

the first in a direction roughly normal to the SARA surface (denoted as B_2). The recorded SARA measurement from the ith sensor is actually the difference between the fields at these two points, which is given by

$$B_i = B_{i1} - B_{i2}, \tag{2.32}$$

where $i = 1, 2, \cdots, 151$. This recording is very similar, but not identical, to the normal component of the magnetic field. This discrepancy is particularly notable in areas such as the lower central portion of the SARA device where the convexity of the surface results, due to space constraints in placing the sensors, in a non-negligible difference between the surface normal and the actual sensor orientation.

2.4 Summary of modeling assumptions

In this section, we list all the assumptions that are used to formulate the model:

1. Cellular level

   The uterus is formed by the same type of cells (myocyte) with cylindrically symmetric electrical conductivity. The myocyte can spontaneously initiate the electrical activity or can be excited by neighboring cells. The plateau-type and bursting-type action potentials are initiated in cells in the form of a stimulus current.

2. Tissue level

   Although there is no well-defined global fiber structure, the fibers in localized regions of the uterus have similar orientations. The conductivities of the intracellular and extracellular domains of the myometrium are inhomogeneous and anisotropic with

equal anisotropic ratio. The transmembrane potential travels across the myometrium without change of shape so that it can be considered as a traveling wave.

3. Organ level

   The volume conductor is modeled as four compartments with electrically conductive boundaries between compartments except for the external boundary of the abdomen. When leaning against the SARA device, the abdomen will deform to follow the SARA device shape. The anatomically realistic uterus with a layer of uniform-thickness wall is modeled based on the MRI of a pregnant, near-term woman. The uterus has inhomogeneous and anisotropic conductivity while the other three compartments are considered to be homogeneous and isotropic.

4. Electromagnetics

   The electromagnetic properties of uterine contractions are modeled using the quasi-static approximation of the Maxwell's Equations [67, 68]. We can use this approximation because bioelectromagnetic fields with frequency below 1 KHz vary slowly and the corresponding spatial length scale is much larger than the volume conductor of geometry. Changes in the bioelectric sources, therefore, affect the bioelectromagnetic fields instantaneously in the whole volume conductor of geometry. The displacement current, which is a result of the time-varying electric field, is much smaller than the ohmic current that results from ions flowing in the medium. Hence, the total current density in the volume conductor can be regarded as the ohmic current only.

2.5 Numerical examples

In this section, we evaluate our multiscale forward model at the cellular, tissue, and organ levels.

2.5.1 Cellular level

The plateau-type action potential under certain parameters was illustrated in our recent work [60]. To generate a bursting-type action potential, we computed the range of the stimulus current amplitude such that the FHN system, with model parameters given in Table 2.2, underwent a limit cycle behavior. Specifically, Δ_1 in this case is negative and Δ_2 is positive, hence by evaluating Eq. (2.18) and inequality (2.20), we obtained that ν should range between 0.012 and 0.207. We confirmed our computation with the bifurcation diagram (Fig. 2.9), which was generated using XPPAUT [69] that is an effective numerical tool for simulating, animating, and analyzing dynamical systems. The bifurcation parameter ν is shown on the horizontal axis and the vertical axis shows the values of the function. The red lines denote stable equilibria while the black lines are unstable equilibria. The green solid circles represent stable limit cycles while the blue ones refer to unstable limit cycles. Note that limit cycle behavior is produced when the stimulus current amplitude ν is between the two vertical lines.

The ionic current model is a nonlinear dynamical system of ordinary differential equations that can be solved numerically. We used MATLAB's built-in ode45 function, which includes the fourth order Runge-Kutta method, to validate our cellular-level model. We reproduced different types of action potentials (Fig. 2.10) by varying the stimulus current. Fig. 2.10(a)

Table 2.2: Ionic current model parameters.

Symbol	Value
c_{m}	0.01 [F/m^2]
ε_1	10 [Ωm^2]
ε_2	10 [s^{-1}]
v_1	-0.02 [V]
v_2	-0.04 [V]
v_3	-0.065 [V]
k	7000 [V^{-2}]
δ	0.052 [V]
γ	0.1
β	1

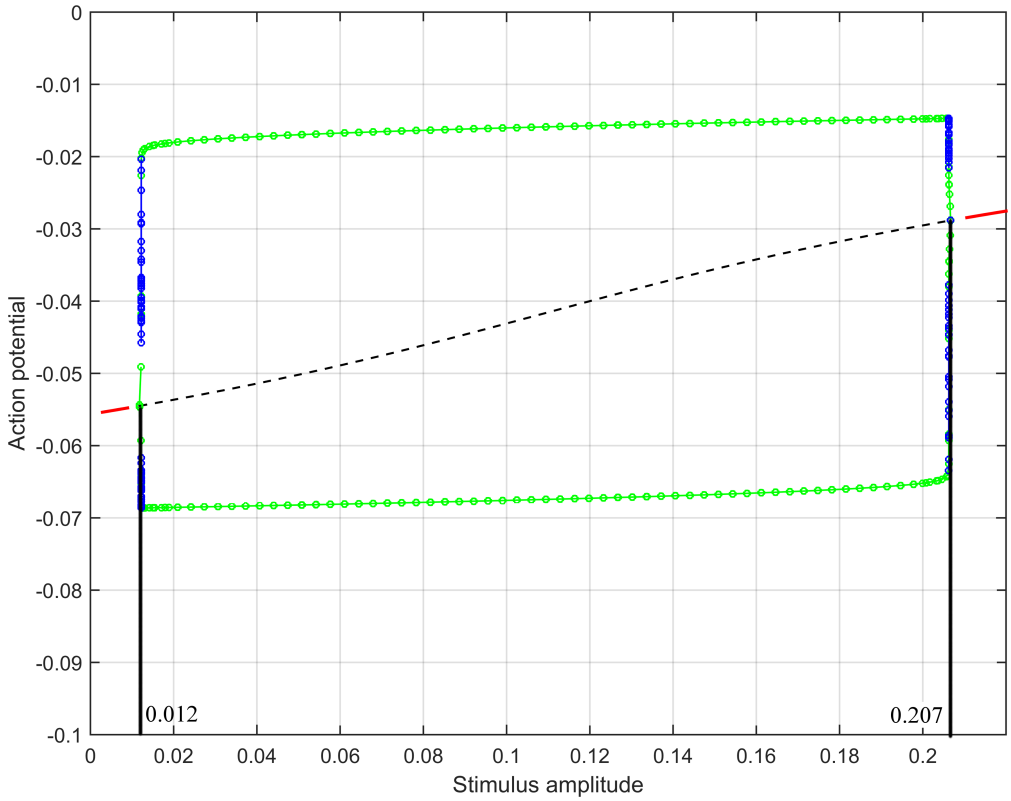

Figure 2.9: Bifurcation diagram, produced by XPPAUT, of action potential with respect to the variation of the stimulus current amplitude.

shows a plateau-type action potential, which was obtained by applying no stimulus current. In this case, a stable equilibrium exists in the FHN model. The system returns to the equilibrium point after experiencing an excitation, generating the plateau-type action potential. If the stimulus current is set to be 0.15 V, it falls in the limit cycle range and hence a bursting-type action potential will be generated (Fig. 2.10(b)). A periodic stimulus current that varies between the stable equilibrium and limit cycle ranges gives rise to periodic bursting-type action potentials. Fig. 2.10(c) shows an example of the periodic bursting-type action potential by applying a sinusoidal stimulus current with amplitude $\nu = 0.11$ V and frequency $f = 0.05$ Hz in Eq. (2.23).

Using as a reference the average bursting-type action potential that was recorded from isolated tissue strips of human myometrium at term [17], we designed the stimulus current of the generalized FHN model. In particular, as reported in [17] from the 39th week of pregnancy, the resting potential is approximately -56 mV and the interval between consecutive contractions is around 7 minutes. Therefore, in this numerical example, we introduced the Heaviside function, which is a unit step function whose value is zero for negative argument and one for positive argument, as the stimulus current. With a periodic Heaviside function whose duration is 1 minute and period is 7 minutes, the generated periodic bursting-type action potential is illustrated in Fig. 2.10(d). We observe that the resting potential of our model is -55.6 mV, and the interval between consecutive contractions is about 420 s, which are in fair agreement with the recorded values in [17].

Using the stimulus current in Fig. 2.10(b), we examined the relationship between the frequency of burstings and parameters ε_1 and ε_2 and the results are given in Table 2.3. We generated transmembrane potentials for different combinations of ε_1 and ε_2 values. It shows

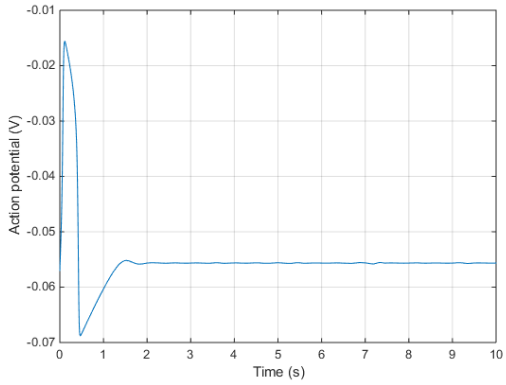

(a) Plateau-type action potential

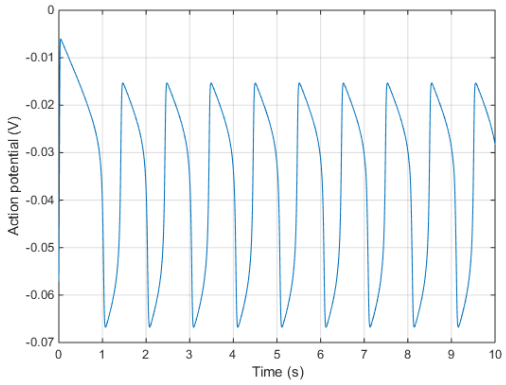

(b) Bursting-type action potential

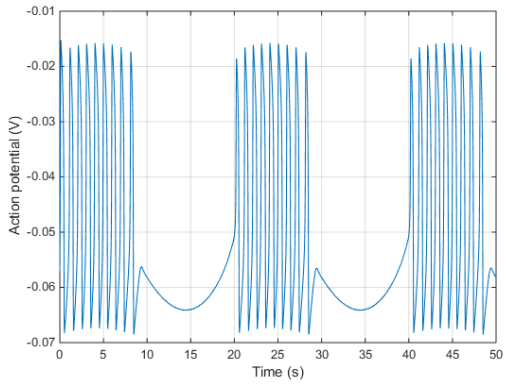

(c) Periodic bursting-type action potential under a sinusoidal stimulus

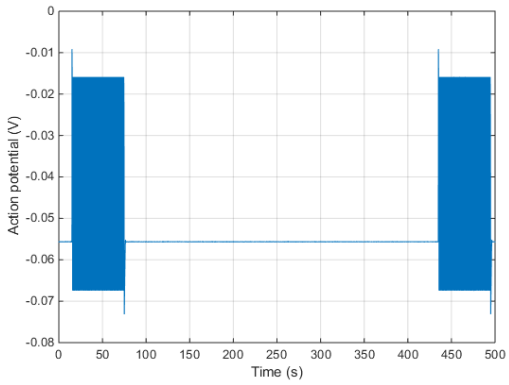

(d) Periodic bursting-type action potential under a periodic heaviside-function stimulus

Figure 2.10: Various action potentials by applying different stimuli.

that we are able to obtain a higher frequency with smaller ε_1 and larger ε_2, which is consistent with the relationship that is derived in Eq. (2.24).

2.5.2 Tissue level

Table 2.4 gives the parameter values (other than those included in Table 2.2) for the analysis of the propagation speed of the bursting-type potential. According to Eq. (2.30), the speed of propagation is 0.0429 m/s along the main fiber direction. In order to verify this speed,

Table 2.3: Frequency of spike trains (spiking/second).

ε_2 \ ε_1	1	2	3	4	5	6	7	8	9	10
1	0.164	0.161	0.159	0.156	0.154	0.151	0.149	0.147	0.145	0.143
2	0.333	0.323	0.313	0.302	0.294	0.286	0.278	0.270	0.263	0.256
3	0.488	0.458	0.444	0.431	0.429	0.425	0.408	0.400	0.392	0.377
4	0.606	0.588	0.571	0.556	0.541	0.532	0.526	0.510	0.502	0.495
5	0.769	0.741	0.714	0.690	0.667	0.645	0.625	0.606	0.600	0.581
6	0.870	0.847	0.833	0.800	0.769	0.741	0.733	0.720	0.707	0.693
7	1.042	1.000	0.947	0.918	0.882	0.861	0.840	0.833	0.800	0.769
8	1.200	1.190	1.087	1.020	1.000	0.962	0.926	0.893	0.861	0.820
9	1.333	1.277	1.200	1.136	1.111	1.064	1.020	1.000	0.980	0.943
10	1.556	1.429	1.304	1.250	1.200	1.154	1.111	1.071	1.034	1.020

the fiber angle α in Eq. (2.27) was set to be 0 so that the fibers lay along the vertical axis of the uterus. In our numerical simulation, we took the difference between the top and equator of uterus and find that the the speed at the equator is approximately 0.0421 m/s, which is a good match with the above theoretic value of wavespeed.

Table 2.4: Parameters for speed analysis.

Symbol	Value
a_{m}	575870 [m^{-1}]
v_{mr}	-0.056 [V]
σ_{el}	0.68 [S/m]
ζ	0.518

2.5.3 Organ level

We tested various configuration aspects, e.g., shape of uterus, shape of abdomen, fiber orientation, and initiation location, by simulating the abdomen-surface magnetic field using our multiscale forward model. Fig. 2.11 illustrates the simulation results of the abdominal

magnetic field under each configuration (the detailed configuration for each subfigure is given in Table 2.5). In [60], we illustrated the normal magnetic field for a spherical abdomen and one initiation on the fundus of a spherical myometrium with a fixed-angle fiber orientation (Fig. 2.11(a)). In order to investigate the sensitivity of MMG to each aspect in the configuration, we simulated the normal magnetic field with one aspect of the configuration changed in each numerical example (Fig. 2.11(b)–(e)) when compared with the original configuration in Fig. 2.11(a). Fig. 2.11(b) was generated by introducing an anatomical uterus developed from the FEMONUM project instead of the spherical uterus. It can be seen that the normal magnetic field pattern for the anatomical uterus is similar to that for the spherical uterus. In Fig. 2.11(c), the normal magnetic field pattern over a SARA-shape abdomen is presented. We observe that no significant difference is introduced into the abdominal magnetic field by the abdomen shape change. Fig. 2.11(d) illustrates the normal magnetic field for a random fiber orientation sampled from a normal distribution, which displays a significantly different pattern from that for a fixed-angle fiber orientation. The normal magnetic field pattern for initiation located at the lateral of the uterus is given in Fig. 2.11(e). It is obvious that the propagation direction of magnetic field is significantly influenced by the location of the initiation area. Fig. 2.11(f) presents the magnetic field pattern after applying the sensor model, which replicates the true SARA sensor readings, to the configuration in Fig. 2.11(c). It is shown that significant difference of the magnetic field pattern is introduced at the lower abdomen by the SARA sensor model.

2.5.4 Initial validation with real data

Matching a simulation for a full contraction to a real contraction would require the optimization of many variables, such as the initiation location, initiation intensity, and fiber

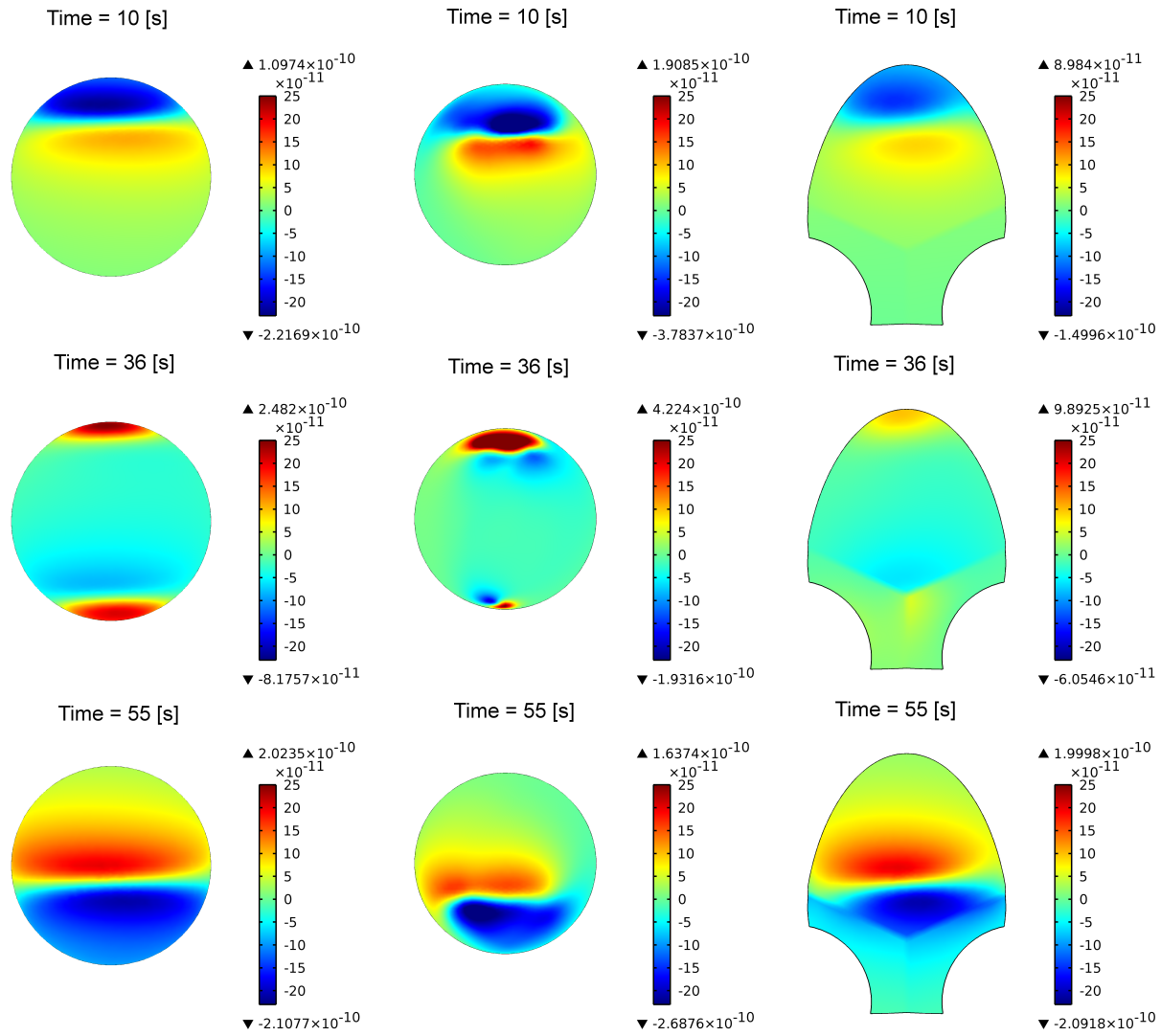

(a) Normal component (b) Normal component (c) Normal component

Figure 2.11: Simulated magnetic fields on the abdominal surface at time instants t = 10 [s], 36 [s], 55 [s] corresponding to Configures a – f in Table 2.5.

directions, and the consideration of complex scenarios such as one transmembrane potential taking a tortured path that travels across the whole uterus [33], or a transmembrane potential that travels confined within a restricted area and recruits other initiations in areas across the uterus [70,71]. In the second scenario, the locations and activation times of the recruited initiations must also be optimized. Without an inverse model, manually optimizing these

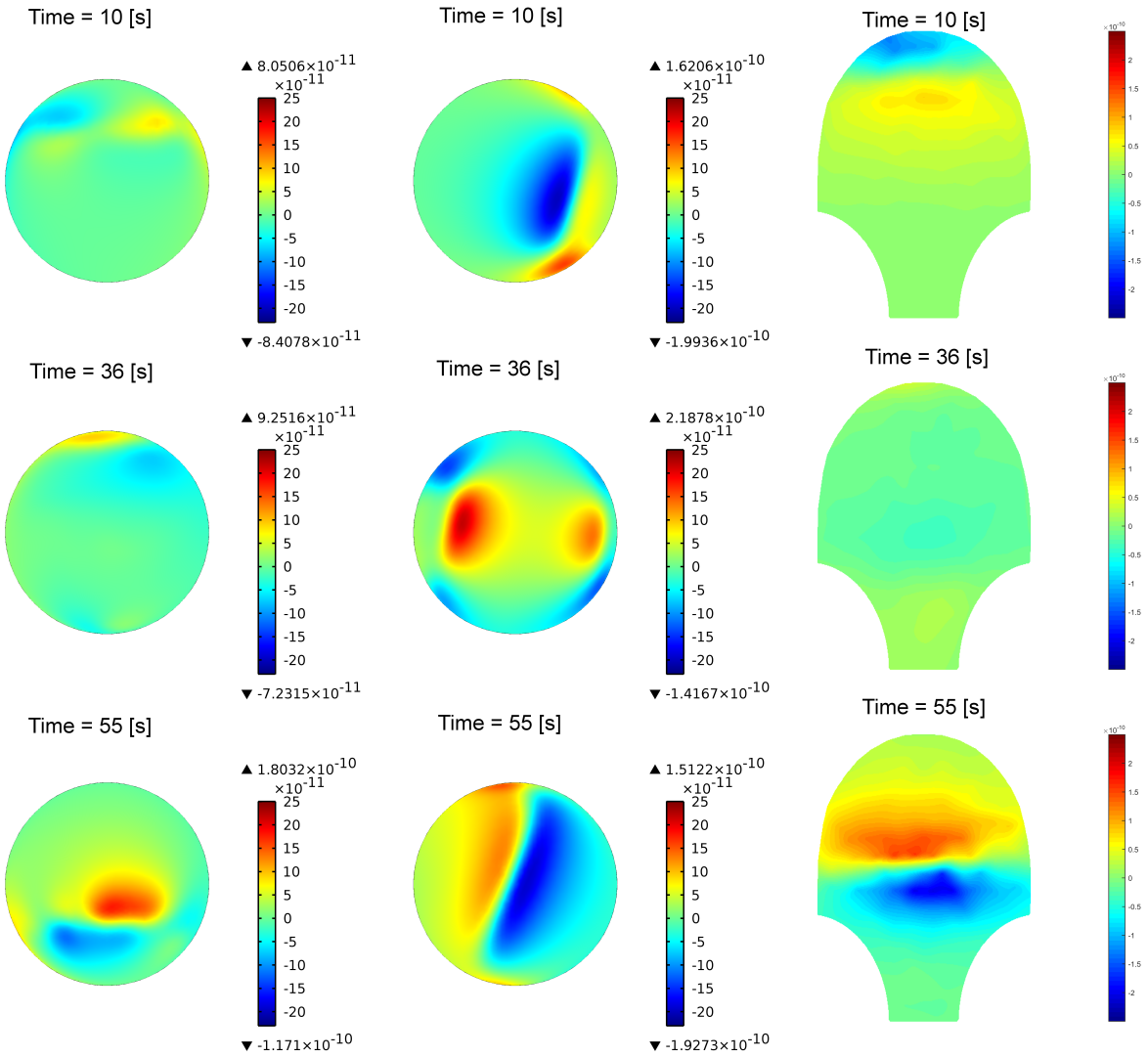

(d) Normal component (e) Normal component (f) Sensing component

Figure 2.11: Simulated magnetic fields on the abdominal surface at time instants t = 10 [s], 36 [s], 55 [s] corresponding to Configures a – f in Table 2.5 (cont.)

variables is infeasible. As such, we validate our model by comparing its magnetic field outputs during a limited portion of a uterine contraction with the real MMG data. Specifically, we match the MMG during the emergence and decay of contractions, when it is known that the contraction will be limited to a small region around a single initiation site.

Table 2.5: Detailed model configurations for Fig. 2.11.

Configuration / No.	Shape of uterus	Shape of abdomen	Fiber orientation	Initiation location	Sensor model
a	Sphere	Sphere	Fixed-angle	Fundus	No
b	FEMONUM	Sphere	Fixed-angle	Fundus	No
c	Sphere	SARA-shape	Fixed-angle	Fundus	No
d	Sphere	Sphere	Random	Fundus	No
e	Sphere	Sphere	Fixed-angle	Lateral	No
f	Sphere	SARA-shape	Fixed-angle	Fundus	Yes

The real data presented here was collected from a pregnant woman whose gestational age was 38 weeks and 4 days (see Section 1.4 for details of recording and preprocessing). The example MMG signal collected by Sensor MLJ4 of the SARA device (Fig. 2.12(a)) is presented in Fig. 2.12(b) and we chose to simulate the emergence and decay of one pre-labor uterine contraction, which are marked in red boxes (1050 s − 1065 s, 1135 s − 1150 s). Considering the alternating positive and negative magnetic field measurements, we decided to adopt the ionic current model that can generate bursting-type action potentials.

In our numerical example, we applied the simplified spherical uterus with a 16 cm radius measured from the center to the external boundary surface of the myometrium $\partial\mathcal{M}$ and assumed the uterine wall with a uniform thickness of 1 cm. The spherical abdominal compartment with a 21 cm radius was 2 cm offset from the front of the uterus. The spherical uterus and abdomen were chosen according to the above analysis at the organ level that the geometry has little impact in the magnetic field pattern. We also defined the fetus to be a solid sphere with a 12 cm radius concentric to the myometrium. The conductivity values of the homogeneous and isotropic compartments are listed in Table 2.6. The anisotropy of uterus was represented by the random conductivity tensor model and the surface normals

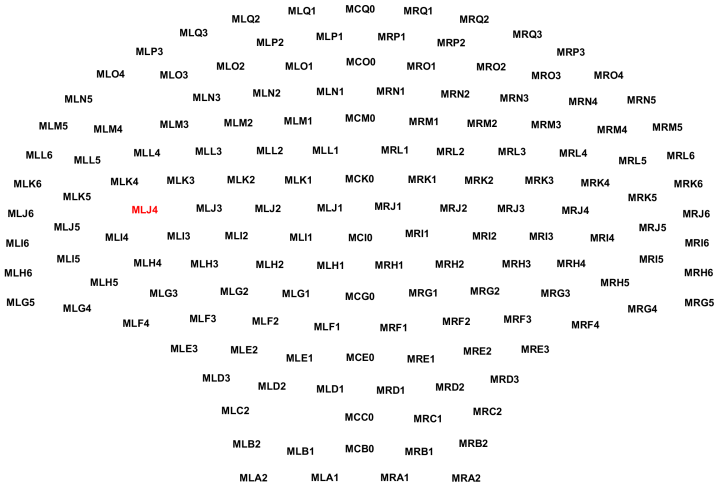

(a) The position of Sensor MLJ4 of the SARA device

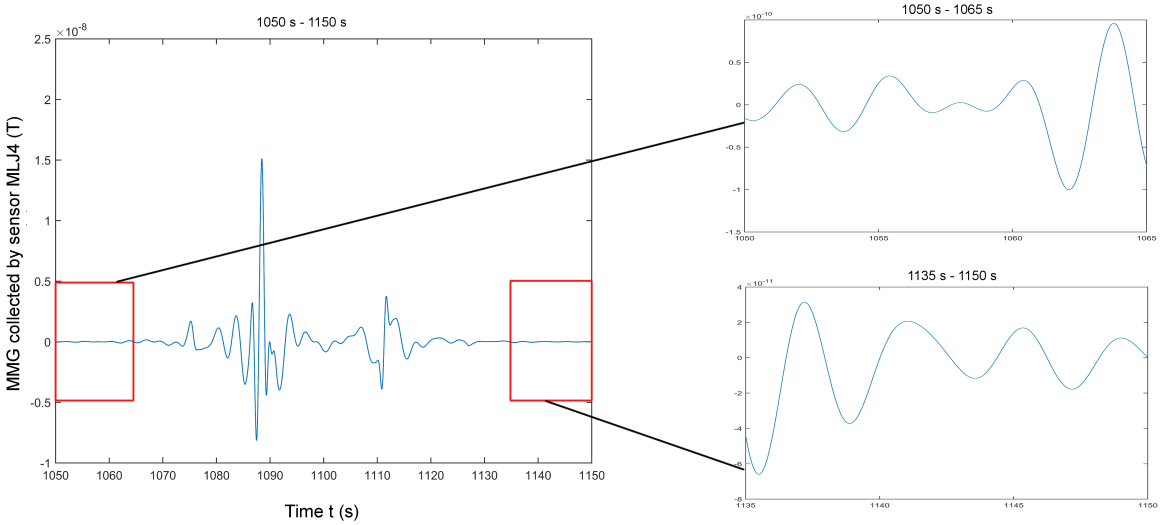

(b) The emergence and decay portions (1050 s – 1065 s, 1135 s – 1150 s) of real subject data collected by Sensor MLJ4

Figure 2.12: The example trace of real subject data collected by Sensor MLJ4 of the SARA device.

were specified relative to the mesh points of the uterus. We randomly chose the conductivities of uterus to be either 0 or sampled from a normal distribution such that the average value matched the conductivity value in Table 2.4. We assumed that one initiation was

located at the back of the uterus, centered at $(0,\ 13.0,\ -7.5)$ cm. The stimulus current was represented by $\boldsymbol{J}_{\text{stim}}(\boldsymbol{r},t) = \frac{1}{\varepsilon_1} * V_{\text{stim}} * \text{heaviside}(t) * \text{heaviside}(T_{\text{stim}} - t) * \text{heaviside}(0.05 - ((y - \cos(-\frac{\pi}{6}) * 0.15)^2 + (z - \sin(-\frac{\pi}{6}) * 0.15)^2 + x^2)^{1/2}) * \cos(2\pi * 0.05 * (t - T_{\text{stim}}))$ with amplitude $V_{\text{stim}} = 0.11$ V and duration $T_{\text{stim}} = 5$ s.

Table 2.6: Conductivity values of the homogeneous and isotropic compartments.

Symbol	Value
$G_{\mathcal{A}}$	0.2 [S/m]
$G_{\mathcal{U}}$	1.74 [S/m]
$G_{\mathcal{F}}$	0.5 [S/m]
G_{air}	$5 * 10^{-15}$ [S/m]
ζ	0.818

The limited propagation of the bursting-type transmembrane potential, as expected during the emergence and decay of a new contraction, can be achieved either by simply electrically isolating the limited propagation area or, more realistically, by having region-specific ionic current model parameters. To test the more realistic limited-propagation approach, we set the ionic current model parameters to lie within the limit cycle range for the region of uterus less than 10 cm from the center of the initiation, and designed the parameters to be within the stable equilibrium range outside this region (see Table 2.7 for detailed parameters).

The computation of the electromagnetic fields on the uterine and abdominal surfaces was implemented using the finite element method (FEM) solver COMSOL Multiphysics version 4.3a on a server with 12 processors at 2.3 GHz and 64 GB RAM. We discretized the four-compartment volume conductor into 1,181,186 tetrahedral elements, which were allocated as: 109,237 elements in the additional compartment concentric to the abdomen with a 50 cm radius, 321,633 elements in the abdominal cavity, 555,180 elements in the myometrium, 190,289 elements in the intrauterine cavity, and 4,847 elements in the fetus. The uterine and abdominal surfaces were divided into 38,844 and 6,834 triangular elements, respectively.

Table 2.7: Region-specific ionic current model parameters.

Symbol	Value within propagation area	Value outside propagation area
c_{m}	0.01 [F/m^2]	0.01 [F/m^2]
ε_1	10 [Ωm^2]	200 [Ωm^2]
ε_2	10 [s^{-1}]	0.09 [s^{-1}]
v_1	-0.02 [V]	-0.02 [V]
v_2	-0.04 [V]	-0.04 [V]
v_3	-0.065 [V]	-0.065 [V]
k	7000 [V^{-2}]	10000 [V^{-2}]
δ	0.052 [V]	0.052 [V]
γ	0.1	0.1
β	1	1

After the discretization, the computations of transmembrane potential, electrical potential, and magnetic field were given in three steps. The first step to solve the 10-minutes uterine transmembrane potential required four and a half hours when the number of degree of freedom was 223,274, while the solution time in the second step for electrical potential was seven hours with the number of degree of freedom 1,440,961. In the computation of the abdominal magnetic field, the number of degree of freedom was 1,579,337 and the corresponding solution time was four hours when we applied the generalized minimal residual (GMRES) solver.

Fig. 2.13 shows several snapshots of the real subject MMG and the FEM solution of our forward model at three time instants within the limited propagation mode of a contraction (i.e., during the beginning or end of a contraction). Fig. 2.13(a) provides the magnetic field measurements of the pregnant woman during the two portions of a uterine contraction. Fig. 2.13(b) illustrates the simulated magnetic field on the abdominal surface and the corresponding transmembrane potential on the uterine surface is shown in Fig. 2.13(c). We observe that our multiscale forward model is able to capture certain features of the subject's

MMG recordings, such as the spreading pattern of magnetic field at different areas, by the proper placement of the initiation and the restriction of the propagation area.

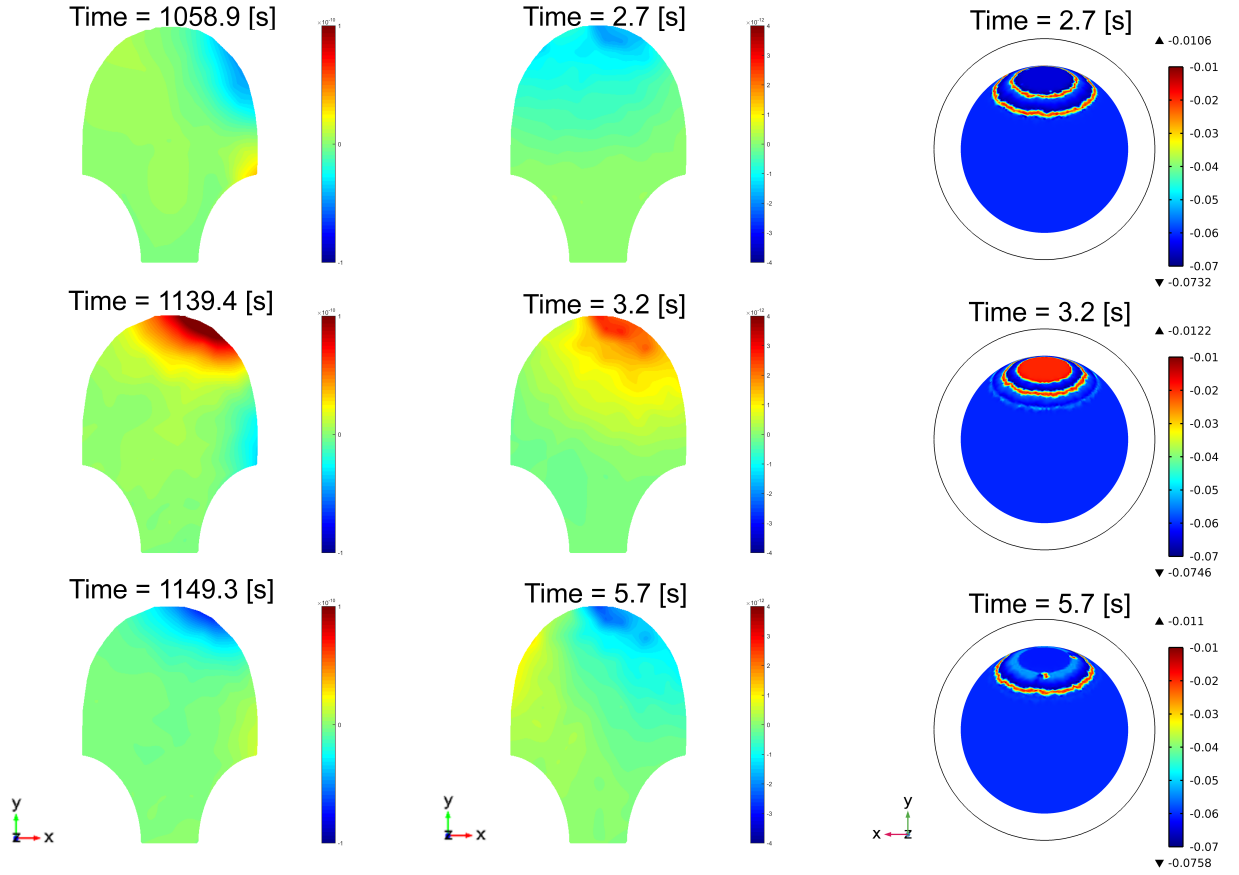

(a) Real subject data

(b) Simulated MMG

(c) Simulated transmembrane potential

Figure 2.13: Real subject MMG data and FEM solution of our forward model at different time instants.

2.6 Discussion

As an ionic current model, the FHN equations produced a fair approximation of the plateau-type action potential [60]. In this work, we generated a periodic bursting-type action potential by applying a periodic stimulus current into the FHN equations. Our simulation

result at the cellular level shows that the simple spikes in a burst depolarize to an average of -25 mV. However, the depolarization of bursting-type action potential in human myocytes reported in [17] is much smaller (-42 mV). Note that in [60], the authors pointed out that the model parameters v_1, v_2, v_3, and k control the range of v_{m}, which means that it is possible to generate a bursting-type action potential that matches experimental values in the literature through adjusting parameters.

In our previous work, the magnetic field was recognized as highly dependent on the fiber orientation of the myometrium. Our numerical simulation results (Fig. 2.11(a) and Fig. 2.11(d)) provide a good illustration that the direction and intensity of the magnetic field change significantly under different fiber orientations. The magnetic field recordings of pregnant women obtained using the SARA device also demonstrate the relationship between the pattern of the magnetic field and the complex fiber orientations. In order to obtain the best match to subject recordings, fiber orientations should ideally be accurate to each individual subject. Unfortunately, a widely accepted model of fiber architecture of the myometrium is currently unavailable [13]. The current technique is to study the global fiber structure based on magnetic resonance (MR) diffusion tensor imaging (DTI). However, it is difficult to get approval for MRI studies on pregnant women that are not medically indicated, thus making it challenging to obtain an accurate fiber structure for every pregnant woman. We can instead apply an averaged fiber structure of human myometrium that can be obtained from MRDTI studies on the subjects recruited in this project.

In our work, we assume that the abdomen follows the contour of the SARA device after the pregnant woman sits and leans her abdomen against the device. This abdominal model should be incorporated into our entire modeling if it could produce magnetic field that matches more with real data. However, the magnetic field measured at the realistic abdomen

(Fig. 2.11(c)) shows minimal changes when compared with that measured at the spherical abdomen (Fig. 2.11(a)). In this sense, a sphere is suitable to represent the geometry of the abdomen.

The spherical volume conductor geometry was thought to be an oversimplification of the true geometry so that a more realistic model needs to be developed. However, the simulation result for an anatomical uterus from the FEMONUM project (Fig. 2.11(b)) displays a quite similar magnetic field pattern to that for a spherical one (Fig. 2.11(a)). The spherical uterus assumption is appropriate for the SARA device analysis, since the shape of the SARA device is concave, which is related to the shape of the abdomen. Despite a variety of uterine shapes at different stages of pregnancy, a spherical geometry is therefore a good choice for simplified modeling without causing too much distortion.

It is expected that each uterine myocyte can act as a pacemaker as well as a pacefollower. In this work, we observe that the location of initiation has a significant impact on the magnetic field pattern (Fig. 2.11(e)). The sensitivity of propagating direction to initiation locations makes it possible for us to determine from real data where the initiation is located. Exploring the configurations that characterize specific contraction patterns is exactly what we want to achieve by developing the multiscale forward model of contractions in pregnant uterus.

Obtaining a better replication of real data in a relatively simple way is possible with the following steps. Regarding the volume conductor geometry, we propose to use the simple spherical model no matter which stage the pregnant woman is in and how her abdomen is deformed. Accurate modeling for the conductivity tensor and initiation location is important since they have a more significant effect on the pattern of magnetic field. The fiber orientation should be averaged to population according to the MR DTI. A periodic bursting-type action potential is introduced into our model by adding a periodic stimulus current in the FHN

model. In [56], the ionic current model with a simple constant stimulus current produces more complex action potentials other than the bursting-type one simply by adjusting the model parameters, which makes it a perfect candidate as our ionic current model.

The simulation of our multiscale forward model to match with real MMG data shows that our model is able to mimic the limited-propagation magnetic field patterns during the emergence and decay of a uterine contraction. Note that this result is obtained by applying an excitation at the back of the uterus, a random fiber direction, a simplified spherical volume conductor geometry, and region-specific ionic current model parameters. Our model, therefore, can flexibly mimic the magnetic field patterns at different stages of uterine contractions by simply changing the model configuration. Our modeling approach enables us to test for different scenarios hypothesized in the literature regarding the recruitment of different regions of uterus during a contraction [33, 70, 71].

Our initial validation on real data shows that reproducing the magnetic field patterns for a full uterine contraction process would require estimating model parameters for specific subject and setting appropriate model configurations as described in Table 2.5. In fact, based on our results, the magnetic field patterns are sensitive to ionic current model parameters, myometrial fiber orientation, and initiation location. To estimate the configurations that best predict the data of a particular subject, there is a need to formally solve the inverse problem for uterine contractions using our proposed multiscale model. Given the MMG measurements and our multiscale forward model, we can estimate the current density, conductivity tensor, and initiation location by solving the inverse problem. Developing the multiscale forward model is a prerequisite to solving the inverse problem, while solving the inverse problem bridges the multiscale modeling and clinical applications.

2.7 Summary

We developed a realistic multiscale forward model of contractions in the pregnant uterus jointly at the cellular, tissue, and organ levels. Our approach incorporated current electrophysiological and anatomical knowledge of uterine contractions to compute the abdominal magnetic field. At the cellular level, we introduced a variation of the FitzHugh-Nagumo equations to generate both plateau-type and bursting-type action potentials. Analytical expressions for the speed of propagation and frequency of the bursting potential were derived and validated using numerical examples. We also designed a random conductivity tensor model applicable to an arbitrary uterine shape at the tissue level. At the organ level, we introduced a realistic anatomical model for the volume conductor geometry, based on magnetic resonance images of a pregnant woman. In order to simulate the real measurements of the SARA device, we proposed an array sensor model on the abdominal surface. Finally, we investigated the sensitivity of the magnetic field pattern to the configuration aspects using numerical examples. Since the volume conductor geometry rarely changes the pattern of magnetic field, we conclude that the spherical shape approximates the geometry of the uterus and abdomen well. We demonstrate that the fiber orientation and initiation location have a great effect on the pattern of magnetic field. By appropriately setting the configurations of our multiscale forward model, we demonstrate that it can capture the key characteristics of the limited-propagation magnetic field pattern during the emergence and decay of the uterine contractions.

Chapter 3

Inverse Estimation of Uterine Source Currents[2]

In Chapter 2, we proposed a realistic multiscale electromagnetic forward model of contractile activities in the pregnant uterus. In this chapter, based on the developed model and by solving the inverse problem, we will investigate the inner uterine source currents that are responsible for the external magnetic fields on the abdominal surface.

In particular, we develop a linear forward approximation model, based on the quasistatic Maxwell's equations and a realistic four-compartment volume conductor, that relates the magnetic fields to the source currents on the uterine surface through a lead-field matrix. To compute the lead-field matrix, we use a finite element method that considers the anisotropic property of the myometrium. We estimate the source currents by minimizing a constrained least-squares problem to solve the non-uniqueness issue of the inverse problem. Because we lack the ground truth of the source current, we propose to predict the intrauterine pressure from our estimated source currents by using an absolute-value-based method and compare

[2]This chapter is based on M. Zhang, P. S. La Rosa, H. Eswaran, and A. Nehorai, "Estimating uterine source current during contractions using magnetomyography measurements," *to appear in PLOS ONE.*

the result with real abdominal deflection recorded during contractile activity. We test the feasibility of the lead-field matrix by displaying the lead fields that are generated by putative source currents at different locations in the myometrium: cervix and fundus, left and right, front and back. We then illustrate our method by using three synthetic MMG data sets, which are generated using our previously developed multiscale model of uterine contractions, and three real MMG data sets, one of which has simultaneous real abdominal deflection measurements. The numerical results demonstrate the ability of our method to capture the local contractile activity of human uterus during pregnancy. Moreover, the predicted intrauterine pressure is in fair agreement with the real abdominal deflection with respect to the timing of uterine contractions.

3.1 Introduction

It is an inverse problem to estimate the parameters of the source currents underlying uterine contractions, such as their locations and time courses, from electromagnetic measurements. Solving this inverse problem is important for understanding the physiological, functional, and pathological properties of the uterus, which can be helpful in the diagnosis of labor and treatment of obstetric syndromes associated with contractile dysfunction, such as preterm birth, post-term birth, and dysfunctional labor, to name a few. Uterine contractile dysfunction during pregnancy is a significant healthcare challenge that has long-term medical and financial consequences [2–4]. Therefore, investigating this inverse problem can lead to considerable clinical benefits for both mothers and children.

3.1.1 Previous approaches

There is little work focusing on estimating the source currents of uterine activities during pregnancy [72, 73]. In [72], the authors investigated this problem based on simulated electrohysterogram data, also known as EMG. However, EMG, which is recorded by electrodes attached to the abdomen and arises from the volume current, is strongly dependent upon tissue conductivity [40], resulting in severe attenuation when electrophysiological signals propagate to the abdominal surface. Unlike EMG signals, MMG signals are detectable outside the boundary of the skin without making electrical contact with the body and are independent of any kind of reference, thus ensuring that each sensor mainly records localized activity. Moreover, MMG is more strongly coupled to the primary current and is much less dependent on tissue conductivity [41]. The authors in [73] evaluated the ability of a simulated full-coverage biomagnetic device to non-invasively monitor uterine magnetic activities. The device, however, is currently unavailable for taking the MMG measurements. In [48], the SARA device is developed to non-invasively collect the abdominal MMG data of uterine contractions.

3.1.2 Our approach

In this work, derived from the quasistatic Maxwell's equations, we develop a linear forward model of the abdominal magnetic field of uterine contractile events with respect to source current dipoles in an anisotropic myometrium. Specifically, taking into account the complex volume conductor geometry, we apply the FEM method to numerically compute the lead-field matrix that represents the linear relation. We estimate the source currents by minimizing the least-squares error penalized by a ℓ_1 norm on the current dipoles, based on which we

predict the corresponding intrauterine pressure in order to explore its clinical implications. Using both synthetic MMG data, generated using our multiscale model of uterine contractions [74] presented in Chapter 2, and real MMG data sets, we show that the estimated source current distribution in the myometrium matches with the synthetic source current in the initiation and tissue recruitment in localized uterine contractions. We also validate that our contractile pressure prediction from the estimated source currents resembles the real abdominal deflection measurement, which is recorded simultaneously with the MMG data, in the timing of the contraction process. To the best of our knowledge, our results are the first to estimate source currents in the uterus during real contractions.

3.1.3 Mathematical notations

The mathematical notation used in this chapter is as follows: Italic lowercase or uppercase letters denote scalars; bold italic lowercase letters indicate vectors; bold italic uppercase letters denote matrices, except for vector fields, which are in bold calligraphic uppercase e.g., electric field $\boldsymbol{E}$, magnetic field $\boldsymbol{B}$, current density $\boldsymbol{J}$, and lead field $\boldsymbol{\mathcal{L}}$. The ℓ_1 and ℓ_2 norms defined in the Euclidean space are denoted by $\|\cdot\|_1$ and $\|\cdot\|_2$, respectively.

3.2 Real and synthetic data

The collection and preprocessing of real MMG data have already been presented in Section 1.4 of Chapter 1. In this section, we describe the measurement of uterine shape change that is recorded simultaneously with MMG and also the generation of synthetic MMG data.

Three real MMG data sets were used for the estimation of uterine source current. Among these data sets, one set has simultaneous recordings of the abdominal deflection, which were collected using an air-filled bag that was placed between the maternal abdomen and the SARA system. During uterine contractions, the pressure on the airbag induced by the abdominal shape change was transmitted via a tube to a pressure sensor that was connected to a standard fetal monitor which was located outside the shielded room. The output of the monitor was digitized and synchronized with the MMG signals. This simultaneous recording was performed as a proof of concept study and is difficult for routine application since noise artifacts could be introduced in the MMG data due to application of an external device.

Synthetic MMG data sets were also employed to test our estimation approach. These synthetic data sets were generated using our realistic multiscale electromagnetic model [74] which is detailed described in Chapter 2. The volume conductor in this model is exactly the same as the one in this inverse estimation work, and a sensor model is used to replicate the true SARA sensor positions and sensing directions as illustrated in Fig. 1.4. In particular, we represent the volume conductor as four compartments (from the inner layer to the outer layer: fetus, amniotic fluid, uterus, and abdomen) with electrically conductive boundaries between compartments (Fig. 3.1). Assuming the cylindrical symmetry of fibers, the average longitudinal and transversal conductivity values for the myometrium are 0.68 S/m and 0.22 S/m, respectively. The corresponding conductivity values for the abdomen, amniotic fluid, and fetus are 0.2 S/m, 1.74 S/m, and 0.5 S/m, respectively.

Considering that fundus is one possibility among the sites that the uterine electrical acitivity is observed to arise [75–77], we set the initiation to occur at the fundus in the simulations. The final synthetic MMG data was generated by adding white noise with 5 fV/$\sqrt{\text{Hz}}$ to the original synthetic time courses.

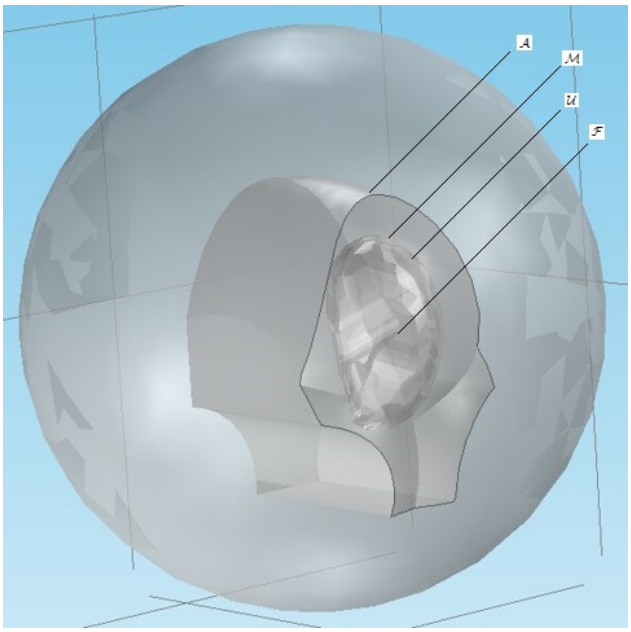

Figure 3.1: Four compartments of the volume conductor (from the outer layer to the inner layer): the abdominal cavity, $\mathcal{A}$; the myometrium, $\mathcal{M}$; the amniotic fluid, $\mathcal{U}$; and the fetus, $\mathcal{F}$.

3.3 Linear forward model

In this section, we introduce a linear forward model for the magnetic field based on a lead-field matrix that is constructed on the realistic four-compartment volume conductor.

3.3.1 Generation of electromagnetic fields

The electromagnetic fields of uterine contractions can be derived from the quasistatic approximation of Maxwell's equations, since the frequency of the associated bioelectrical phenomena is typically below 1 kHz. Thus the time derivatives of the electromagnetic fields can

be ignored as source terms. In the quasistatic approximation,

$$\nabla \times \boldsymbol{E} = 0, \tag{3.1}$$

$$\nabla \cdot \boldsymbol{E} = \frac{\rho}{\epsilon_0}, \tag{3.2}$$

$$\nabla \times \boldsymbol{B} = \mu_0 \boldsymbol{J}, \tag{3.3}$$

$$\nabla \cdot \boldsymbol{B} = 0, \tag{3.4}$$

where $\boldsymbol{E}$ and $\boldsymbol{B}$ are the electric and magnetic fields, respectively; ϵ_0 and μ_0 denote the permittivity and permeability of the free space, respectively; and ρ and $\boldsymbol{J}$ are the total charge density and current density, respectively. We divide the total current density, $\boldsymbol{J}(\boldsymbol{r})$, into two components: the volume current, $\boldsymbol{J}^{\mathrm{v}}(\boldsymbol{r}) = \sigma(\boldsymbol{r})\boldsymbol{E}(\boldsymbol{r})$, which is the result of the macroscopic electric field in the volume conductor, and the primary current, $\boldsymbol{J}^{\mathrm{p}}(\boldsymbol{r})$:

$$\begin{aligned} \boldsymbol{J}(\boldsymbol{r}) &= \boldsymbol{J}^{\mathrm{p}}(\boldsymbol{r}) + \boldsymbol{J}^{\mathrm{v}}(\boldsymbol{r}) \\ &= \boldsymbol{J}^{\mathrm{p}}(\boldsymbol{r}) + \sigma(\boldsymbol{r})\boldsymbol{E}(\boldsymbol{r}), \end{aligned} \tag{3.5}$$

where $\sigma(\boldsymbol{r})$ is the macroscopic conductivity of the volume conductor. The primary current, $\boldsymbol{J}^{\mathrm{p}}(\boldsymbol{r})$, is related to the original biological activity, which is the source current density we consider in this work. From Eq (3.1), the electric field, $\boldsymbol{E}$, can be represented as the negative gradient of a scalar electrical potential, V, as

$$\boldsymbol{E} = -\nabla V. \tag{3.6}$$

Therefore, the total current density in Eq (3.5) becomes

$$\boldsymbol{J}(\boldsymbol{r}) = \boldsymbol{J}^{\mathrm{p}}(\boldsymbol{r}) - \sigma(\boldsymbol{r})\nabla V(\boldsymbol{r}). \tag{3.7}$$

From Eqs (3.3) and (3.7), we obtain that $\nabla \cdot (\nabla \times \boldsymbol{B}) = 0 = \mu_0 \nabla \cdot \boldsymbol{J} = \mu_0 \nabla \cdot (\boldsymbol{J}^{\mathrm{p}} - \sigma \nabla V)$, hence

$$\nabla \cdot (\sigma \nabla V) = \nabla \cdot \boldsymbol{J}^{\mathrm{p}}, \tag{3.8}$$

which shows that the scalar electrical potential, V, can be solved analytically using FEM [78] given the source current density, $\boldsymbol{J}^{\mathrm{p}}$, and proper boundary conditions.

3.3.2 Linear approximation

The forward problem in uterine contractions is to calculate the magnetic field, $\boldsymbol{B}(\boldsymbol{r})$, outside the abdomen generated by the source current density, $\boldsymbol{J}^{\mathrm{p}}(\boldsymbol{r})$, within the uterus. According to the Biot-Savart law, the magnetic field can be computed as

$$\boldsymbol{B}(\boldsymbol{r}) = \frac{\mu_0}{4\pi} \int \frac{\boldsymbol{J}(\boldsymbol{r}') \times \boldsymbol{l}}{l^3}\, dv', \tag{3.9}$$

where $\boldsymbol{l} = \boldsymbol{r} - \boldsymbol{r}'$ is the vector pointing from the source point $\boldsymbol{r}'$ to the observation point $\boldsymbol{r}$ with magnitude $l = \|\boldsymbol{l}\|_2$. Here, the prime refers to quantities in the source region. Since

$\boldsymbol{l}/l^3 = -\nabla(1/l) = \nabla'(1/l)$, Eq (3.9) becomes

$$\begin{aligned}
\boldsymbol{B}(\boldsymbol{r}) &= \frac{\mu_0}{4\pi}\int \boldsymbol{J}(\boldsymbol{r}')\times\nabla'\frac{1}{l}\,dv' \\
&= \frac{\mu_0}{4\pi}\int\left(\frac{\nabla'\times\boldsymbol{J}(\boldsymbol{r}')}{l} - \nabla'\times\frac{\boldsymbol{J}(\boldsymbol{r}')}{l}\right)dv' \\
&= \frac{\mu_0}{4\pi}\int\frac{\nabla'\times\boldsymbol{J}(\boldsymbol{r}')}{l}\,dv' - \frac{\mu_0}{4\pi}\int\nabla'\times\frac{\boldsymbol{J}(\boldsymbol{r}')}{l}\,dv' \\
&= \frac{\mu_0}{4\pi}\int\frac{\nabla'\times\boldsymbol{J}(\boldsymbol{r}')}{l}\,dv' - \frac{\mu_0}{4\pi}\int\hat{\boldsymbol{n}}'\times\frac{\boldsymbol{J}(\boldsymbol{r}')}{l}\,ds',
\end{aligned} \tag{3.10}$$

where $\hat{\boldsymbol{n}}'$ is the unit normal vector pointing outwards the source surface. For the total current density that approaches zero sufficiently fast when the source point, $\boldsymbol{r}'$, goes to infinity, Eq (3.10) becomes

$$\boldsymbol{B}(\boldsymbol{r}) = \frac{\mu_0}{4\pi}\int\frac{\nabla'\times\boldsymbol{J}(\boldsymbol{r}')}{l}\,dv'. \tag{3.11}$$

With Eq (3.7),

$$\begin{aligned}
\boldsymbol{B}(\boldsymbol{r}) &= \frac{\mu_0}{4\pi}\int\frac{\nabla'\times(\boldsymbol{J}^{\mathrm{p}}(\boldsymbol{r}') - \sigma(\boldsymbol{r}')\nabla'V(\boldsymbol{r}'))}{l}\,dv' \\
&= \frac{\mu_0}{4\pi}\int\left(\frac{\nabla'\times\boldsymbol{J}^{\mathrm{p}}(\boldsymbol{r}')}{l} - \frac{\nabla'\times(\sigma(\boldsymbol{r}')\nabla'V(\boldsymbol{r}'))}{l}\right)dv'.
\end{aligned} \tag{3.12}$$

Since $\nabla\times(\sigma\nabla V) = \nabla\sigma\times\nabla V + \sigma\nabla\times\nabla V = \nabla\sigma\times\nabla V$,

$$\boldsymbol{B}(\boldsymbol{r}) = \frac{\mu_0}{4\pi}\int\left(\frac{\nabla'\times\boldsymbol{J}^{\mathrm{p}}(\boldsymbol{r}')}{l} - \frac{\nabla'\sigma(\boldsymbol{r}')\times\nabla'V(\boldsymbol{r}')}{l}\right)dv'. \tag{3.13}$$

With $\nabla\sigma \times \nabla V = V(\nabla \times \nabla\sigma) - \nabla \times (V\nabla\sigma) = -\nabla \times (V\nabla\sigma)$, the magnetic field, $\boldsymbol{B}$, is represented as

$$\begin{aligned}\boldsymbol{B}(\boldsymbol{r}) &= \frac{\mu_0}{4\pi}\int\left(\frac{\nabla' \times \boldsymbol{J}^{\mathrm{p}}(\boldsymbol{r}')}{l} + \frac{\nabla' \times (V(\boldsymbol{r}')\nabla'\sigma(\boldsymbol{r}'))}{l}\right) dv' \\ &= \frac{\mu_0}{4\pi}\int\frac{\nabla' \times (\boldsymbol{J}^{\mathrm{p}}(\boldsymbol{r}') + V(\boldsymbol{r}')\nabla'\sigma(\boldsymbol{r}'))}{l}\, dv'.\end{aligned} \tag{3.14}$$

Based on the equivalence between Eqs (3.9) and (3.11), we obtain from Eq (3.14) that

$$\boldsymbol{B}(\boldsymbol{r}) = \frac{\mu_0}{4\pi}\int(\boldsymbol{J}^{\mathrm{p}}(\boldsymbol{r}') + V(\boldsymbol{r}')\nabla'\sigma(\boldsymbol{r}')) \times \frac{\boldsymbol{l}}{l^3}\, dv'. \tag{3.15}$$

According to Eq (3.8), the electrical potential, V, in the above equation can be computed from the source current density, $\boldsymbol{J}^{\mathrm{p}}$, and is linearly related to $\boldsymbol{J}^{\mathrm{p}}$. Therefore, based on Eq (3.15), the magnetic field, $\boldsymbol{B}$, is linearly related to the source current density, $\boldsymbol{J}^{\mathrm{p}}$ [79]. Thus, there is a lead field, $\boldsymbol{\mathcal{L}}(\boldsymbol{r}, \boldsymbol{r}')$, relating the magnetic field measurement, $\boldsymbol{B}$, at $\boldsymbol{r}$ to the source current, $\boldsymbol{J}^{\mathrm{p}}$, at $\boldsymbol{r}'$, satisfying

$$\boldsymbol{B}(\boldsymbol{r}) = \int \boldsymbol{\mathcal{L}}(\boldsymbol{r}, \boldsymbol{r}') \cdot \boldsymbol{J}^{\mathrm{p}}(\boldsymbol{r}')\, dv'. \tag{3.16}$$

If the source current, $\boldsymbol{J}^{\mathrm{p}}$, is a current dipole with moment $\boldsymbol{q} = q\boldsymbol{d}_{\mathrm{q}}$ in location $\boldsymbol{r}_{\mathrm{q}}$, i.e., $\boldsymbol{J}^{\mathrm{p}}(\boldsymbol{r}) = \boldsymbol{q}\delta(\boldsymbol{r} - \boldsymbol{r}_{\mathrm{q}})$, the magnetic field is given by

$$\boldsymbol{B}(\boldsymbol{r}) = \boldsymbol{\mathcal{L}}(\boldsymbol{r}, \boldsymbol{r}_{\mathrm{q}}) \cdot \boldsymbol{q}, \tag{3.17}$$

where $\boldsymbol{q} = q\boldsymbol{d}_{\mathrm{q}}$ denotes a current dipole with magnitude q pointing at direction $\boldsymbol{d}_{\mathrm{q}}$.

For simplicity, the orientation of the current dipole is assumed to be perpendicular to the surface. When taking measurements using the SARA device, we cannot obtain all the components of the magnetic field; instead, we get a specific sensor-oriented component. Under these conditions, Eq (3.17) becomes

$$b(\boldsymbol{r}) = \mathcal{L}(\boldsymbol{r}, \boldsymbol{r}')q, \tag{3.18}$$

where b denotes the sensor-oriented magnetic field measurement that is generated by a normal current dipole with magnitude q. Note that according to Eq (3.18), the lead field $\mathcal{L}(\boldsymbol{r}, \boldsymbol{r}')$ is exactly the same as the magnetic field measurement b at $\boldsymbol{r}$ if we apply a unit normal current dipole with $q = 1$ at $\boldsymbol{r}'$. If the volume conductor is spherically symmetric and piecewise homogeneous, the lead field for the normal component of the magnetic field has a closed form [79]. However, it is a great challenge to obtain an explicit expression for the lead field in a complex volume conductor. We choose to solve this problem using FEM, which is a powerful tool for numerically solving for the lead field since it can deal with the anisotropy and realistic geometry in our volume conductor.

In this work, considering the random initiation area [22,23], we adopt the distributed source current instead of a small number of current dipoles. In this case, a much larger number (usually greater than $5,000$) of current dipoles are distributed over the whole myometrium. Since the myometrium is a thin layer [9], it is feasible for us to assume that the source current is limited to the external uterine surface. We divide the external uterine surface into small elements and introduce a current dipole at every vertex of the elements. Therefore, the lead field $\mathcal{L}(\boldsymbol{r}_i, \boldsymbol{r}'_j)$ is the numerical solution $b(\boldsymbol{r}_i)$ of the sensor-oriented magnetic field at sensor

location $\boldsymbol{r}_i$ generated by a unit current dipole at $\boldsymbol{r}'_j$, i.e.,

$$\mathcal{L}(\boldsymbol{r}_i, \boldsymbol{r}'_j) = b(\boldsymbol{r}_i) \triangleq g(\boldsymbol{r}_i, \boldsymbol{r}'_j),\ i = 1, 2, \ldots, M,\ j = 1, 2, \ldots, N, \tag{3.19}$$

where M is the number of SARA sensors and N denotes the number of current dipoles. The linear relationship between the current dipole amplitudes $\boldsymbol{q}_t$ and the measurements $\boldsymbol{b}_t$ at time t, therefore, is given by

$$\boldsymbol{b}_t = \begin{bmatrix} b_t(\boldsymbol{r}_1) \\ \vdots \\ b_t(\boldsymbol{r}_M) \end{bmatrix} = \begin{bmatrix} g(\boldsymbol{r}_1, \boldsymbol{r}'_1) & \ldots & g(\boldsymbol{r}_1, \boldsymbol{r}'_N) \\ \vdots & \ddots & \vdots \\ g(\boldsymbol{r}_M, \boldsymbol{r}'_1) & \ldots & g(\boldsymbol{r}_M, \boldsymbol{r}'_N) \end{bmatrix} \begin{bmatrix} q_t(\boldsymbol{r}'_1) \\ \vdots \\ q_t(\boldsymbol{r}'_N) \end{bmatrix} = \boldsymbol{G}\boldsymbol{q}_t,\ t = 1, 2, \ldots, T, \tag{3.20}$$

where

1. $b_t(\boldsymbol{r}_i),\ i = 1, 2, \ldots, M$ is the magnetic field measured by ith sensor at time t;
2. $q_t(\boldsymbol{r}'_j),\ j = 1, 2, \ldots, N$ is the amplitude of the jth current dipole at time t;
3. $\boldsymbol{G} = \{g(\boldsymbol{r}_i, \boldsymbol{r}'_j),\ i = 1, 2, \ldots, M,\ j = 1, 2, \ldots, N\}$ is the lead-field matrix, with $g(\boldsymbol{r}_i, \boldsymbol{r}'_j)$ obtained using Eq (3.19).

3.4 Inverse estimation of source currents

The data collected by all sensors at time t can be expressed as

$$\boldsymbol{b}_t = \boldsymbol{G}\boldsymbol{q}_t + \boldsymbol{e}_t, \tag{3.21}$$

for $t = 1, 2, \ldots, T$, where $\boldsymbol{e}_t$ is the measurement noise at time t. With the constructed lead-field matrix $\boldsymbol{G}$, we are interested in estimating the current dipole amplitudes $\boldsymbol{q}_t$ from the magnetic fields $\boldsymbol{b}_t$ measured using the SARA device. In the MMG inverse estimation problem, the number of unknowns, N, is usually greater than $5,000$, but the number of measurements, M, is about one hundred. Because of this ill-posed nature, the inverse problem has an identifiability issue, in that there is no unique mathematically correct solution for the problem. To resolve this issue, it is necessary to impose additional constrains on the current dipoles. Here, we are interested in the most significant source currents, hence we embed extra information as an ℓ_1 norm on the current distribution [80]. The resulting convex optimization problem is known as the Lasso problem [81]:

$$\hat{\boldsymbol{q}}_t = \arg\min_{\boldsymbol{q}_t} \frac{1}{2}\|\boldsymbol{b}_t - \boldsymbol{G}\boldsymbol{q}_t\|_2^2 + \lambda\|\boldsymbol{q}_t\|_1, \quad t = 1, 2, \ldots, T, \tag{3.22}$$

where λ is a regularization parameter balancing the least-squares error and the ℓ_1 penalty. A small λ puts more emphasis on the least-squares error, whereas large values of λ emphasize the ℓ_1 penalty. Applying convex optimization algorithms [82], we can obtain the source current amplitudes after solving this Lasso problem.

3.5 Prediction of intrauterine pressure

Clinically, uterine contraction is measured using either an external measuring device (TOCO) or internal pressure device (IUPC). The TOCO technique is widely used by physicians as it is simple and almost risk free to the mother and the fetus, but is qualitative only and does not reflect the contractile intensity. IUPC is considered as a gold standard for assessing the uterine contractions during labor. Uterine catheterization, however, is an invasive procedure

that requires the rupture of the amniotic membranes. In this work, to show that our work has clinical implications even without the ground truth of source currents, we predict the intrauterine pressure from our estimated source currents.

The amplitude of the contractile pressure varies based on the uterine shape change. We employ an absolute-value-based method [83] to predict the contractile pressure from our estimated source currents. To each estimated source current at each location, we first apply a 4th-order low-pass Butterworth filter with a cut-off frequency of 2 Hz and then downsample the source currents with a sampling frequency of 4 Hz to lower the computational complexity. After rectifying the source currents, we obtain the approximate energy by summing over all locations. We then smooth the energy by applying a 4th-order low-pass Butterworth filter with a cut-off frequency of 0.02 Hz and resample at the original sampling frequency, resulting in our predicted contractile pressure measurement.

3.6 Numerical examples

In this section, we first illustrate the constructed lead-field matrix and then present numerical examples using both synthetic and real MMG data to illustrate our approach.

For the construction of the lead-field matrix, we divided the external uterine surface into 12,412 vertices, i.e., $N = 12,412$. The sensor-oriented magnetic field is measured on the abdominal surface using the SARA device with 151 sensors, i.e., $M = 151$. The constructed lead-field matrix $\boldsymbol{G}$ is therefore a 151-by-12,412 matrix, corresponding to the SARA device with 151 sensors and 12,412 unit current dipoles on the external uterine surface.

3.6.1 Validation of the constructed lead-field matrix

We displayed the lead fields corresponding to particular source locations on the SARA device to test the feasibility of the constructed lead-field matrix $\boldsymbol{G}$. In order to present the relationship between the lead field and source location and distance, the specific source locations were chosen to be pairs, such as cervix and fundus, left and right, front and back (from the front perspective). The corresponding results are illustrated in Figs. 3.2-3.4. The values of the spatial coordinates (x, y, z) are expressed in meters. Figs. 3.2 and 3.3 show the source coordinates at the cervix $(-0.022, -0.153, 0.007)$, fundus $(0.044, 0.150, 0.038)$, left $(-0.109, 0.0007, 0.101)$, and right $(0.106, -0.0004, 0.098)$ and the corresponding lead fields. We observe that the magnetic field patterns appear at the corresponding surrounding areas of the sources. The lead fields generated by the sources at the front $(0.001, -0.075, 0.148)$ and back $(-0.0001, -0.075, 0.014)$ of the uterus are presented in Fig. 3.4. Note that the magnetic-field intensity generated by a source at the front is higher than that generated by the one at the back, which is in agreement with the inverse square nature of magnetic field with respect to the distance between source and observation points.

3.6.2 Estimation using synthetic MMG data

We utilized three synthetic MMG data sets (see details in Table 3.1 and Figs. 3.5-3.7) to test our inverse estimation approach. Since fundus is one of the sites where uterine contractions are observed to arise [75–77], we excited the uterine activity at the upper left (from the rear perspective) of the uterus in the simulations. The parameters of the cell-level model in our multiscale model were set to generate plateau-type and bursting-type action potentials, which are the two predominant types in both a single uterine smooth muscle cell and isolated

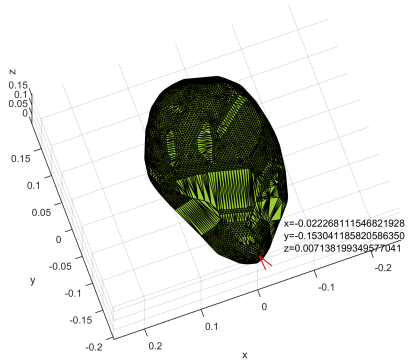

(a) A unit current dipole at the cervix $(-0.022, -0.153, 0.007)$

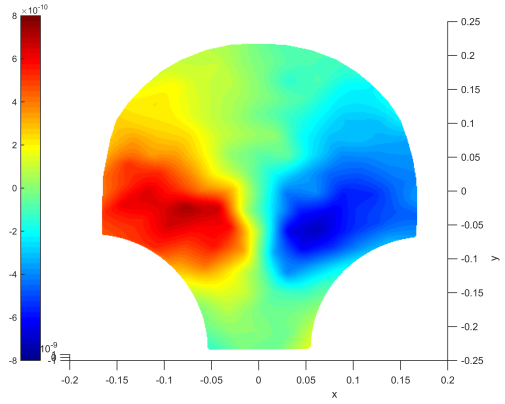

(b) The corresponding lead field generated by the unit current dipole at the cervix

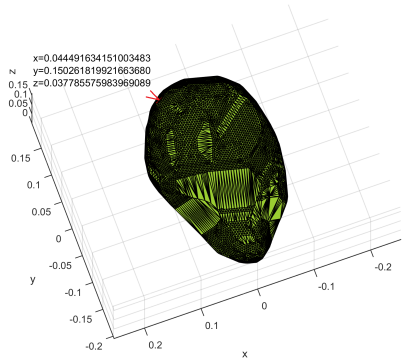

(c) A unit current dipole at the fundus $(0.044, 0.150, 0.038)$

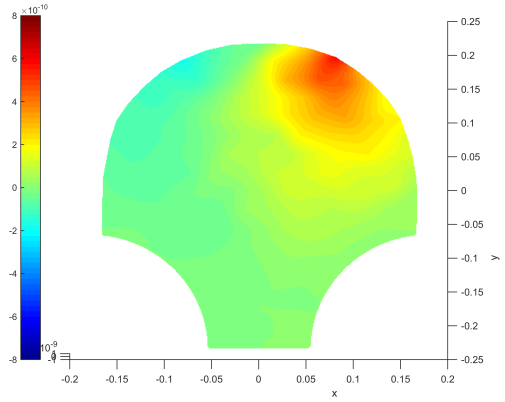

(d) The corresponding lead field generated by the unit current dipole at the fundus

Figure 3.2: Lead fields corresponding to unit current dipoles (locations highlighted in red) at the cervix and fundus of the uterus.

strips of myometrium [17, 25]. In each simulation, the sampling frequency was 10 Hz with simulation length of 10 s. We obtained the synthetic MMG data $\boldsymbol{b}_t$, $t = 1, 2, \ldots, 100$ as 100 151-by-1 vectors and the lead-field matrix $\boldsymbol{G}$ as a 151-by-12,412 matrix, i.e., $M = 151$, $N = 12,412$, and $T = 100$.

The initiation area of the first two synthetic MMG data sets is illustrated in Fig. 3.8, in which the uterus is drawn in blue with the initiation area highlighted in green. The contour

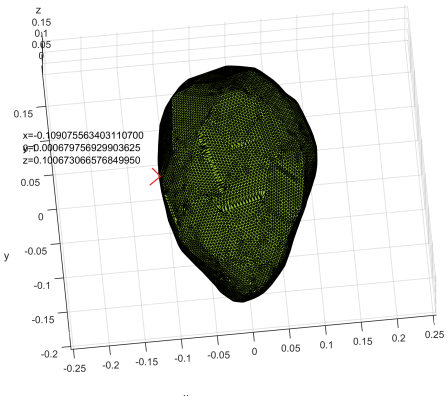

(a) A unit current dipole on the left side $(-0.109, 0.0007, 0.101)$

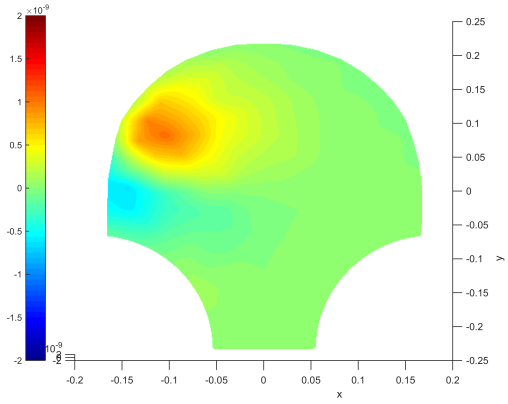

(b) The corresponding lead field generated by the unit current dipole on the left

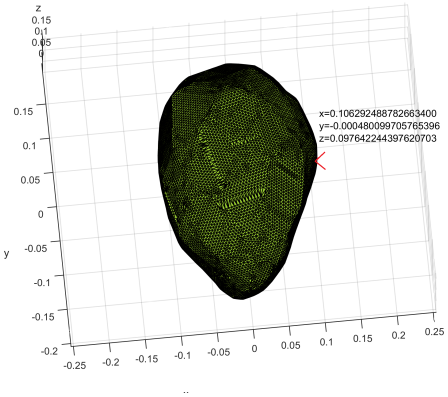

(c) A unit current dipole on the right side $(0.106, -0.0004, 0.098)$

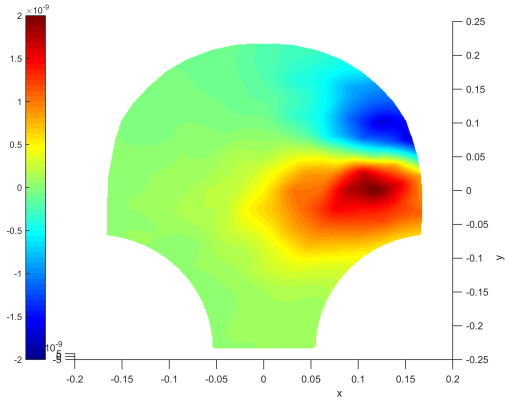

(d) The corresponding lead field generated by the unit current dipole on the right

Figure 3.3: Lead fields corresponding to unit current dipoles (locations highlighted in red) on the left and right side of the uterus.

Table 3.1: Details of three synthetic MMG data sets.

Data set	Initiation area	Action potential	Sampling frequency	M	N	T
1	1	plateau	10 Hz	151	12,412	100
2	1	bursting	10 Hz	151	12,412	100
3	2	bursting	10 Hz	151	12,412	100

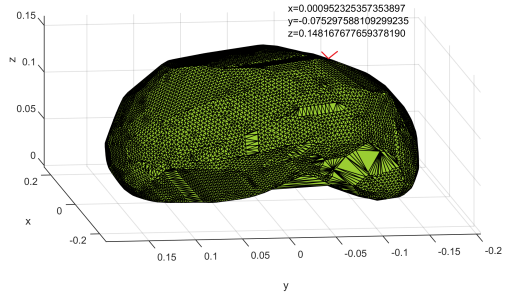

(a) A unit current dipole on the front side $(0.001, -0.075, 0.148)$

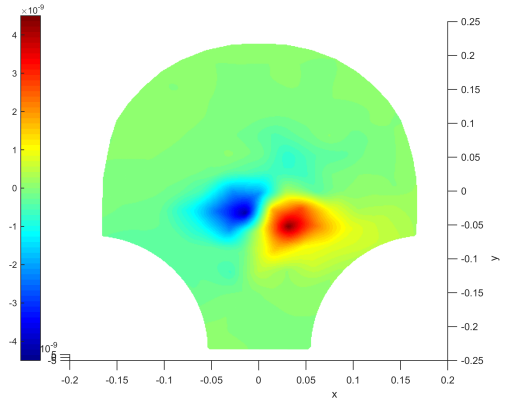

(b) The corresponding lead field generated by the unit current dipole on the front

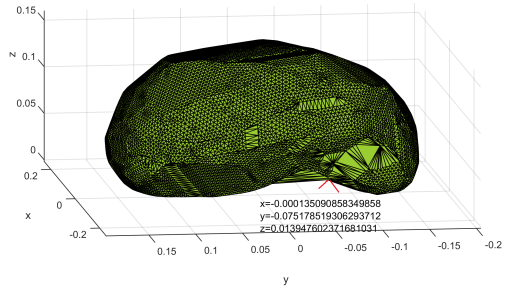

(c) A unit current dipole on the back side $(-0.0001, -0.075, 0.014)$

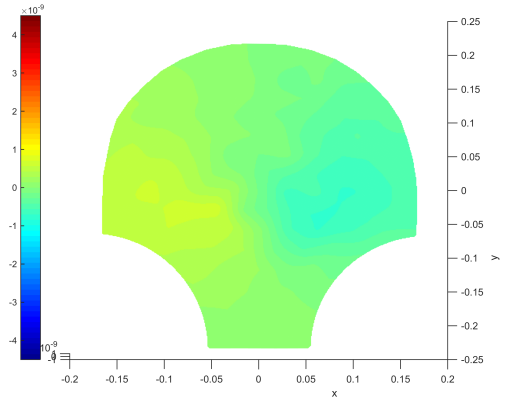

(d) The corresponding lead field generated by the unit current dipole on the back

Figure 3.4: Lead fields corresponding to unit current dipoles (locations highlighted in red) on the front and back side of the uterus.

of the SARA device is sketched in black curves. The first data set represents the short-time oscillations of magnetic field (Fig. 3.5(a)), that correspond to plateau-type action potential recruiting a small region in the upper left of the uterus (Fig. 3.5(c)). In the second data set, local activity of bursting-type action potential (Fig. 3.6(c)) was adopted to generate long-time oscillations of magnetic field (Fig. 3.6(a)). Regarding the change of pacemaker locations during a single contraction or successive contractions [23], we shifted the initiation

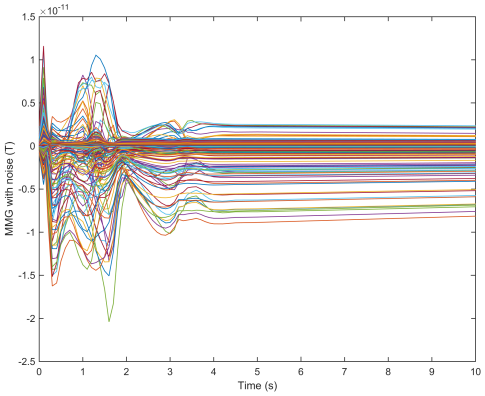

(a) Synthetic MMG over all SARA sensors

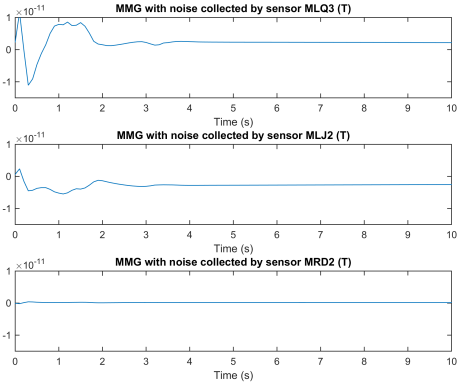

(b) Example traces from sensors MLQ3, MLJ2, and MRD2, respectively

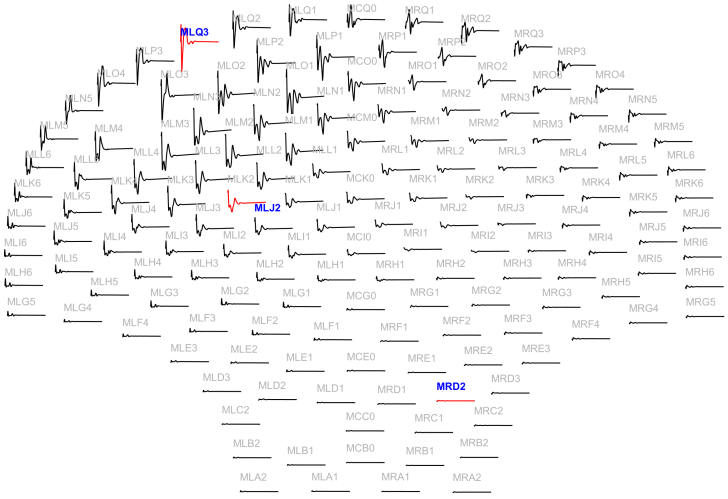

(c) Layout plot over SARA device

Figure 3.5: Sensor temporal courses of synthetic MMG Data set 1 in Table 3.1.

area from the location illustrated in Fig. 3.9(a) to that in Fig. 3.9(b) during one contraction, resulting in a local contractile activity shown in Fig. 3.7(c).

In the literature, there are many ways to define the regularization parameter λ [84]. In general, the degree of the regularization should be consistent with the level of noise involved in the measurements. Therefore, the regularization parameter λ was set to be a little bit

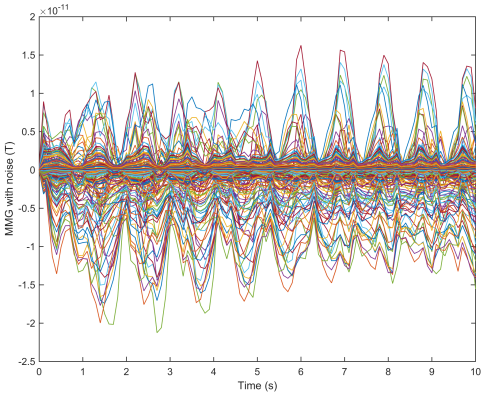

(a) Synthetic MMG over all SARA sensors

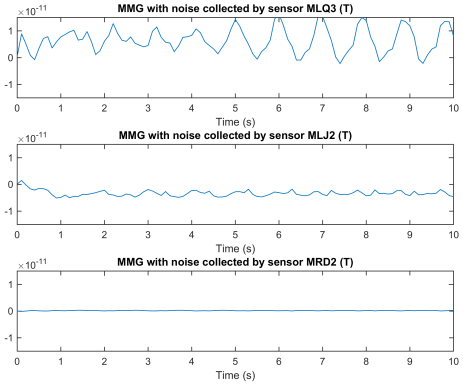

(b) Example traces from sensors MLQ3, MLJ2, and MRD2, respectively

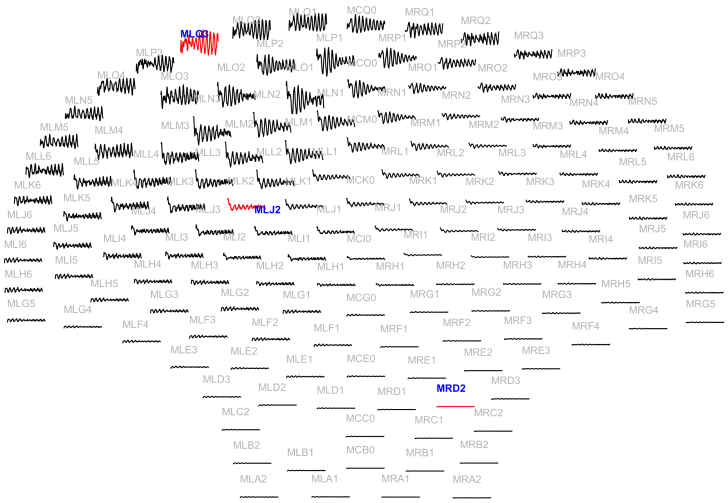

(c) Layout plot over SARA device

Figure 3.6: Sensor temporal courses of synthetic MMG Data set 2 in Table 3.1.

greater than the noise in our estimation. The choice of the regularization parameter is beyond the scope of this work.

Fig 3.10 shows the time courses of the estimated source currents for Data Set 1 in Table 3.1. Here, we were interested in the ones with higher intensity, hence set the threshold of the

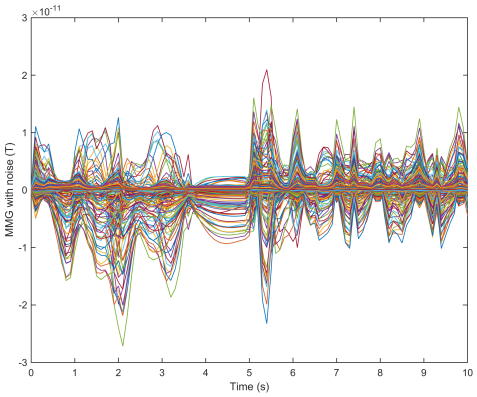

(a) Synthetic MMG over all SARA sensors

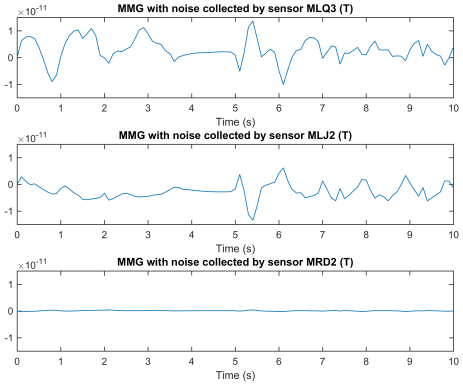

(b) Example traces from sensors MLQ3, MLJ2, and MRD2, respectively

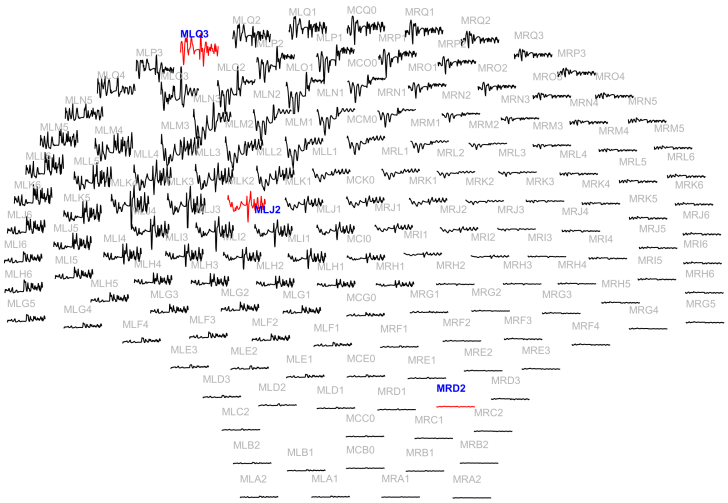

(c) Layout plot over SARA device

Figure 3.7: Sensor temporal courses of synthetic MMG Data set 3 in Table 3.1.

absolute value of amplitudes to be 2×10^{-5}. Fig. 3.11(a) illustrates snapshots of the estimated source currents on the uterine surface after thresholding at different time instants $t = 0.5$ s, 1.0 s, 2.0 s. The synthetic source currents generated using our multiscale model are presented as the Arrow Surface (red arrows on the uterine surface) in Fig. 3.11(b), in which the synthetic MMG on the uterine surface is also displayed. Red arrows in this figure

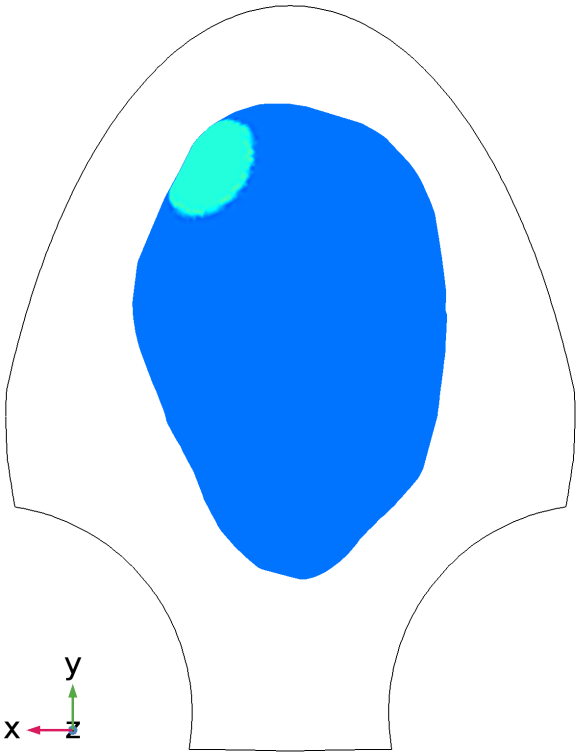

Figure 3.8: Location of the initiation area in the uterus for Data Sets 1 and 2 in Table 3.1. Blue, uterus; green, initiation area; black, the contour of SARA device.

reflect the direction of the source current. We observe that the synthetic source currents are distributed in a small local region in the upper left of the uterus at the beginning, then appear in a constrained neighboring region, and finally return to quiescence. Comparing Fig. 3.11(a) with Fig. 3.11(b), we can see that the distribution area of the estimated source currents resembles that of the synthetic ones, although it is not exactly the same. Furthermore, while we did not consider the tangential component of the source current, the estimated source currents capture the emergence of local activities and the involvement of a larger excited area in the following contractile activities, which are in agreement with the tissue recruitment and contraction coordination via limited action potential propagation in local contractions.

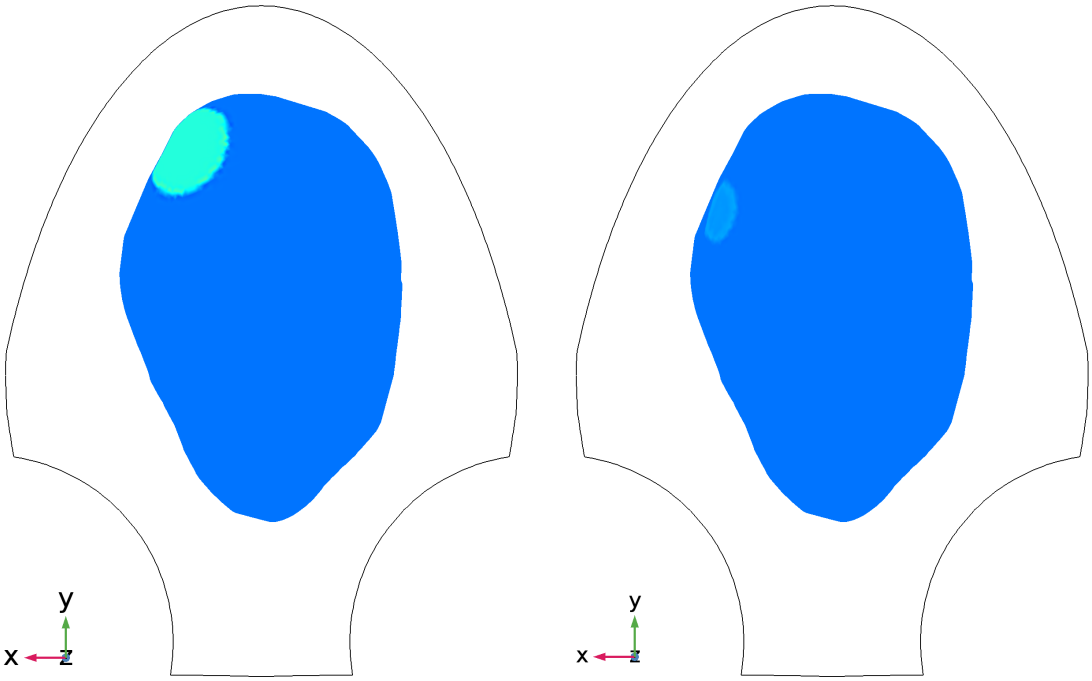

(a) The first location

(b) The second location

Figure 3.9: Locations of the initiation area in the uterus for Data Set 3 in Table 3.1. Blue, uterus; green, initiation areas; black, the contour of SARA device.

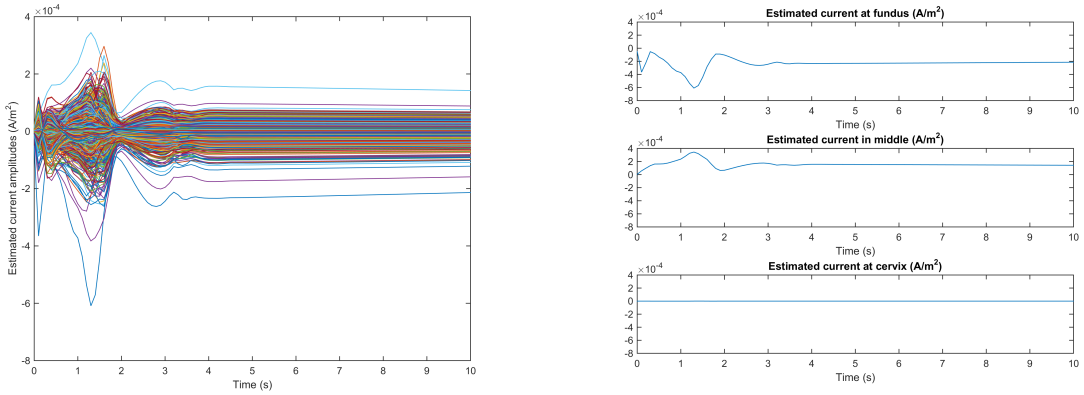

(a) Estimated source current amplitudes at all source locations

(b) Example traces of estimated source current amplitudes at the fundus, middle, and cervix of the uterus, respectively

Figure 3.10: Temporal courses of estimated source current amplitudes for Data Set 1 in Table 3.1.

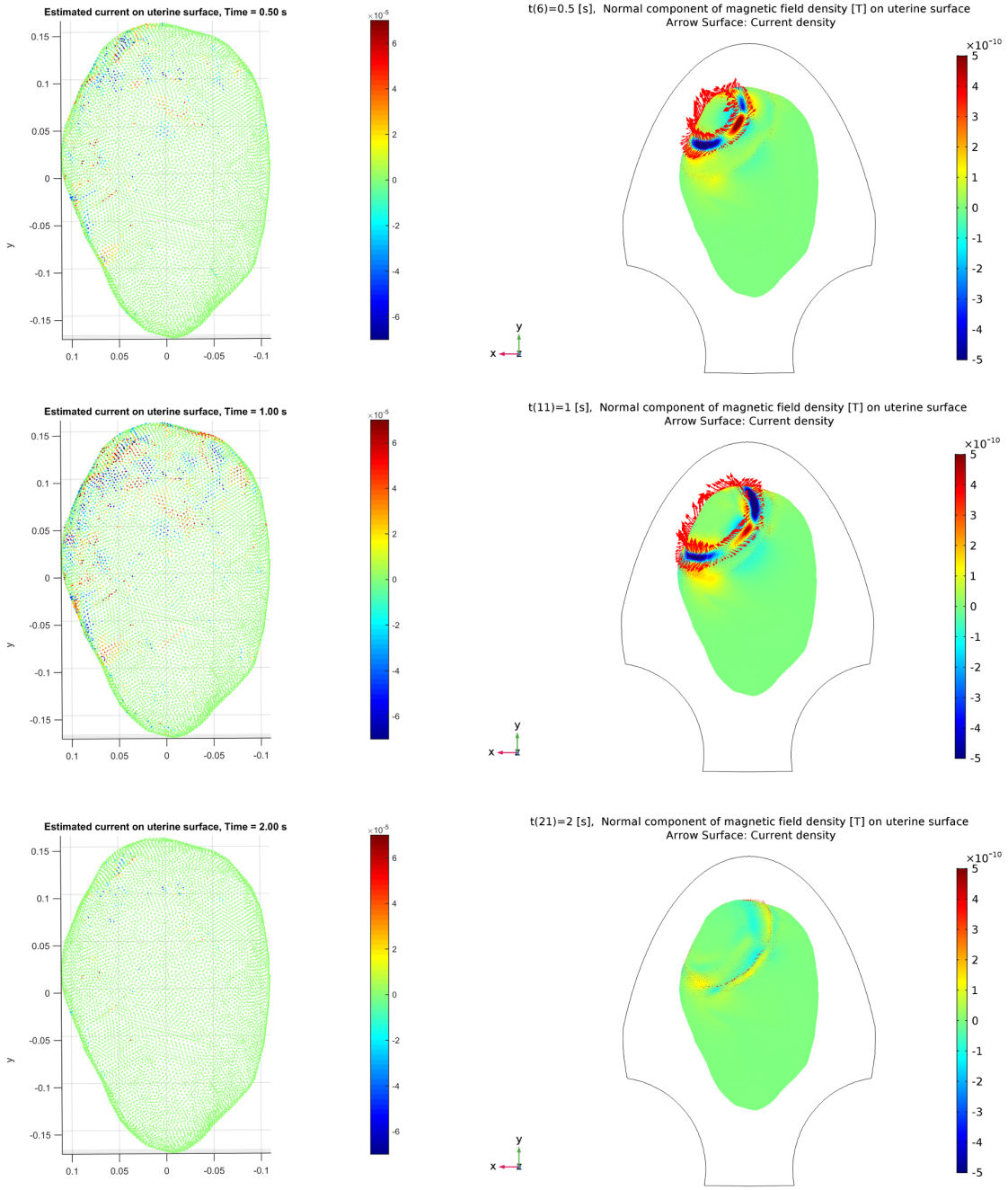

(a) Estimated source current amplitudes

(b) Synthetic source current amplitudes generated by our multiscale model

Figure 3.11: Estimated and synthetic source current amplitudes at time instants $t = 0.5$ [s], 1.0 [s], 2.0 [s] for Data Set 1 in Table 3.1.

The snapshots of the estimated source currents for Data Sets 2 and 3 in Table 3.1 are illustrated in Figs. 3.12 and 3.13, respectively. We observe that similar results are obtained for both data sets, i.e., the occurrence of local activity and recruitment of neighboring area for the synthetic and estimated source currents are fairly well matched. Note from the results at different time instants, $t = 2.8$ s and $t = 7.0$ s, in Fig. 3.13 that the estimated source currents reflect the change of the excited area from the upper left to a relatively lower position during the contraction, due to the initiation area change as shown in Fig. 3.9.

3.6.3 Estimation using real MMG data

We validated our inverse estimation method using three real data sets (see details in Table 3.2). The temporal courses of signals after preprocessing are presented in Figs. 3.14-3.16. Among these three data sets, Data set 1 includes simultaneous MMG and abdominal deflection recordings. The temporal course MMG signals over SARA sensors of Data set 1 are illustrated in Fig. 3.14(a) with the corresponding abdominal deflection shown in Fig. 3.14(c). The noisy signals in the top are due to maternal motion rather than uterine contractile activity. We can see strong uterine activities in the lower right region of the abdomen (from the rear perspective). MMG signals after preprocessing of Data sets 2 and 3 are given in Figs. 3.15 and 3.16, respectively. In these two figures, subfigure a presents the layout plot of MMG signals over the SARA sensors with high-amplitude signals highlighted in red. The frequency spectrum in the frequency band of $0.1 - 1$ Hz obtained from sensors in region where strong uterine activities occur is given in subfigure c.

For the first MMG data set that lasts for 12 minutes, we removed MMG data from two noisy sensors and also removed two corresponding rows of the lead-field matrix, thus obtaining the

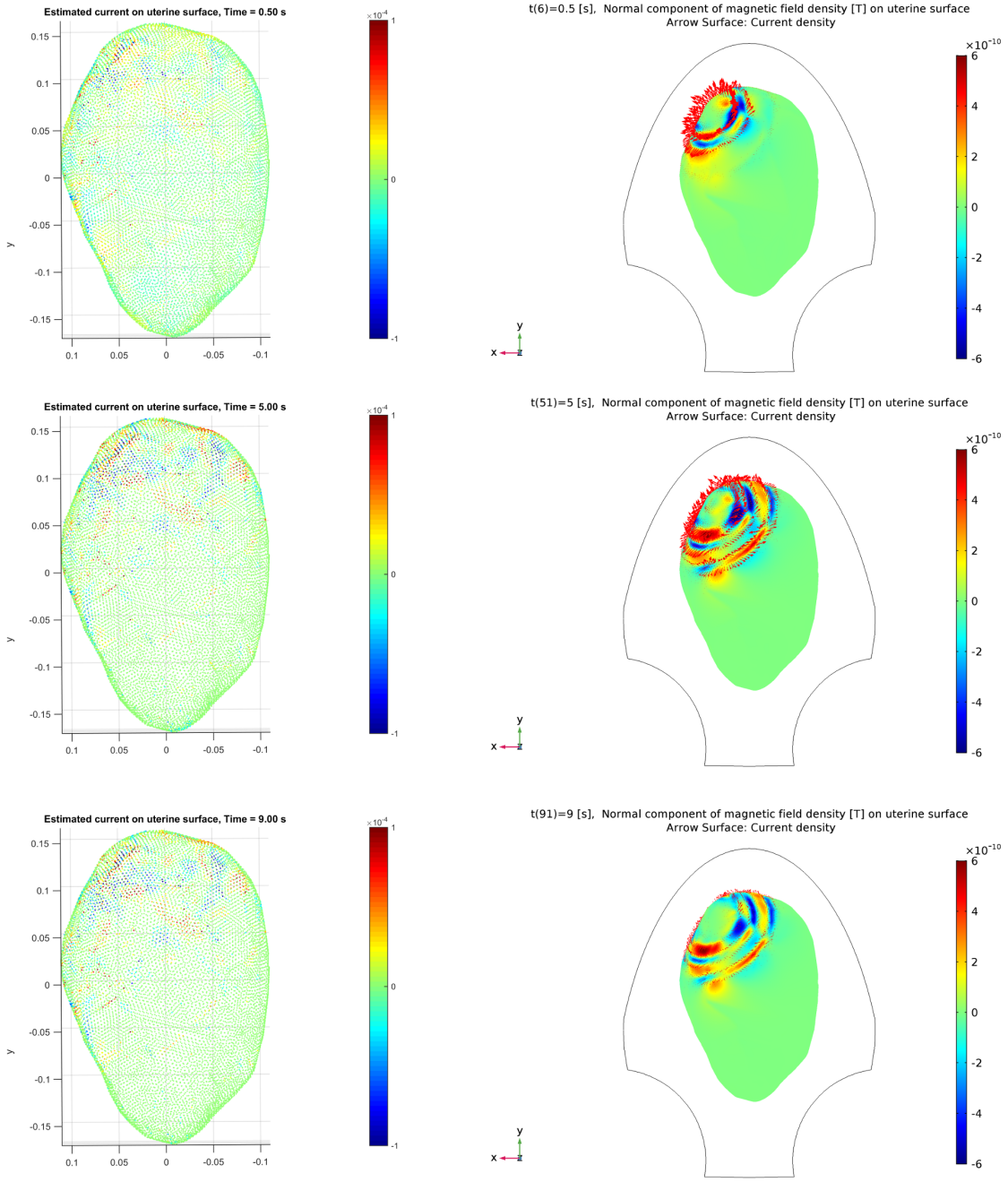

(a) Estimated source current amplitudes

(b) Synthetic source current amplitudes generated by our multiscale model

Figure 3.12: Estimated and synthetic source current amplitudes at time instants $t = 0.5$ [s], 5.0 [s], 9.0 [s] for Data Set 2 in Table 3.1.

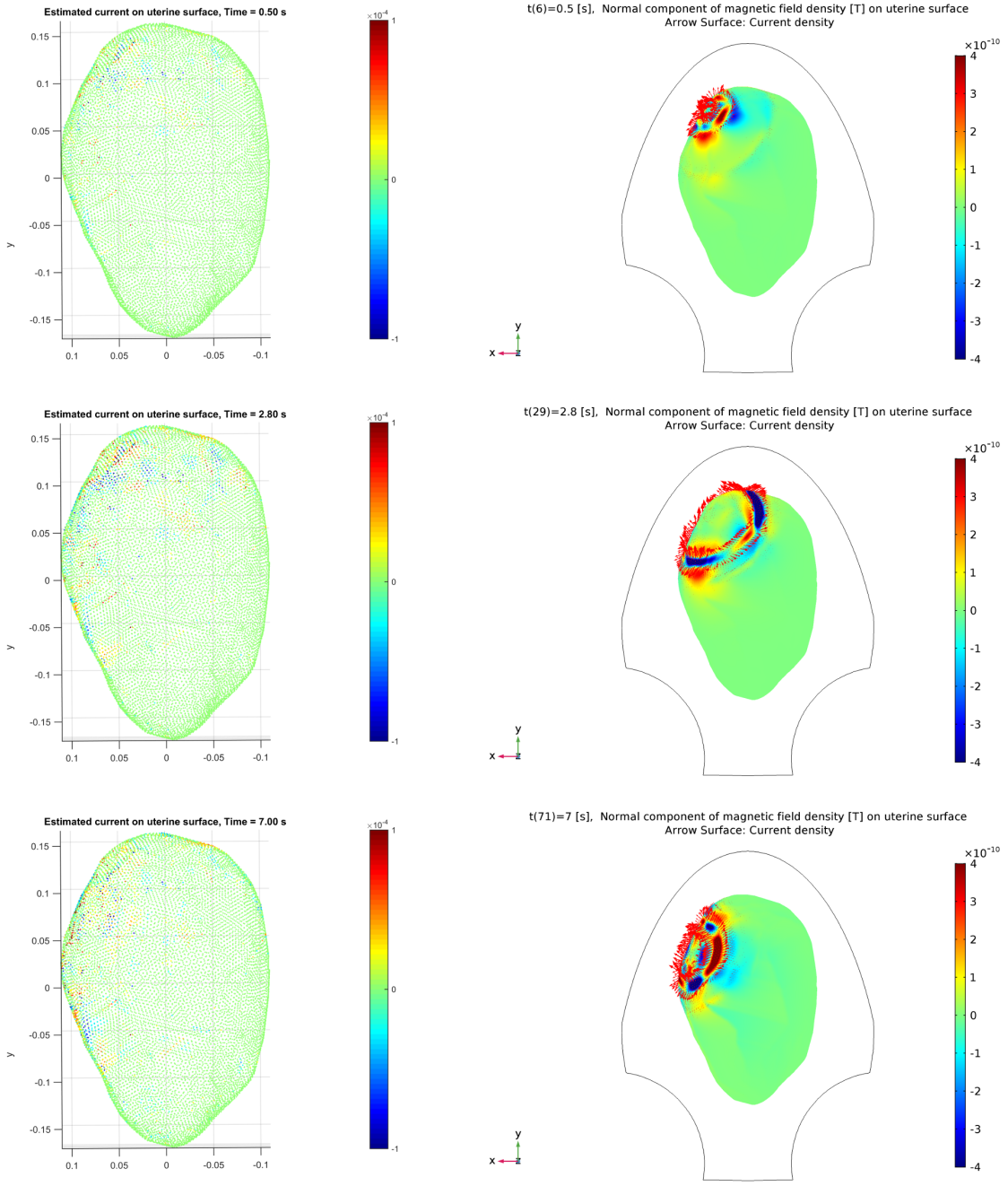

(a) Estimated source current amplitudes

(b) Synthetic source current amplitudes generated by our multiscale model

Figure 3.13: Estimated and synthetic source current amplitudes at time instants $t = 0.5$ [s], 2.8 [s], 7.0 [s] for Data Set 3 in Table 3.1.

Table 3.2: Details of three real MMG data sets.

Data set	Data	M	N	T
1	MMG & abdominal deflection	149	12,412	23,040
2	MMG	148	12,412	16,001
3	MMG	148	12,412	19,201

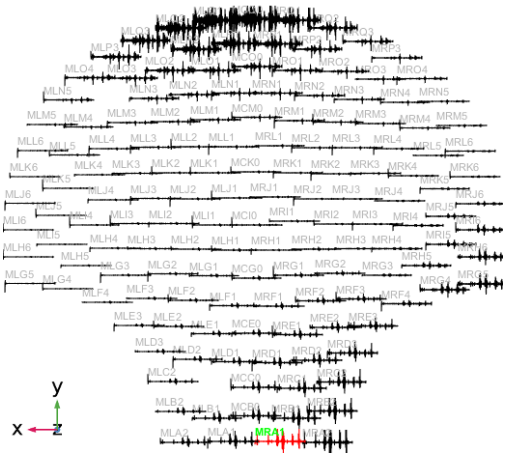

(a) Layout plot of MMG signals over SARA device

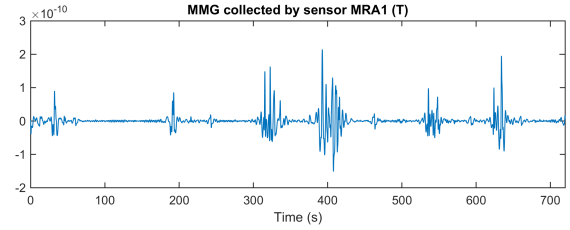

(b) Example MMG signal from Sensor MRA1 in the lower right side of the abdomen

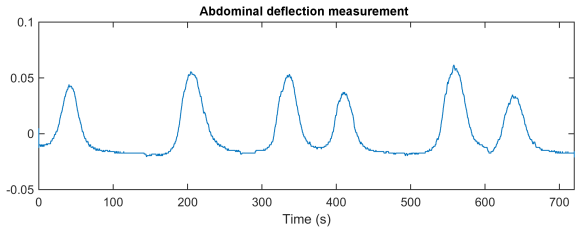

(c) Abdominal deflection

Figure 3.14: Preprocessed signals of Data set 1 in Table 3.2

MMG data $\boldsymbol{b}_t$, $t = 1, 2, \ldots, 23,040$ as 23,040 149-by-1 vectors and the lead-field matrix $\boldsymbol{G}$ as a 149-by-12,412 matrix, i.e., $M = 149$, $N = 12,412$, and $T = 23,040$ (see Data Set 1 in Table 3.2). The temporal courses of the MMG data over 149 sensors are shown in Fig. 3.17(a), with amplitude in Tesla (T). The MMG data collected when the woman experienced no contractions is at the level of several 10^{-13}s. Therefore, the regularization parameter λ was set to be 10^{-12}, slightly greater than the noise, in this estimation. The estimated MMG and source currents are shown in parts b and c of Fig. 3.17. As can be seen from Fig. 3.17, the source-current patterns match well with the real MMG data, i.e., there are stronger source

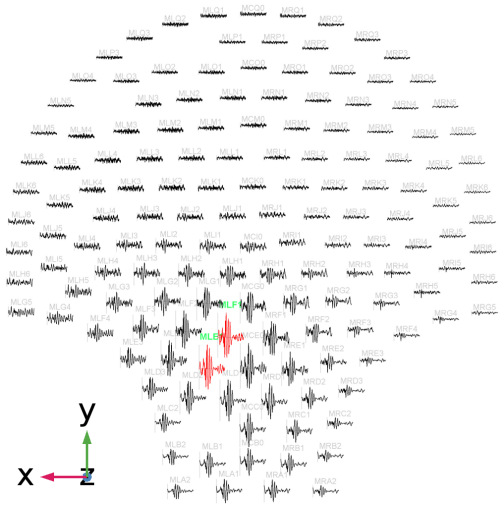

(a) Layout plot of MMG signals over SARA device that covers one contraction (430 s – 490 s)

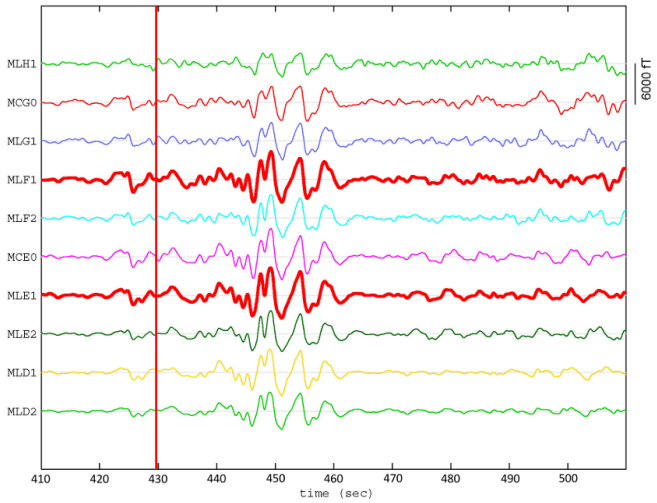

(b) Expanded view of MMG signals that were obtained from 10 sensors in the lower left side of the abdomen

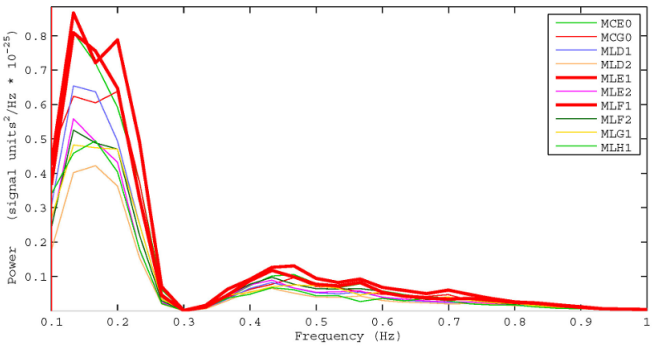

(c) Frequency spectrum obtained from these sensors

Figure 3.15: Preprocessed MMG signals of Data set 2 in Table 3.2

currents underlying more intense uterine electrical activities. In addition, we observe that the reconstructed MMG using our estimated source currents is in fair agreement with the real MMG data. Fig. 3.18 shows several snapshots of the real MMG data and corresponding estimated MMG and source current amplitudes. Fig. 3.18(a) illustrates the real MMG data on the abdominal surface, and Fig. 3.18(b) shows the reconstructed MMG data on the abdominal surface using the estimated source currents in the myometrium in Fig. 3.18(c). According to the non-invasive MMG recording on the abdominal surface, the cervix is active

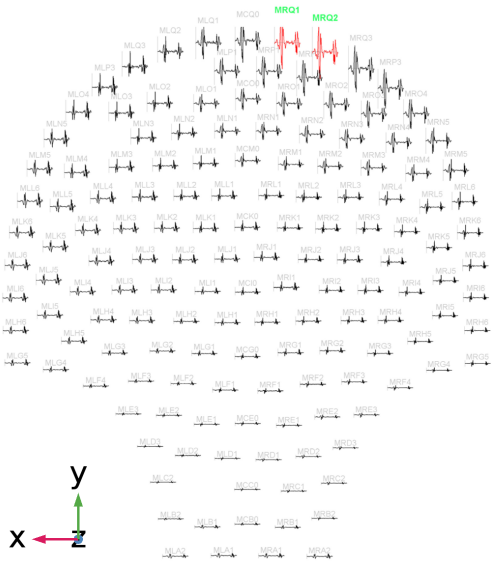

(a) Layout plot of MMG signals over SARA device that covers two contractions (580 s – 640 s)

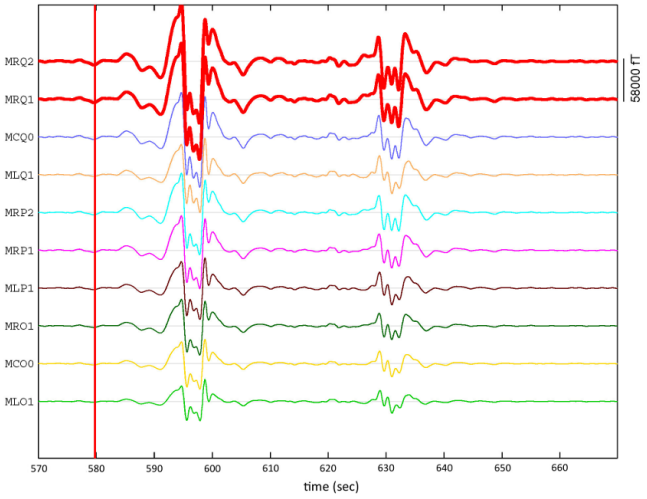

(b) Expanded view of MMG signals that were obtained from 10 sensors in the upper right side of the abdomen

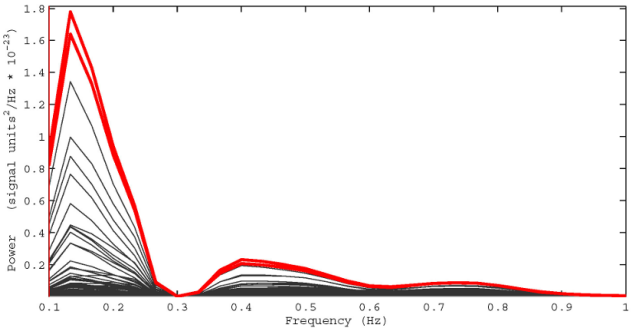

(c) Frequency spectrum obtained from these sensors

Figure 3.16: Preprocessed MMG signals of Data set 3 in Table 3.2

during this uterine contraction period, i.e., this contractile activity is constrained in the lower left region of the uterus (from the front perspective). The estimated source currents capture this local contraction: the source currents first arise in a small region in the lower left part of the uterus, then appear in larger regions when the contraction becomes stronger, and finally reverse this process.

For the other two data sets, we also removed the noisy sensors and the corresponding rows of the lead-field matrix before estimation (see Data Sets 2 and 3 in Table 3.2). In Figs. 3.19

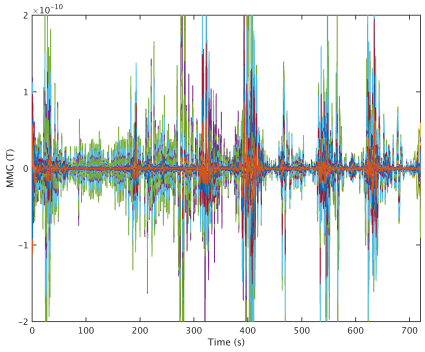

(a) Sensor temporal courses of real MMG data

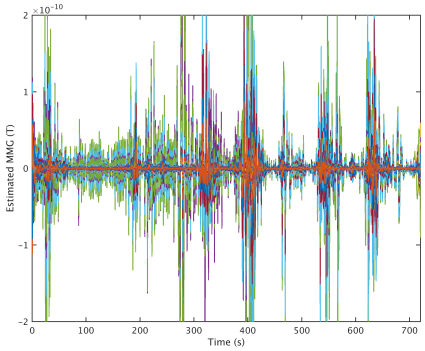

(b) Sensor temporal courses of the reconstructed MMG using our estimated source current

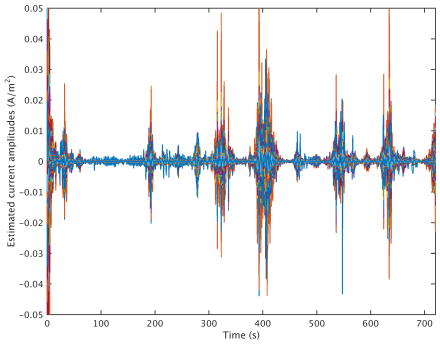

(c) Temporal courses of estimated source current amplitudes

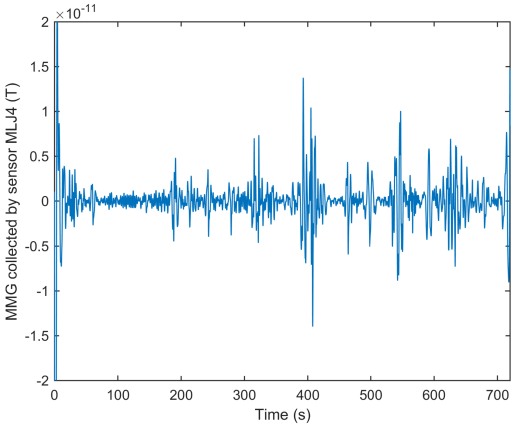

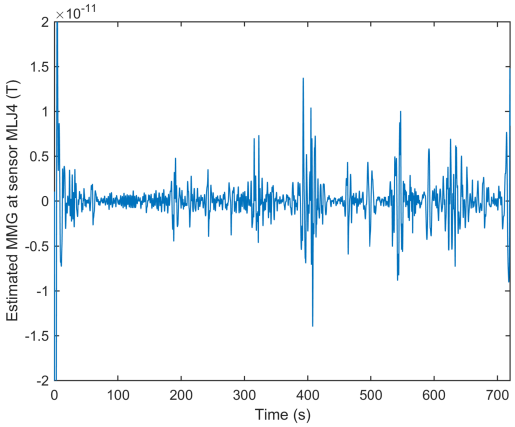

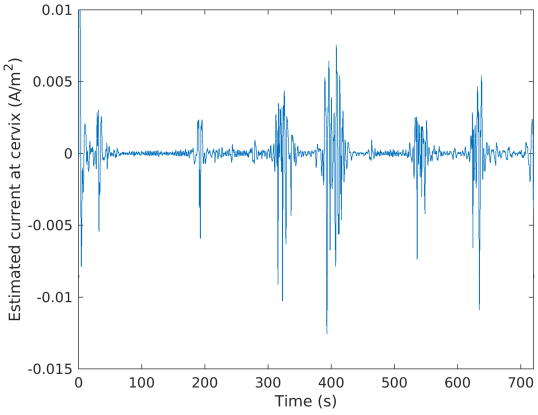

(d) Example traces of real MMG data, reconstructed MMG, and estimated source current amplitude, respectively

Figure 3.17: Sensor temporal courses of estimated source current amplitudes and the corresponding estimated MMG of Data Set 1 in Table 3.2.

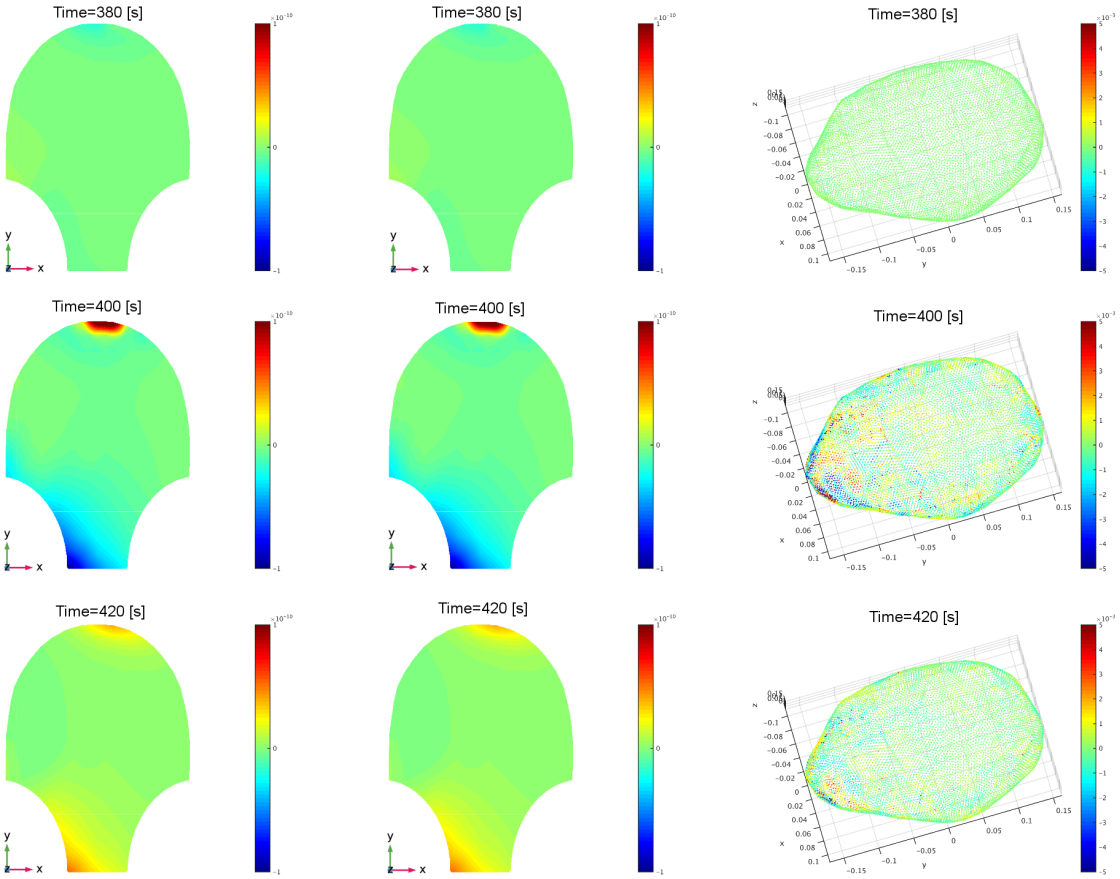

(a) Real MMG data on the abdominal surface collected by the SARA device

(b) Reconstructed MMG on the abdominal surface, using our estimated source currents

(c) Estimated source current amplitudes in the myometrium

Figure 3.18: Estimated source current amplitudes and the corresponding estimated MMG of Data Set 1 in Table 3.2 at time instants $t = 380$ [s], 400 [s], 420 [s].

and 3.20, we illustrate the temporal courses and snapshots of the two MMG data sets and the estimated source currents, respectively. We observe that the results are similar to those of the first data set, i.e., the estimated source current density matches well with the local contraction in the lower region and upper left region of the uterus, respectively.

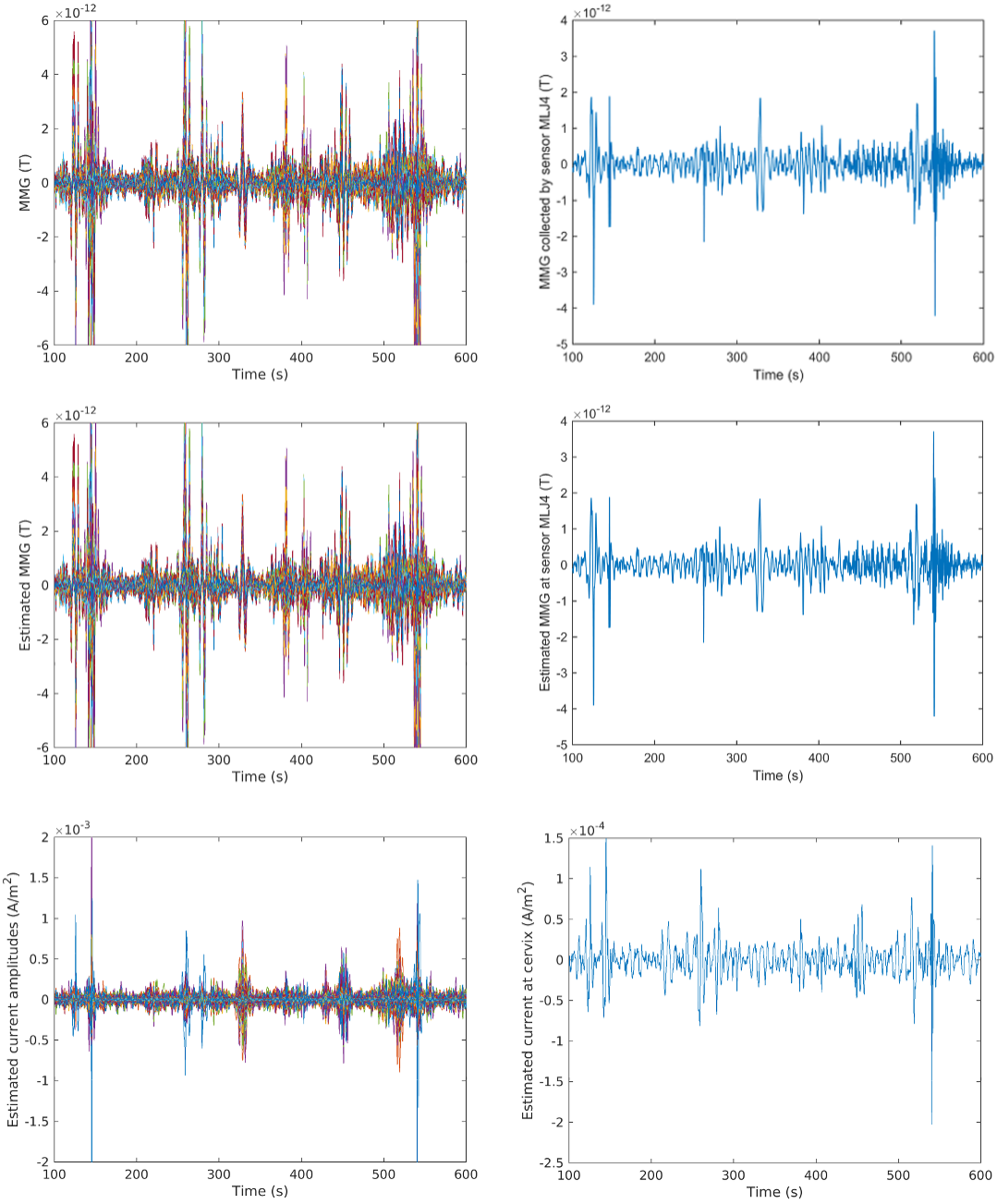

(a) Data Set 2

(b) Example traces for Data Set 2

Figure 3.19: Sensor temporal courses of estimated source current amplitudes and the corresponding estimated MMG for Data Sets 2 and 3 in Table 3.2.

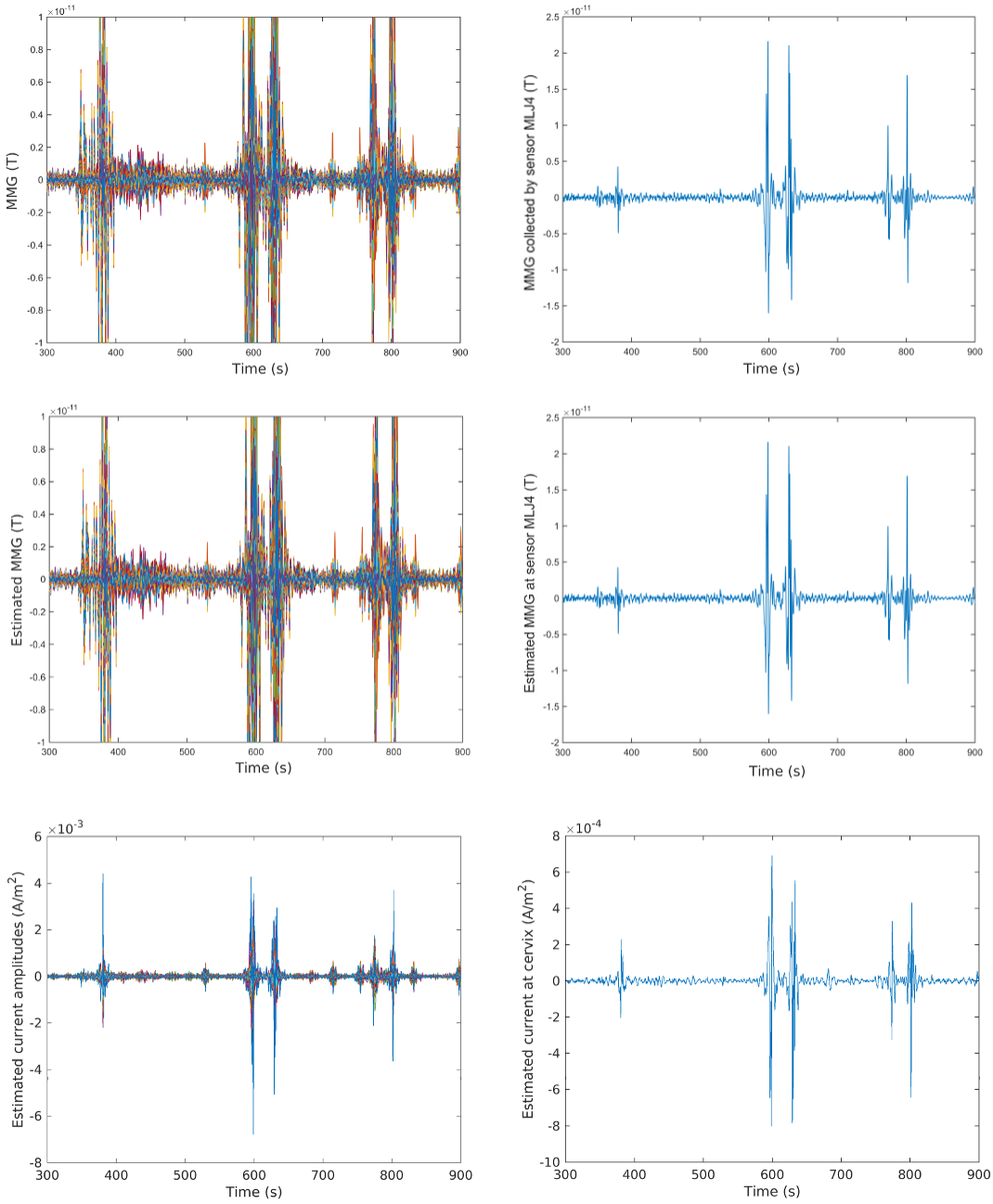

(c) Data Set 3

(d) Example traces for Data Set 3

Figure 3.19: Sensor temporal courses of estimated source current amplitudes and the corresponding estimated MMG for Data Sets 2 and 3 in Table 3.2 (cont.)

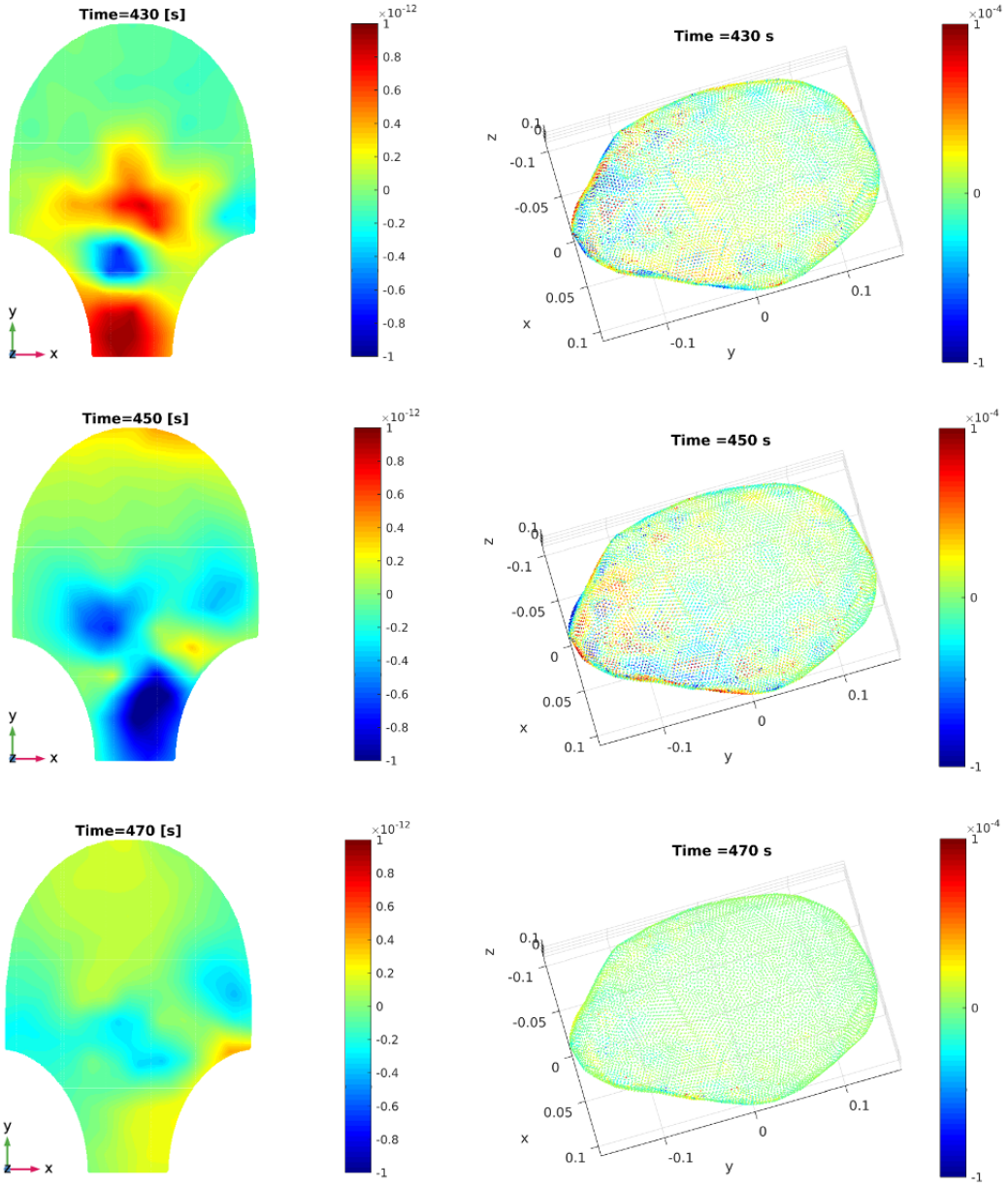

(a) Real MMG data for Data Set 2

(b) Estimated source current amplitudes in the myometrium for Data Set 2

Figure 3.20: Estimated source current amplitudes for Data Sets 2 and 3 in Table 3.2 at different time instants $t = 430$ [s], 450 [s], 470 [s] and $t = 377.75$ [s], 380.75 [s], 383.75 [s], respectively.

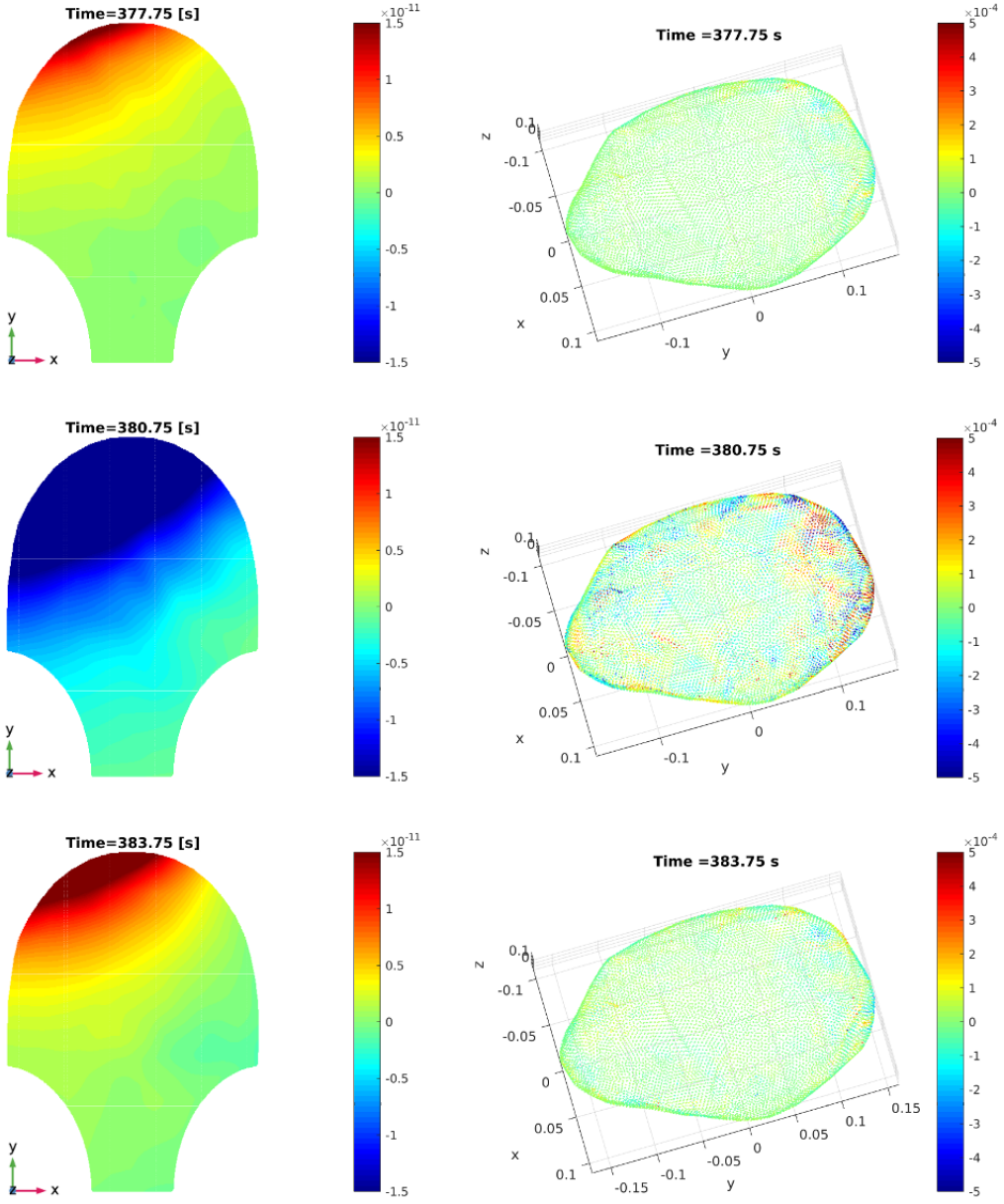

(c) Real MMG data for Data Set 3

(d) Estimated source current amplitudes in the myometrium for Data Set 3

Figure 3.20: Estimated source current amplitudes for Data Sets 2 and 3 in Table 3.2 at different time instants $t = 430$ [s], 450 [s], 470 [s] and $t = 377.75$ [s], 380.75 [s], 383.75 [s], respectively (cont.)

3.6.4 Intrauterine pressure prediction

Currently, TOCO or IUPC is widely used by physicians for assessing uterine contractions during pregnancy. To show the potential clinical implications of our source current estimation despite the lack of ground truth, we predicted intrauterine pressure for Data Set 1 in Table 3.2, which includes simultaneous measurement of abdominal deflection during a contraction as described earlier.

Fig. 3.21 shows the real abdominal deflection data in red and our predicted intrauterine pressure in blue. We observe that 83.33% of the predicted intrauterine pressure peaks display good predictive timing of uterine contractions when compared with the real abdominal deflection peaks. Note that the intrauterine pressure predicted from the myometrial source currents is several seconds in advance of the measured abdominal deflection, which is in agreement with the fact that the uterine electrical activities induce the increase of intrauterine pressure. According to the estimated source currents, there exist local contractile activities in uterus. Based on the mechanotransduction mechanism proposed in [35], a local contraction slightly increases the intrauterine pressure, resulting in a global wall tension increase and the induction of more local contractions that generate high intrauterine pressure. One possible reason for the difference of phase shifts between the real and predicted contractions is that the predicted contractions are calculated based on the local activities while the real ones are for the global change. The phase shift is dependent on the complex tissue recruitment and contraction coordination following the local contraction. The predicted contractile pressure curves for Data Sets 2 and 3 in Table 3.2 are also presented in Fig 3.22.

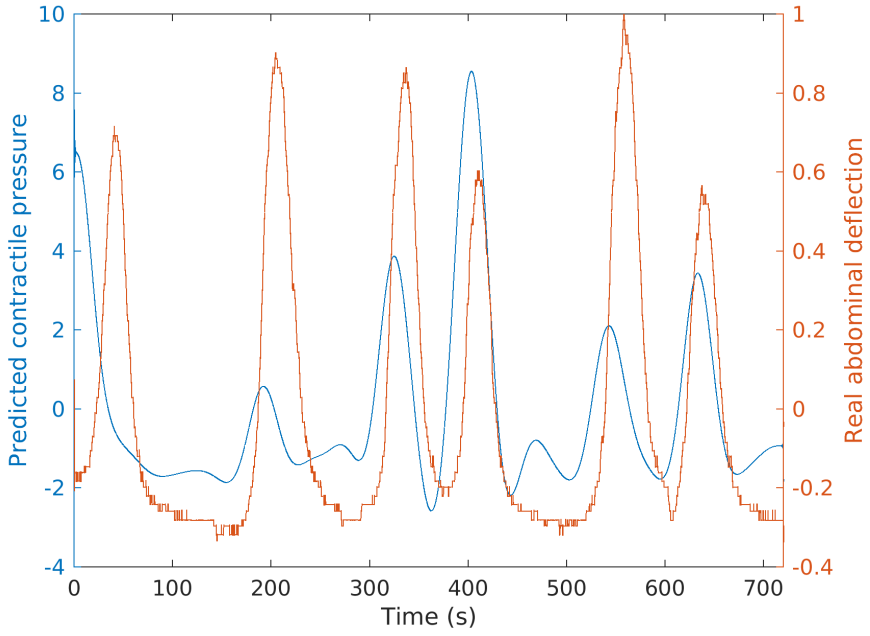

Figure 3.21: Real abdominal deflection observed during a contraction (red) and our predicted intrauterine pressure (blue) for Data Set 1 in Table 3.2.

3.7 Discussion

In this work, we tested our inverse estimation approach using synthetic MMG data sets which were generated using our previously developed multiscale model. The initiation areas were set at the fundus of the uterus (Fig. 3.8) and the resulting electrophysiological activity further recruits more area of the uterus in local contractions (Figs. 3.11-3.12). In real high-resolution recordings, there exist complex wave-propagation patterns, such as three or more wavefronts emerging at different positions of uterus and time instants and propagating in different directions [85]. According to our previous work [74], it is possible to obtain various magnetic field patterns by changing the model configuration, such as initiation location, initiation time, and fiber orientations, which will affect the emerging position, emerging time, and propagating direction of the waves. MMG measurement is independent of any

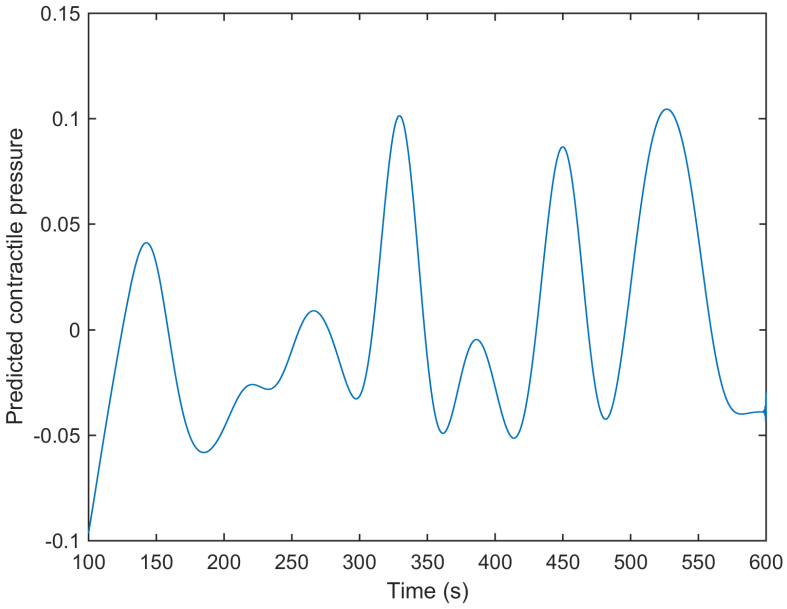

(a) Data Set 2

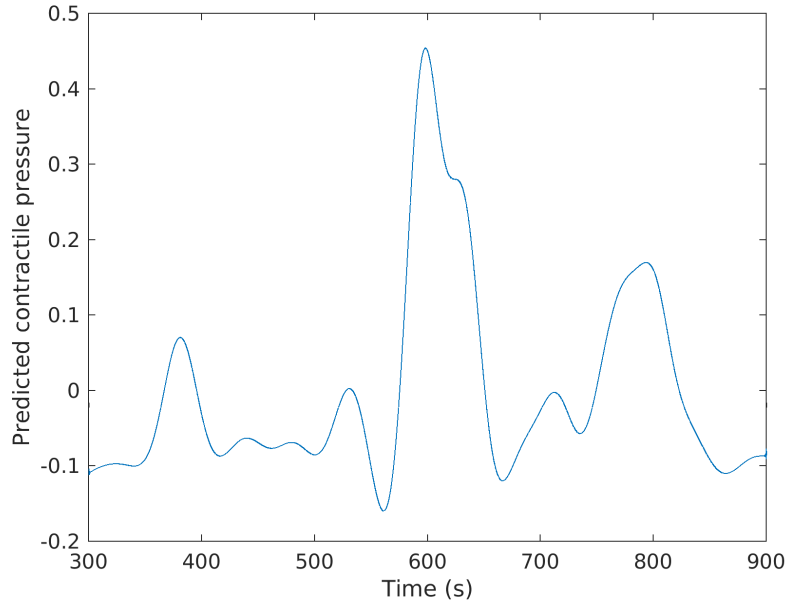

(b) Data Set 3

Figure 3.22: Predicted intrauterine pressure for Data Sets 2 and 3 in Table 3.2.

kind of reference, thus ensuring that the SARA device measures localized activity. The magnetic sensors of the SARA device are spaced 3 cm apart. Activities at different positions should be differentiable if the distance between them is greater than the distance between neighboring sensors. Our estimation result in Fig. 3.13 reflects the shift of excited areas in uterus during one local contraction.

In our multiscale model, the coordination of uterine contractions is through the continuous propagation of action potential in smooth muscle cells. However, animal and human data indicates that action potentials propagate noncontiguously and over short distances [23,33,34]. During the local contractions in real MMG data, we observe that the estimated source currents arise not only continuously, but also in areas that are not the neighbor of initiation area (Figs. 3.18 and 3.20). One possible explanation for this is the mechanotransduction for long-distance signaling mechanism presented in [35]. Particularly in the mechanotransduction mechanism, one local contraction increases intrauterine pressure, then increases wall tension, and induces more local contractions to generate strong uterine contractile activity.

Uterine activities are generated by myometrial source currents [34]. It is common to model these currents using current dipoles [86]. According to the superposition principle, all complex sources can be approximated by multiple current dipoles. In this work, we are interested in the distribution of source currents and hence assume for simplicity that the current dipoles are perpendicular to the surface of the myometrium. Our numerical results (Figs. 3.11-3.13, 3.18 and 3.20) show that the distribution of the source current estimation over the myometrium is in agreement with the synthetic source current and the MMG pattern measured using the SARA device, respectively. The snapshots of estimation results for synthetic MMG data (Figs. 3.11-3.13) illustrate that our approach can track the emergence of local activity

and the recruitment of larger area of source currents, although we do not consider the tangential component. Furthermore, the contractile force assessment based on the estimated source currents for real MMG data (Fig. 3.21) proves that the inverse solution characterizes the timing of the contraction process as measured by the uterine shape change. Estimating the directions of source currents can be accommodated using the same framework. In this case, the inverse solution would be the amplitudes of the source currents in three orthogonal directions at each vertex, calculated using the lead-field matrix, in which each column corresponds to the lead field generated by a unit current dipole pointed in each direction.

Regarding the volume conductor, a set of concentric spheres with homogeneous and isotropic conductivities is the simplest model, in which case the radial component of magnetic field has a closed form with respect to a tangential current dipole [41, 79]. A variant on the spherical model introduced in our previous work [60] is a set of spheres with the outer uterine layer shifted to the front of the abdomen. In [87], a more complex volume conductor represented by differently shaped ellipsoids is developed, which was constructed based on anatomic diagrams from Hunter's Anatomia Uteri Humani Gravidi [88]. In this project, we applied a more realistic volume conductor, proposed in our previous work [74], based on the MRI of a near-term woman and the abdomen that deforms to follow the SARA contour.

The spherical representation of the volume conductor geometry is a good approximation at the early stage of pregnancy, and its lead field can be expressed in a closed form. Our lead-field matrix, however, is constructed for a realistic geometry that is obtained after the acquisition of anatomical magnetic resonance images of a pregnant, near-term woman. In general, the computation of the lead field for this realistic geometry requires numerical solutions, for which we applied the finite element method, considering the anisotropic property of the myometrium. Numerical solution is computationally expensive and requires specifying

conductivity values for each compartment. The conductivity values of the intracellular and extracellular domains, unlike those of the abdomen, amniotic fluid, and fetus [89], have not been reported. In this work, these values were obtained from the effective myometrium conductivity calculated by applying Archie's law [90]. Regardless, construction of a lead-field matrix by using precise experimentally-confirmed conductivity values remains desirable.

The performance of the inverse calculation is sensitive to the regularization parameter λ. In general, the degree of the regularization should be consistent with the level of noise in the measurement data. Accordingly, the choice of λ is often determined by popular methods such as the discrepancy principle, χ^2 test, L-curve, and generalized cross validation [84]. In this work, a fixed value of λ, determined according to the noise, was used for the estimation. Although we did not choose an optimal value, λ was set to ensure that the signal to noise ratios (SNRs) of the MMG data sets were in a consistent range in order to mitigate their potential influence. We postulate that optimizing the regularization parameter will further improve the performance of our estimation, the next natural research topic.

Source estimation has wide application in many different anatomical domains, such as the brain, heart, and uterus [73,91–94]. The inverse problem is to estimate a large number of current dipoles from about one hundred measurements, which is mathematically ill-conditioned in the sense that various source configurations can produce the same magnetic field pattern. To solve it, it is necessary to impose additional constrains on the current dipoles. Among them, the most commonly used is the minimum-norm constraint, which imposes a weighted ℓ_2 norm on the source current distribution [79, 95–97]. A nonlinear smooth constraint is included using Bayesian methods [98], whose performance depends greatly on the choice of prior distributions. In spite of these methods, it is quite difficult to validate the estimation accuracy. However, our first attempt at source estimation for uterine contractions, despite

its limitations, is promising. Future research on developing a method to solve this inverse estimation is needed to achieve good estimation performance.

3.8 Summary

We proposed a method to estimate the underlying source currents in the myometrium from non-invasive abdominal MMG measurements of uterine contractile activities during pregnancy. Our method incorporates electrophysiological and anatomical knowledge of uterine contractions. We developed a forward model to describe the relationship between the abdominal magnetic field and myometrial source currents based on a lead-field matrix, and we used this model to compute the unknown source currents in the myometrium. We introduced a realistic four-compartment geometry as the volume conductor model and a current dipole as the source model. We also applied the finite element method to construct the lead-field matrix. We obtained the estimation of underlying source currents in the myometrium by solving a constrained optimization problem. Using an absolute-value-based method, we also predicted the intrauterine pressure, which is clinically used for uterine contraction measurements, from the estimated source currents. Finally, we displayed the lead fields that are generated by unit current dipoles at particular locations and illustrated our approach through numerical examples, using both synthetic and real MMG data. We then estimated the source currents and predicted the intrauterine pressure to show its clinical implications. Our work is potentially important as a starting point for characterizing underlying activities of uterine contractions during pregnancy, and potentially for diagnosing contractile dysfunctions.

Chapter 4

Conclusions and Future Work

In this chapter, we summarize the key contributions of this work in Section 4.1 and discuss the future work in Section 4.2.

4.1 Summary and conclusions

In this dissertation, based on MMG measurements, we studied the forward electromagnetic modeling and inverse estimation of uterine contractions during pregnancy.

We proposed a realistic multiscale forward electromagnetic model of human uterine contractions during pregnancy. Our approach aimed at computing the abdominal magnetic field that is generated by uterine activities, taking into account current electrophysiological and anatomical knowledge of the uterus jointly at the cellular, tissue, and organ levels. We applied a generalized version of the FitzHugh-Nagumo equations to each uterine smooth muscle cell and investigated its parameter values using bifurcation analysis to model both plateau-type and bursting-type action potentials. The simplicity and flexibility of this model for capturing action potential characteristics make it a good candidate for the cellular model,

although it does not consider detailed ionic dynamics such as those of Ca^{2+}, K^+, and Na^+. For the myometrium, considering the anisotropic property of tissue fibers, we designed a random conductivity tensor model that is applicable to arbitrary uterine shapes. We divided the entire uterus wall into 25 contiguous regions and assigned a random fiber orientation to each region. We also derived analytical expressions for the propagation speed and spiking frequency of the bursting potential. At the organ level, we introduced a realistic four-compartment volume conductor, including the fetus, amniotic fluid, uterus, and abdomen, based on the MRI of a near-term woman. We also proposed a sensor array model to represent the sensing directions of the SARA device that is used to take MMG measurements. We illustrated our analysis of the cellular model parameters through a numerical example with a periodic Heaviside stimulus current. The resulting resting potential is -55.5 mV and the period of consecutive contractions is about 420 s, which closely approximate the real human recordings. With numerical examples, we tested the sensitivity of MMG outputs to our model configuration aspects, such as volume conductor shape, fiber orientation, and initiation location and demonstrated that the last two are the main factors that affect the MMG pattern. We also showed that tuning the parameters of our multiscale forward model enables it to capture local uterine contractile activity that is observed in real MMG data.

To investigate inner uterine activity from external non-invasive recordings based on the model we developed, we then developed a general analysis for the inverse problem involved in uterine contractions during pregnancy. Our aim was to estimate the underlying source currents that result in the abdominal MMG measurements. We applied distributed current dipoles as the source model embedded in the previously developed realistic volume conductor. We constructed a lead-field matrix based on the quasi-static Maxwell's equations, using the finite element method to relate the sensor-oriented magnetic field to the unit current dipoles. Based on this lead-filed matrix, we developed a linear approximation model representing the

relationship between the abdominal MMG measurements and the amplitudes of the current dipoles. To solve the non-uniqueness issue, we conducted the estimation by solving a constrained least-squares problem, focusing on the main source currents. Based on the estimated source currents, we predicted the contractile pressure using an absolute-value-based method to show the clinical implications of our work. We presented the lead-field matrix by displaying the lead fields corresponding to unit current dipoles in different areas of the myometrium, including the fundus and cervix, and the left, right, front, and back sides. We illustrated our approach through numerical examples with both synthetic MMG data, which were generated using our multiscale forward model, and real MMG data, which were collected using the SARA device. Considering the random initiation area and the short-distance propagation of the action potential, we assumed the initiation to be located at the fundus of the uterus and set the parameters of our multiscale model to generate limited-propagation plateau-type and bursting-type action potentials according to our previous bifurcation analysis. We showed that our approach captures the local initiation, the further short-distance recruitment, and the change of active areas of contractile activity during pregnancy. We also observed that the predicted contractile pressure matches with the real uterine shape change with respect to the timing of contractions. This should allow us to detect labor from external non-invasive measurements, which is particularly important in the diagnosis and treatment of preterm and post-term births.

4.2 Future directions

In this section, we discuss potential future research directions.

Ionic current model: In this dissertation, we applied the FitzHugh-Nagumo equations as the ionic current model at the cellular level in the multiscale forward model. Although this model can capture the characteristics of action potential response, it includes no detailed information about the dynamics of ions that are functionally important in uterine activity, in particular Ca^{2+}, Na^{+}, and K^{+}. The action potential of myocytes is attributed to the entry of Ca^{2+} through voltage-sensitive Ca^{2+} channels, and possibly also through fast Na^{+} channels close to the end of the pregnancy. The differences in excitability between pregnant and non-pregnant myometria are influenced by changes in K^{+} conductance, such as a decrease in the BKCa channel conductance and an increase in conductance through delayed rectifier channels. Therefore, developing an ionic current model that includes the detailed ion dynamics would make the multiscale model more realistic.

Anisotropy of myometrium: We have identified that the anisotropic property of the myometrium greatly affects the magnetic field pattern of uterine contractions. However, there is no widely accepted global model of the fiber architecture of the myometrium. Some local structures exist according to the MRI DTI images of pregnant women. It would be helpful to incorporate realistic fiber structures to make the multiscale model more accurate.

Mechanical force model: In the multiscale forward modeling work, we focused on the electrophysiological and anatomical aspects of uterine contractions, but not the mechanical aspect. A mechanical contraction is a result of shortening of the myometrial cells following their excitation. It appears in the form of a force generation and an intrauterine pressure increase. The force generation in the myometrial smooth muscle cells is controlled by the intracellular Ca^{2+} concentration, which is highly related to the Ca^{2+} channels. It would be interesting to develop a mechanical force model to describe the force generation, allowing further validation of our multiscale model with real measurements.

Source current direction: In the inverse problem work, we assumed that the current dipoles were perpendicular to the myometrium surface. Although the inverse solution can capture the characteristics of the local contractions during pregnancy, it would be interesting to estimate the directions of the current dipoles, for which it is promising to apply the same inverse estimation framework. In this case, the direction can be represented as three orthogonal components, and each column of the lead-field matrix would correspond to the lead field generated by a unit current dipole in each component. The inverse solution would be the amplitudes of the current dipoles in each component at the source locations. This approach would help to investigate the propagation direction of source currents during the contractions at term.

Regularization parameter: In this work, we chose a fixed value for the regularization parameter in solving the optimization problem. This parameter plays a critical role in balancing the estimation error and sparse penalty. Therefore, obtaining an optimal value for this regularization parameter would provide a more accurate estimation of the contractile source currents.

Inverse estimation method: Estimating the amplitudes of a large number of current dipoles from hundreds of measurements is mathematically ill-posed. In this dissertation, we imposed an ℓ_1-norm constraint on the amplitudes, focusing on the most significant source currents that contributed to uterine contractions. It would be interesting to develop an estimation method in order to achieve better performance.

Initiation localization: In this work, we found that the magnetic field measurements of uterine activity can be greatly affected by the location of the initiation area. The myometrial smooth muscle cells can function as pacemakers to spontaneously excite electric activity. However, it is still uncertain whether a pacemaker mechanism exists in the uterus or not. In clinical

experiments, uterine activities are observed to be initiated at any site of the myometrium, and the initiation area can vary during subsequent contractions or even in a single contraction. It would be illustrative to localize the initiation area to help determine the existence of pacemaker cells in the uterus.

Prediction of labor: It would be interesting to predict labor based on the estimated internal uterine source currents together with the external measurements. This prediction is extremely important in the timing of labor, which can help physicians to diagnose uterine dysfunction associated with preterm or post-term bith and provide timely treatment.

Bibliography

[1] Segen JC. Concise Dictionary of Modern Medicine. McGraw-Hill; 2006. Available from: https://books.google.com/books?id=vVNqAAAAMAAJ.

[2] McCormick MC, Litt JS, Smith VC, Zupancic JAF. Prematurity: an overview and public health implications. Annual Review of Public Health. 2011;32:367–379.

[3] Gulmezoglu AM, Crowther CA, Middleton P, Heatley E. Induction of labour for improving birth outcomes for women at or beyond term. The Cochrane Database of Systematic Reviews. 2012 Jun;(6):CD004945.

[4] El Marroun H, Zeegers M, Steegers EAP, van der Ende J, Schenk JJ, Hofman A, et al. Post-term birth and the risk of behavioural and emotional problems in early childhood. International Journal of Epidemiology. 2012 Jun;41(3):773–781.

[5] Clark SL, Simpson KR, Knox GE, Garite TJ. Oxytocin: new perspectives on an old drug. American Journal of Obstetrics and Gynecology. 2009 Jan;200(1):35.e1–6.

[6] Vogel JP, Nardin JM, Dowswell T, West HM, Oladapo OT. Combination of tocolytic agents for inhibiting preterm labour. The Cochrane Database of Systematic Reviews. 2014 Jul;(7):CD006169.

[7] Hayes EJ, Weinstein L. Improving patient safety and uniformity of care by a standardized regimen for the use of oxytocin. American Journal of Obstetrics & Gynecology. 2017 Aug;198(6):622.e1–622.e7. Available from: http://dx.doi.org/10.1016/j.ajog.2008.01.039.

[8] Chard T, Grudzinskas JG. The Uterus. Cambridge Reviews in Human Reproduction. Cambridge University Press; 1994. Available from: https://books.google.com/books?id=2gBrQbeylBkC.

[9] Young RC, Hession RO. Three-dimensional structure of the smooth muscle in the term-pregnant human uterus. Obstetrics and Gynecology. 1999 Jan;93(1):94–99.

[10] Wagner H. The structure of the human uterine musculature, and fibre displacement during contraction. Archiv fur Gynakologie. 1950;179(1):105–114.

[11] Jaisle F. Structure and function of the myometrium. 1. A short review of the anatomy, biochemistry and electrophysiology of the uterus musulature. Die Medizinische Welt. 1964 Sep;39:2076–81 CONTD.

[12] Schwalm H, Dubrauszky V. The structure of the musculature of the human uterus-muscles and connective tissue. American Journal of Obstetrics & Gynecology. 1966 Apr;94(3):391–404. Available from: http://dx.doi.org/10.1016/0002-9378(66)90661-2.

[13] Weiss S, Jaermann T, Schmid P, Staempfli P, Boesiger P, Niederer P, et al. Three-dimensional fiber architecture of the nonpregnant human uterus determined ex vivo using magnetic resonance diffusion tensor imaging. The Anatomical Record Part A: Discoveries in Molecular, Cellular, and Evolutionary Biology. 2006;288A(1):84–90. Available from: http://dx.doi.org/10.1002/ar.a.20274.

[14] Young RC. Myocytes, myometrium, and uterine contractions. Annals of the New York Academy of Sciences. 2007;1101. Available from: http://dx.doi.org/10.1196/annals.1389.038.

[15] Marshall JM. Regulation of activity in uterine smooth muscle. Physiological Reviews Supplement. 1962 Jul;5:213–227.

[16] Sanborn BM. Ion channels and the control of myometrial electrical activity. Seminars in Perinatology. 1995 Feb;19(1):31–40.

[17] Parkington HC, Tonta MA, Brennecke SP, Coleman HA. Contractile activity, membrane potential, and cytoplasmic calcium in human uterine smooth muscle in the third trimester of pregnancy and during labor. American Journal of Obstetrics and Gynecology. 1999 Dec;181(6):1445–1451.

[18] Lammers WJEP, Ver Donck L, Stephen B, Smets D, Schuurkes JAJ. Origin and propagation of the slow wave in the canine stomach: the outlines of a gastric conduction system. American Journal of Physiology Gastrointestinal and Liver Physiology. 2009 Jun;296(6):G1200–10.

[19] O'Grady G, Du P, Cheng LK, Egbuji JU, Lammers WJEP, Windsor JA, et al. Origin and propagation of human gastric slow-wave activity defined by high-resolution mapping. American Journal of Physiology Gastrointestinal and Liver Physiology. 2010 Sep;299(3):G585–92.

[20] Young RC. The uterine pacemaker of labor. Best Practice & Research Clinical Obstetrics & Gynaecology. 2018;Available from: http://www.sciencedirect.com/science/article/pii/S1521693418300786.

[21] Lammers WJEP, Stephen B, Al-Sultan MA, Subramanya SB, Blanks AM. The location of pacemakers in the uteri of pregnant guinea pigs and rats. American Journal of Physiology Regulatory, Integrative and Comparative Physiology. 2015 Dec;309(11):R1439–46.

[22] Lammers WJ. The electrical activities of the uterus during pregnancy. Reproductive Sciences. 2013;20(2):182–189.

[23] Rabotti C, Mischi M. Propagation of electrical activity in uterine muscle during pregnancy: a review. Acta physiologica (Oxford, England). 2015 Feb;213(2):406–416.

[24] Sperelakis N, Inoue Y, Ohya Y. Fast Na+ channels and slow Ca2+ current in smooth muscle from pregnant rat uterus. Molecular and Cellular Biochemistry. 1992;114(1):79–89. Available from: http://dx.doi.org/10.1007/BF00240301.

[25] Khan RN, Smith SK, Morrison JJ, Ashford ML. Ca2+ dependence and pharmacology of large-conductance K+ channels in nonlabor and labor human uterine myocytes. The American Journal of Physiology. 1997 Nov;273(5 Pt 1):C1721–31.

[26] Garfield RE, Sims S, Daniel EE. Gap junctions: their presence and necessity in myometrium during parturition. Science (New York, NY). 1977 Dec;198(4320):958–960.

[27] Garfield RE, Sims SM, Kannan MS, Daniel EE. Possible role of gap junctions in activation of myometrium during parturition. The American Journal of Physiology. 1978 Nov;235(5):C168–79.

[28] Garfield RE, Hayashi RH. Appearance of gap junctions in the myometrium of women during labor. American Journal of Obstetrics and Gynecology. 1981 Jun;140(3):254–260.

[29] Garfield RE, Blennerhassett MG, Miller SM. Control of myometrial contractility: role and regulation of gap junctions. Oxford Reviews of Reproductive Biology. 1988;10:436–490.

[30] Miller SM, Garfield RE, Daniel EE. Improved propagation in myometrium associated with gap junctions during parturition. American Journal of Physiology-Cell Physiology. 1989;256(1):C130–C141.

[31] Miyoshi H, Boyle MB, MacKay LB, Garfield RE. Gap junction currents in cultured muscle cells from human myometrium. American Journal of Obstetrics and Gynecology. 1998;178(3):588–593. Available from: http://www.sciencedirect.com/science/article/pii/S0002937898704430.

[32] Smith R, Imtiaz M, Banney D, Paul JW, Young RC. Why the heart is like an orchestra and the uterus is like a soccer crowd. American Journal of Obstetrics and Gynecology. 2015 Aug;213(2):181–185.

[33] Lammers WJEP, Mirghani H, Stephen B, Dhanasekaran S, Wahab A, Al Sultan MaH, et al. Patterns of electrical propagation in the intact pregnant guinea pig uterus. American Journal of Physiology Regulatory, Integrative and Comparative Physiology. 2008 Mar;294(3):R919–28. Available from: http://www.ncbi.nlm.nih.gov/pubmed/18046017.

[34] Rabotti C, Mischi M, Beulen L, Oei G, Bergmans JWM. Modeling and identification of the electrohysterographic volume conductor by high-density electrodes. IEEE Transactions on Biomedical Engineering. 2010 Mar;57(3):519–527.

[35] Young RC. Mechanotransduction mechanisms for coordinating uterine contractions in human labor. Reproduction (Cambridge, England). 2016 Aug;152(2):R51–61.

[36] Smyth CN. The guard-ring tocodynamometer; absolute measurement of intra-amniotic pressure by a new instrument. The Journal of Obstetrics and Gynaecology of the British Empire. 1957 Feb;64(1):59–66.

[37] Devedeux D, Marque C, Mansour S, Germain G, Duchene J. Uterine electromyography: a critical review. American Journal of Obstetrics and Gynecology. 1993 Dec;169(6):1636–1653.

[38] Buhimschi C, Boyle MB, Saade GR, Garfield RE. Uterine activity during pregnancy and labor assessed by simultaneous recordings from the myometrium and abdominal surface in the rat. American Journal of Obstetrics and Gynecology. 1998 Apr;178(4):811–822. Available from: http://www.sciencedirect.com/science/article/pii/S0002937898704983.

[39] Marque C, Duchene J. Human abdominal EHG processing for uterine contraction monitoring. Biotechnology (Reading, Mass). 1989;11:187.

[40] Plonsey R. Magnetic field resulting from action currents on cylindrical fibres. Medical and Biological Engineering and Computing. 1981 May;19(3):311–315. Available from: https://doi.org/10.1007/BF02442550.

[41] Sarvas J. Basic mathematical and electromagnetic concepts of the biomagnetic inverse problem. Physics in Medicine and Biology. 1987 Jan;32(1):11–22.

[42] Vasak B, Graatsma EM, Hekman-Drost E, Eijkemans MJ, Schagen van Leeuwen JH, Visser GH, et al. Uterine electromyography for identification of first-stage labor arrest in term nulliparous women with spontaneous onset of labor. American Journal of Obstetrics & Gynecology. 2018 Apr;209(3):232.e1–232.e8. Available from: http://dx.doi.org/10.1016/j.ajog.2013.05.056.

[43] La Rosa PS, Nehorai A, Eswaran H, Lowery CL, Preissl H. Detection of uterine MMG contractions using a multiple change point estimator and the K-means cluster algorithm. IEEE Transactions on Bio-medical Engineering. 2008 Feb;55(2 Pt 1):453–467.

[44] Nagarajan R, Eswaran H, Wilson JD, Murphy P, Lowery C, Preissl H. Analysis of uterine contractions: a dynamical approach. The Journal of Maternal-Fetal & Neonatal Medicine. 2003 Jul;14(1):8–21.

[45] Ramon C, Preissl H, Murphy P, Wilson JD, Lowery C, Eswaran H. Synchronization analysis of the uterine magnetic activity during contractions; 2005.

[46] Garfield RE, Maner WL, MacKay LB, Schlembach D, Saade GR. Comparing uterine electromyography activity of antepartum patients versus term labor patients. American Journal of Obstetrics and Gynecology. 2005 Jul;193(1):23–29.

[47] Garfield RE, Maner WL. Physiology and Electrical Activity of Uterine Contractions. Seminars in Cell & Developmental Biology. 2007 Jun;18(3):289–295. Available from: http://www.ncbi.nlm.nih.gov/pmc/articles/PMC2048588/.

[48] Eswaran H, Preissl H, Wilson JD, Murphy P, Robinson SE, Lowery CL. First magnetomyographic recordings of uterine activity with spatial-temporal information with a 151-channel sensor array. American Journal of Obstetrics and Gynecology. 2002;187(1):145–151.

[49] Eswaran H, Preissl H, Wilson JD, Murphy P, Lowery CL. Prediction of labor in term and preterm pregnancies using non-invasive magnetomyographic recordings of uterine contractions. American Journal of Obstetrics and Gynecology. 2004;190(6):1598–1602.

[50] Andersen HF, Barclay ML. A computer model of uterine contractions based on discrete contractile elements. Obstetrics and Gynecology. 1995 Jul;86(1):108–111.

[51] Young RC. A computer model of uterine contractions based on action potential propagation and intercellular calcium waves. Obstetrics and Gynecology. 1997 Apr;89(4):604–608.

[52] Garfield RE. Control of myometrial function in preterm versus term labor. Clinical Obstetrics and Gynecology. 1984;27(3):572–591.

[53] Luo CH, Rudy Y. A dynamic model of the cardiac ventricular action potential. I. Simulations of ionic currents and concentration changes. Circulation Research. 1994 Jun;74(6):1071–1096.

[54] Bursztyn L, Eytan O, Jaffa AJ, Elad D. Mathematical model of excitation-contraction in a uterine smooth muscle cell. American Journal of Physiology Cell Physiology. 2007 May;292(5):1816–1829.

[55] Rihana S, Terrien J, Germain G, Marque C. Mathematical modeling of electrical activity of uterine muscle cells. Medical & Biological Rngineering & Bomputing. 2009 Jun;47(6):665–675.

[56] Tong WC, Choi CY, Kharche S, Karche S, Holden AV, Zhang H, et al. A computational model of the ionic currents, Ca2+ dynamics and action potentials underlying contraction of isolated uterine smooth muscle. PloS One. 2011 Jan;6(4):18685–18705.

[57] Tong WC, Tribe RM, Smith R, Taggart MJ. Computational modeling reveals key contributions of KCNQ and hERG currents to the malleability of uterine action potentials underpinning labor. PLoS One. 2014;9(12).

[58] Laforet J, Rabotti C, Terrien J, Mischi M, Marque C. Toward a multiscale model of the uterine electrical activity. IEEE Transactions on Biomedical Engineering. 2011;58(12):3487–3490.

[59] Laforet J, Rabotti C, Mischi M, Marque C. Improved multi-scale modeling of uterine electrical activity. Innovation and Research in BioMedical Engineering. 2013;34(1):38–42.

[60] La Rosa PS, Eswaran H, Preissl H, Nehorai A. Multiscale forward electromagnetic model of uterine contractions during pregnancy. BMC Medical Physics. 2012;12(4).

[61] Govindan RB, Siegel E, Mckelvey S, Murphy P, Lowery CL, Eswaran H. Tracking the changes in synchrony of the electrophysiological activity as the uterus approaches labor using magnetomyographic technique. Reproductive Sciences. 2015;22(5):595–601.

[62] Fitzhugh R. Impulses and physiological states in theoretical models of nerve membrane. Biophysical Journal. 1961;1(1948):445–466.

[63] Nagumo J, Arimoto S, Yoshizawa S. An active pulse transmission line simulating nerve axon. Proceedings of the IRE. 1962;50(10):2061–2070.

[64] Wikland M, Lindblom B. Relationship between electrical and mechanical activity of the isolated term-pregnant human myometrium. European Journal of Obstetrics & Gynecology and Reproductive Biology. 1985 Dec;20(6):337–346.

[65] Murray JD. Mathematical Biology: I. An Introduction. 3rd ed. Interdisciplinary Applied Mathematics. Springer-Verlag New York, Inc.; 2002.

[66] Bibin L, Anquez J, de la Plata Alcalde JP, Boubekeur T, Angelini ED, Bloch I. Whole-body pregnant woman modeling by digital geometry processing with detailed uterofetal unit based on medical images. IEEE Transactions on Biomedical Engineering. 2010 Oct;57(10):2346–2358.

[67] Plonsey R, Heppner DB. Considerations of quasi-stationarity in electrophysiological systems. The Bulletin of Mathematical Biophysics. 1967 Dec;29(4):657–664.

[68] Malmivuo J, Plonsey R. Bioelectromagnetism: Principles and Applications of Bioelectric and Biomagnetic Fields. Oxford University Press; 1995. Available from: https://books.google.com/books?id=H9CFM0TqWwsC.

[69] Ermentrout B. Simulating, Analyzing, and Animating Dynamical Systems. Society for Industrial and Applied Mathematics; 2002.

[70] Young RC, Zhang P. Tissue-level bioelectrical signals as the trigger for uterine contractions in human pregnancy. Journal of the Society for Gynecologic Investigation. 2004 Oct;11(7):478–482.

[71] Young RC. Synchronization of regional contractions of human labor; direct effects of region size and tissue excitability. Journal of Biomechanics. 2015 Jun;48(9):1614–1619.

[72] Zahran S, Yochum M, Diab A, Zahran S, Marque C. Variation-based sparse source imaging in localizing uterine activity. In: 2017 39th Annual International Conference of the IEEE Engineering in Medicine and Biology Society (EMBC); 2017. p. 2948–2951.

[73] Lew S, Hämäläinen MS, Okada Y. Toward noninvasive monitoring of ongoing electrical activity of human uterus and fetal heart and brain. Clinical Neurophysiology. 2017 Oct;Available from: http://dx.doi.org/10.1016/j.clinph.2017.08.026.

[74] Zhang M, Tidwell V, La Rosa PS, Wilson JD, Eswaran H, Nehorai A. Modeling magnetomyograms of uterine contractions during pregnancy using a multiscale forward electromagnetic approach. PLOS ONE. 2016 Mar;11(3):1–23. Available from: http://dx.doi.org/10.1371%2Fjournal.pone.0152421.

[75] Alvarez CH, Reynolds SRM. A better understanding of uterine contractility through simultaneous recording with an internal and a seven channel external method. Surgery, Gynecology & Obstetrics. 1950 Dec;91(6):641–650.

[76] Fuchs AR. Uterine activity in late pregnancy and during parturition in the rat. Biology of Reproduction. 1969 Dec;1(4):344–353.

[77] Buhimschi CS. Spatiotemporal electromyography during human labor to monitor propagation of the uterine contraction wave and diagnose dystocia. American Journal of Obstetrics and Gynecology. 2009 Jan;200(1):1–3.

[78] Zienkiewicz OC, Taylor RL, Zhu JZ. The finite element method: its basis and fundamentals. Elsevier Science; 2005. Available from: https://books.google.com/books?id=YocoaH8lnx8C.

[79] Hämäläinen M, Hari R, Ilmoniemi RJ, Knuutila J, Lounasmaa OV. Magnetoencephalography¯theory, instrumentation, and applications to noninvasive studies of the working human brain. Reviews of Modern Physics. 1993 Apr;65:413–497. Available from: http://link.aps.org/doi/10.1103/RevModPhys.65.413.

[80] Uutela K, Hämäläinen M, Somersalo E. Visualization of magnetoencephalographic data using minimum current estimates. NeuroImage. 1999;10(2):173–180. Available from: http://www.sciencedirect.com/science/article/pii/S1053811999904548.

[81] Tibshirani R. Regression shrinkage and selection via the lasso. Journal of the Royal Statistical Society Series B (Methodological). 1996;58(1):267–288.

[82] Grant M, Boyd S. CVX: Matlab software for disciplined convex programming, version 2.1; 2014. http://cvxr.com/cvx.

[83] Skowronski MD, Harris JG, Marossero DE, Edwards RK, Euliano TY. Prediction of intrauterine pressure from electrohysterography using optimal linear filtering. IEEE Transactions on Biomedical Engineering. 2006 Oct;53(10):1983–1989.

[84] Hansen P. Rank-deficient and Discrete Ill-posed Problems. Society for Industrial and Applied Mathematics; 1998. Available from: http://epubs.siam.org/doi/abs/10.1137/1.9780898719697.

[85] Lammers WJ, Arafat K, El-Kays A, El-Sharkawy TY. Spatial and temporal variations in local spike propagation in the myometrium of the 17-day pregnant rat. The American Journal of Physiology. 1994 Nov;267(5 Pt 1):C1210–23.

[86] Williamson SJ, Kaufman L. Biomagnetism. Journal of Magnetism and Magnetic Materials. 1981;22(2):129–201.

[87] Barclay M, Andersen H, Simon C. Emergent behaviors in a deterministic model of the human uterus. Reproductive Sciences. 2010;17(10):948–954. Available from: http://dx.doi.org/10.1177/1933719110376544.

[88] Hunter W. Anatomia uteri humani gravidi tabulis illustrate (The anatomy of the human gravid uterus exhibited in figures). Birmingham: John Baskerville; 1774. Available from: https://collections.nlm.nih.gov/catalog/nlm:nlmuid-2491060R-bk.

[89] Peters MJ, Stinstra JG, Uzunbajakau S, Srinivasan N. In: Lin JC, editor. Fetal magnetocardiography. Boston, MA: Springer US; 2005. p. 1–40. Available from: http://dx.doi.org/10.1007/0-387-24024-1_1.

[90] Peters MJ, Stinstra G, Hendriks M. Estimation of the electrical conductivity of human tissue. Electromagnetics. 2001;21(7-8):545–557. Available from: http://dx.doi.org/10.1080/027263401752246199.

[91] Ahlfors SP, Ilmoniemi RJ, Hämäläinen MS. Estimates of visually evoked cortical currents. Electroencephalography and Clinical Neurophysiology. 1992;82(3):225–236. Available from: http://www.sciencedirect.com/science/article/pii/001346949290172E.

[92] Lai D, Liu C, Eggen MD, Iaizzo PA, He B. Cardiac source localization by means of a single moving dipole solution during endocardial pacing in an animal model. Conference proceedings : Annual International Conference of the IEEE Engineering in Medicine and Biology Society IEEE Engineering in Medicine and Biology Society Annual Conference. 2009;2009:1778–1780.

[93] Jeremic A, Nehorai A. Estimating current density in the heart using structured and unstructured covariance analysis. In: Proceedings of the 25th Annual International Conference of the IEEE Engineering in Medicine and Biology Society. vol. 3; 2003. p. 2335–2338.

[94] Yetik IS, Nehorai A, Lewine JD, Muravchik CH. Distinguishing between moving and stationary sources using EEG/MEG measurements with an application to epilepsy. IEEE Transactions on Biomedical Engineering. 2005 Mar;52(3):471–479.

[95] Wang JZ, Williamson SJ, Kaufman L. Magnetic source images determined by a lead-field analysis: the unique minimum-norm least-squares estimation. IEEE Transactions on Biomedical Engineering. 1992 Jul;39(7):665–675.

[96] Hämäläinen MS, Ilmoniemi RJ. Interpreting magnetic fields of the brain: minimum norm estimates. Medical & Biological Engineering & Computing. 1994;32(1):35–42. Available from: http://dx.doi.org/10.1007/BF02512476.

[97] Hauk O. Keep it simple: a case for using classical minimum norm estimation in the analysis of EEG and MEG data. NeuroImage. 2004;21(4):1612–1621. Available from: http://www.sciencedirect.com/science/article/pii/S1053811903007845.

[98] Baillet S, Garnero L. A Bayesian approach to introducing anatomo-functional priors in the EEG/MEG inverse problem. IEEE Transactions on Biomedical Engineering. 1997 May;44(5):374–385.

[99] Hale JK, Buttanri H, Kocak H. Dynamics and Bifurcations. Texts in Applied Mathematics. Springer New York; 1996.

Appendix A

Bifurcation Analysis of the Generalized FitzHugh-Nagumo Model

The variation of the FitzHugh-Nagumo (FHN) equations is represented as

$$\frac{\partial v_{\mathrm{m}}}{\partial t} = \frac{1}{\varepsilon_1 c_{\mathrm{m}}}(k(v_{\mathrm{m}} - v_1)(v_2 - v_{\mathrm{m}})(v_{\mathrm{m}} - v_3) - w + \nu) \triangleq f_1(v_{\mathrm{m}}, w), \tag{A.1}$$

$$\frac{\partial w}{\partial t} = \varepsilon_2(\beta v_{\mathrm{m}} - \gamma w + \delta) \triangleq f_2(v_{\mathrm{m}}, w). \tag{A.2}$$

The nullclines of the FHN model are given by the following two equations

$$f_1(v_{\mathrm{m}}, w) = 0, \tag{A.3}$$

$$f_2(v_{\mathrm{m}}, w) = 0. \tag{A.4}$$

The v_{m}-nullcline is a cubic function of v_{m}, which is shown as

$$w = k(v_{\mathrm{m}} - v_1)(v_2 - v_{\mathrm{m}})(v_{\mathrm{m}} - v_3) + \nu, \tag{A.5}$$

and the w-nullcline is a straight line as follows:

$$w = \frac{\beta}{\gamma} v_{\mathrm{m}} + \frac{\delta}{\gamma}. \tag{A.6}$$

The equilibrium of the FHN system is the intersection of these two nullclines, which is defined as (v_{m}^*, w^*). The stimulus amplitude ν can then be denoted as a function of the equilibrium v_{m}^* with other parameters fixed:

$$\nu(v_{\mathrm{m}}^*) = -k(v_{\mathrm{m}}^* - v_1)(v_2 - v_{\mathrm{m}}^*)(v_{\mathrm{m}}^* - v_3) + (\beta v_{\mathrm{m}}^* + \delta)/\gamma. \tag{A.7}$$

We are interested in the case when there is always only one equilibrium in the FHN system whatever the stimulus amplitude ν, for which the slope of the w-nullcline should be greater than the maximal slope of the v_{m}-nullcline. The slope of the straight w-nullcline is $\frac{\beta}{\gamma}$, while the maximal slope of the v_{m}-nullcline is found at the point $v_{\mathrm{m}} = \frac{v_1 + v_2 + v_3}{3}$ and it is equal to $\frac{k(v_1 + v_2 + v_3)^2}{3} - k(v_1 v_2 + v_1 v_3 + v_2 v_3)$. The condition for the existence and uniqueness of equilibrium is therefore given by:

$$\Delta_1 \triangleq (v_1 + v_2 + v_3)^2 - 3(v_1 v_2 + v_1 v_3 + v_2 v_3) - \frac{3\beta}{k\gamma} < 0. \tag{A.8}$$

The local stability of the equilibrium is determined by linearization of the nonlinear FHN model at the equilibrium, which is given by

$$\frac{\partial}{\partial t}\boldsymbol{x} = \boldsymbol{D}\boldsymbol{x}, \tag{A.9}$$

where $\boldsymbol{x} = \begin{pmatrix} v_{\mathrm{m}} - v_{\mathrm{m}}^* \\ w - w^* \end{pmatrix}$, and $\boldsymbol{D}$ is the Jacobian matrix at the equilibrium (v_{m}^*, w^*), which is shown as follows:

$$\begin{aligned} \boldsymbol{D} &= \begin{pmatrix} \dfrac{\partial f_1(v_{\mathrm{m}}, w)}{\partial v_{\mathrm{m}}} & \dfrac{\partial f_1(v_{\mathrm{m}}, w)}{\partial w} \\ \dfrac{\partial f_2(v_{\mathrm{m}}, w)}{\partial v_{\mathrm{m}}} & \dfrac{\partial f_2(v_{\mathrm{m}}, w)}{\partial w} \end{pmatrix} \Bigg|_{(v_{\mathrm{m}}^*, w^*)} \triangleq \begin{pmatrix} f_{1v_{\mathrm{m}}} & f_{1w} \\ f_{2v_{\mathrm{m}}} & f_{2w} \end{pmatrix} \\ &= \begin{pmatrix} \dfrac{q(v_{\mathrm{m}}^*, v_1, v_2, v_3, k)}{\varepsilon_1 c_{\mathrm{m}}} & -\dfrac{1}{\varepsilon_1 c_{\mathrm{m}}} \\ \varepsilon_2 \beta & -\varepsilon_2 \gamma \end{pmatrix}, \end{aligned} \tag{A.10}$$

where $q(v_{\mathrm{m}}^*, v_1, v_2, v_3, k) = -3kv_{\mathrm{m}}^{*2} + 2k(v_1 + v_2 + v_3)v_{\mathrm{m}}^* - k(v_1v_2 + v_1v_3 + v_2v_3)$. The solution of Eq. (A.9) can be represented as

$$\boldsymbol{x}(t) = \exp(\lambda t)\ \boldsymbol{v}, \tag{A.11}$$

where λ is the eigenvalue of the Jacobian matrix $\boldsymbol{D}$ and $\boldsymbol{v}$ is its corresponding eigenvector. By solving the characteristic equation

$$\det(\boldsymbol{D} - \lambda \boldsymbol{I}) = 0, \tag{A.12}$$

we obtain the relationship between eigenvalue λ and the equilibrium v_{m}^*, which is given as follows:

$$\lambda^2 - (f_{1v_{\mathrm{m}}} + f_{2w})\lambda + (f_{1v_{\mathrm{m}}} f_{2w} - f_{1w} f_{2v_{\mathrm{m}}}) = 0. \tag{A.13}$$

Depending on the values of eigenvalues, we can determine whether the equilibrium is stable or not. Since we are interested in characterizing the stability of equilibrium as a function of

model parameters, we need to compute eigenvalues as a function of these parameters and so we assess stability through the evaluation of two conditions as presented in Table A.1.

Table A.1: Conditions for the stability of equilibrium.

Type	Stability	Eigenvalues (λ_1 and λ_2)	Condition 1	Condition 2
saddle	unstable	$\lambda_1 > 0,\ \lambda_2 < 0$ or $\lambda_1 < 0,\ \lambda_2 > 0$	$\lambda_1\lambda_2 < 0$	
node/focus	stable	$Re(\lambda_1) < 0,\ Re(\lambda_2) < 0$	$\lambda_1\lambda_2 > 0$	$\lambda_1 + \lambda_2 < 0$
node/focus	unstable	$Re(\lambda_1) > 0,\ Re(\lambda_2) > 0$	$\lambda_1\lambda_2 > 0$	$\lambda_1 + \lambda_2 > 0$

When the node or focus loses stability, it is possible to construct a bounding surface around the unstable equilibrium. According to the Poincaré-Bendixson theorem [99], a limit cycle must exit in the FHN system when the node or focus is unstable. In other words, the behavior of the FHN system changes qualitatively from a stable equilibrium to a limit cycle. Therefore, in order to identify the ranges of v_{m}^* so that the FHN system has a limit cycle, we need to compute condition 1 and condition 2 in Table A.1 under which the node or focus is unstable, that is,

$$\lambda_1\lambda_2 = f_{1v_{\mathrm{m}}} f_{2w} - f_{1w} f_{2v_{\mathrm{m}}} = -\varepsilon_2\gamma \frac{q(v_{\mathrm{m}}^*, v_1, v_2, v_3, k)}{\varepsilon_1 c_{\mathrm{m}}} + \frac{\varepsilon_2\beta}{\varepsilon_1 c_{\mathrm{m}}} > 0, \tag{A.14}$$

$$\lambda_1 + \lambda_2 = f_{1v_{\mathrm{m}}} + f_{2w} = \frac{q(v_{\mathrm{m}}^*, v_1, v_2, v_3, k)}{\varepsilon_1 c_{\mathrm{m}}} - \varepsilon_2\gamma > 0. \tag{A.15}$$

With the condition (A.8), the discriminant of inequality (A.14) is negative. Therefore, inequality (A.14) is satisfied for all v_{m}^* so that we only need to consider inequality (A.15). If the discriminant of the quadratic polynomial in inequality (A.15) is negative, the inequality is also satisfied for all v_{m}^*. In this work, we are interested in the case when the quadratic polynomial has positive discriminant, i.e.,

$$\Delta_2 > 0, \tag{A.16}$$

where $\Delta_2 = (v_1+v_2+v_3)^2 - 3(v_1v_2+v_1v_3+v_2v_3) - \dfrac{3\varepsilon_1\varepsilon_2 c_{\mathrm{m}}\gamma}{k}$, in which case inequality (A.15) is satisfied if

$$\frac{v_1+v_2+v_3-\sqrt{\Delta_2}}{3} < v_{\mathrm{m}}^* < \frac{v_1+v_2+v_3+\sqrt{\Delta_2}}{3}. \tag{A.17}$$

In a word, the equilibrium is unstable and instead the FHN system has a limit cycle if the equilibrium satisfies inequality (A.17) with the parameters v_1, v_2, v_3, k, β, γ, ε_1, ε_2, c_{m} satisfying inequalities (A.8) and (A.16). Together with Eq. (A.7) and inequality (A.17), we finally obtain the range of the stimulus amplitude ν to produce a limit cycle.

At the transition point (the point at which equilibrium loses stability), the real parts of eigenvalues vanish and the eigenvalues are

$$\lambda_{1,2} = \pm i\sqrt{f_{1v_{\mathrm{m}}}f_{2w} - f_{1w}f_{2v_{\mathrm{m}}}}. \tag{A.18}$$

These eigenvalues correspond to an oscillatory solution, i.e., spike trains, with a frequency given by

$$\omega = \sqrt{f_{1v_{\mathrm{m}}}f_{2w} - f_{1w}f_{2v_{\mathrm{m}}}} = \sqrt{\frac{\varepsilon_2}{\varepsilon_1 c_{\mathrm{m}}}}\sqrt{-\gamma q(v_{\mathrm{m}}^*, v_1, v_2, v_3, k) + \beta}. \tag{A.19}$$

According to Eq. (A.7), v_{m}^* in the above equation is a function of v_1, v_2, v_3, k, β, δ, γ, ν. Hence, the frequency can be represented as

$$\omega = \sqrt{\frac{\varepsilon_2}{\varepsilon_1 c_{\mathrm{m}}}}\, g(v_1, v_2, v_3, k, \beta, \delta, \gamma, \nu), \tag{A.20}$$

where $g(v_1, v_2, v_3, k, \beta, \delta, \gamma, \nu) = \sqrt{-\gamma q(v_{\mathrm{m}}^*, v_1, v_2, v_3, k) + \beta}$, which is a function of v_1, v_2, v_3, k, β, δ, γ, ν.

Vita

Mengxue Zhang

Education

Ph.D., Electrical Engineering, Washington University in St. Louis, Missouri, USA, 2012-2018
Advisor: Prof. Arye Nehorai
Dissertation: Forward Electrophysiological Modeling and Inverse Problem for Uterine Contractions during Pregnancy

M.S., Electrical Engineering, Washington University in St. Louis, Missouri, USA, 2018
Advisor: Prof. Arye Nehorai

B.S., Electrical Engineering, University of Science and Technology of China, China, 2008-2012
Advisor: Prof. Zhongfu Ye

Research Interests

Mathematical modeling of complex systems
Statistical signal processing
Optimization
Machine learning

Research Experience

Research Assistant, 2013-2018
Integrated Signal Processing in Research and Education Lab, Center for Signal and Sensing Information Processing
Department of Electrical and Systems Engineering, Washington University in St. Louis
Advisor: Prof. Arye Nehorai
Topic: forward multiscale modeling and inverse source current estimation for uterine contractions during pregnancy using magnetomyography

Research Assistant, 2011-2012
Institute of Statistical Signal Processing

Department of Electronic Engineering and Information Science, University of Science and Technology of China
Advisor: Prof. Zhongfu Ye
Topic: direction of arrival (DOA) estimation of wideband signals

Publications

Journal Papers:

M. Zhang, P. S. La Rosa, H. Eswaran, and A. Nehorai, "Estimating uterine source current during contractions using magnetomyography measurements," to appear in *PLOS ONE*.

M. Zhang, V. Tidwell, P. S. La Rosa, J. D. Wilson, H. Eswaran, and A. Nehorai, "Modeling magnetomyograms of uterine contractions during pregnancy using a multiscale forward electromagnetic approach," *PLOS ONE* 11(3): e0152421, DOI: 10.1371/journal.pone.0152421, Mar. 2016.

Conference Papers:

D. Escalona-Vargas, **M. Zhang**, A. Nehorai, and H. Eswaran, "Connectivity measures of uterine activity using magnetomyography," to appear in *40th Annual International Conference of the IEEE Engineering in Medicine and Biology Society (EMBC 2018)*, Honolulu, HI, USA, July 17-21, 2018.

X. Xu, **M. Zhang**, and Z. Ye, "Wideband DOA estimation based on sparse signal representation," in *5th International Symposium on Computational Intelligence and Design*, Hangzhou, China, 2012, pp. 10-13. doi: 10.1109/ISCID.2012.154.

Poster Presentation

"Multiscale electromagnetic modeling of contractions in the pregnant uterus," poster presentation at the COMSOL Conference 2014, Boston, MA, USA, Oct. 2014.

Teaching Experience

Instructor, 2013-2016
Study group on Introduction to Mathematical Statistics
Integrated Signal Processing in Research and Education Lab, Center

for Signal and Sensing Information Processing
Department of Electrical and Systems Engineering, Washington University in St. Louis
Responsible for organizing lectures and discussions, teaching, as well as assigning and grading homework

Teaching Assistant, 2016
ESE 517 Partial Differential Equations
Department of Electrical and Systems Engineering, Washington University in St. Louis
Responsible for help sessions and grading homework

Awards

Donald F. Wann Scholarship, 2013
National Scholarship, 2011

August 2018